UNIVERSITY OF CALIFORNIA,
IRVINE

Optical Tweezers Assessment of Cell-Matrix Interactions

DISSERTATION

submitted in partial satisfaction of the requirements
for the degree of

DOCTOR OF PHILOSOPHY

in Biomedical Engineering

by

Alicja Jagiełło

Dissertation Committee:
Professor Elliot Botvinick, Chair
Associate Professor Anna Grosberg
Professor John Lowengrub

2022

DEDICATION

To

My family

Thank you for your love and support.

TABLE OF CONTENTS

LIST OF FIGURES

Page

LIST OF TABLES

Page

ACKNOWLEDGMENTS

First and foremost, I would like to express my deepest gratitude to my advisor and committee chair, Professor Elliot Botvinick, who has continuously supported and motivated me throughout my graduate studies at University of California, Irvine. I feel very fortunate to have had such an excellent mentor.

I would also like to thank my committee members, Professor Anna Grosberg and Professor John Lowengrub, for their encouragement and support of my work. I also want to thank Professor Robert T. Tranquillo and Professor Alex J. Levine for collaborating with me on my projects.

Further, I would like to thank all members of the Botvinick lab, who are too numerous to name, but are all greatly appreciated. To Qingda Hu, thank you for being my friend, for working alongside me and helping me whenever anything broke down. To Dr. Dat Nguyen and Toni Wilkinson, thank you for your friendship. To Dr. Todd Thorson, thank you for proofreading my papers. To Ulysses Castillo, Micah Lim and Dr. Mark Keating, thank you for helping me with my projects. I also thank researchers from other laboratories at University of California, Irvine for sharing their knowledge and advice.

Lastly, I would like to thank my whole family back in Poland as well as Janus Varmarken and Yentl Jagiełło-Varmarken for their continuous love and support.

CURRICULUM VITAE
ALICJA JAGIEŁŁO

EDUCATION

Biomedical Engineering, PhD 2017- 2022
University of California, Irvine GPA 3.96/4.00

Biomedical Engineering, BEng 2013-2017
University of Glasgow Graduated with Honours of the First Class
University of California, Riverside International Exchange Programme. GPA 4.0/4.0 2015-2016

RESEARCH EXPERIENCE

Graduate Researcher – Ph.D. Graduate Student – BEAMS lab
Department of Biomedical Engineering *University of California, Irvine* 2017-2022

- Designed, created and operated opto-mechanical optical tweezers active microrheology system with multi-directional back-focal-plane detection of bead displacement on the sub-micrometer scale.
- Measured stiffness around dermal fibroblasts and cancerous human cells cultured in 3D hydrogels with different mechanical and biochemical properties.
- Correlated peri-cellular stiffness with cellular processes and hydrogel properties using physiological modelling and non-parametric statistical analysis in MATLAB.
- Mentored three undergraduate students.

Undergraduate Researcher – Prof. Nikolaj Gadegaard's Laboratory
Department of Biomedical Engineering *University of Glasgow* 2016-2017

- Quantified cell morphology, migration, proliferation and cell traction forces exerted by pancreatic cancer cells for a project funded by Cancer Research UK
- Performed soft lithographic molding to create PDMS micropillar arrays for quantification of cell traction forces

Undergraduate Researcher – Biomaterials & Nanomedicine Lab
Department of Biomedical Engineering *University of California, Riverside* 2015-2016

- Prepared safe and biodegradable neural electrodes and analyzed their mechanical and biochemical properties before and after surface modification using conducting polymers.
- Conducted Tafel and cyclic voltammetry measurements on a daily basis.

TEACHING EXPERIENCE

Teaching Assistant – Engineering Analysis and Design: Data Acquisition
BME60A Department of Biomedical Engineering University of California, Irvine Fall 2020
BME60A Department of Biomedical Engineering University of California, Irvine Fall 2019

Teaching Assistant – Photomedicine
BME135 Department of Biomedical Engineering University of California, Irvine Fall 2018

PUBLICATIONS

Jagiełło, A., Castillo, U., Botvinick, E., "Stiffness-matched extracellular matrices comprising collagen or fibrin differentially affect cell-mediated remodeling and peri-cellular stiffness". *Sci. Rep.* (2022), Submitted.

Jagiełło, A., Hu, Q., Castillo, U., Botvinick, E., "Patterned photocrosslinking to establish stiffness anisotropies in fibrous 3D hydrogels". *Acta Biomater* (2021), S1742-7061(21)00842-4.

Thrivikraman, G., **Jagiełło, A.**, Lai, V. K., Johnson, S. L., Keating, M., Nelson, A., Schultz, B., Wang, C. M. Levine, A. J., Botvinick, E. L., Tranquillo, R. T., "Cell contact guidance via sensing anisotropy of network mechanical resistance". *PNAS* (2021), 118 (29):e2024942118.

Jagiełło A., Lim M., Botvinick E., "Dermal fibroblasts and triple-negative mammary epithelial cancer cells differentially stiffen their local matrix". *APL Bioeng* (2020), 4(4):046105.

Rath, N., Munro, J., Cutiongco, M. F., **Jagiełło, A.**, Gadegaard, N., McGarry, L., Unbekandt, M., Michalopoulou, E., Kamphorst, J.J., Sumpton, D., Mackay, G., Vennin, C., Pajic, M., Timpson, P., Olson, M. F., "Rho Kinase Inhibition by AT13148 Blocks Pancreatic Ductal Adenocarinoma Invasion and Tumor Growth". *Cancer Res.* (2018), 78(12):3321-3336.

ORAL PRESENTATIONS

Jagiełło, A., Hu, Q., Castillo, U., Botvinick, E., *Using light to establish and measure stiffness gradients in three-dimensional engineered tissues*, International Society of Optics Photonics: Nanoscience + Engineering. San Diego, CA. August 2021.

Jagiełło, A., Lim, M., Botvinick, E., *Dermal fibroblasts and human breast cancer cells differentially stiffen their local matrix*, 13th European Biophysics Conference, Vienna, Austria, July 2021.

Jagiełło, A., Lim, M., Botvinick, E., *Cells Establish Spatially Heterogeneous And Anisotropic Stiffness Landscapes – Direct Measurements*, SB3C2020 Summer Biomechanics, Bioengineering and Biotransport Conference (Virtual), June 2020.

Jagiełło, A., Ramirez-Guerrero, D., McEvoy, E., Shenoy, V., Botvinick, E., Lowengrub, J., *Unraveling how interactions of chemical signaling and mechanical forces influence cell fate decisions and behaviors of growing tissues,* 2nd Annual Symposium on Multiscale Cell Fate, NSF-Simons Center for Multiscale Cell Fate Research, UC Irvine, October 2019.

Jagiełło, A., Ramirez-Guerrero, D., McEvoy, E., Shenoy, V., Botvinick, E., Lowengrub, J., *Unraveling how interactions of chemical signaling and mechanical forces influence cell fate decisions and behaviors of growing tissues*, Early-Career Researcher Symposium 2019, NSF-Simons Center for Multiscale Cell Fate Research, UC Irvine, March 2019.

POSTER PRESENTATIONS

Jagiełło, A., Hu, Q., Castillo, U., Botvinick, E., *Patterned photocrosslinking to create stiffness gradients and local anisotropies in 3D hydrogels*, 2021 Biomedical Engineering Society Annual Meeting, Orlando, FL, October 2021.

Jagiełło, A., Lim, M., Botvinick, E., *Dermal fibroblasts and breast cancer cells differentially alter their local stiffness landscape,* American Physical Society March Meeting 2021 (Virtual), March 2021.

Jagiełło, A., Lim, M., Botvinick, E., *Cells differentially alter their local stiffness landscape as assessed,* 65th Virtual Annual Meeting of the Biophysical Society, February 2021.

Jagiełło, A., Ramirez-Guerrero, D., McEvoy, E., Shenoy, V., Botvinick, E., Lowengrub, J., *Unraveling how interactions of chemical signaling and mechanical forces influence cell fate decisions and behaviors of growing tissues,* NSF-Simons visit to Center for Multiscale Cell Fate Research at UCI, Irvine, CA, USA, October 2019.

ABSTRACT OF THE DISSERTATION

Optical Tweezers Assessment of Cell-Matrix Interactions

by

Alicja Jagiełło

Doctor of Philosophy in Biomedical Engineering

University of California, Irvine, 2022

Professor Elliot Botvinick, Chair

Understanding complex interactions between a cell and its extracellular matrix (ECM) lies at the core of mechanobiology. For instance, stiffness of the ECM was previously shown to be highly heterogenous and deregulated in wound healing or during cancer progression. However, tools available for measuring and dynamically altering peri-cellular stiffness have been lacking and bulk measurements do not probe stiffness sensed by the cells. Thus, we have developed an optical tweezers active microrheology (AMR) system capable of multi-axes stiffness measurements in the peri-cellular region.

In this thesis, multi-axes AMR system was used to investigate highly heterogenous and anisotropic stiffness landscapes established by dermal fibroblasts, human breast cancer and fibrosarcoma cells. Peri-cellular stiffness and anisotropy are shown to vary between the tested cell lines and with different treatments modifying cell behavior. Further, stiffness landscape and cell response to ECM vary with hydrogel source, concentration and fiber architecture of the local ECM. These studies underscore the need for peri-cellular and not bulk stiffness measurements in studies on cellular mechanotransduction.

Additionally, the method of patterned crosslinking is used to alter ECM topography by inducing fiber alignment and peri-cellular stiffness landscape. Following localized crosslinking, human breast cancer cells undergo contact guidance and durotaxis, as indicated by cell migration in a direction of fiber alignment and along an off-axis stiffness gradient, respectively. While these phenomena are widely known and studied on 2D substrates or in 3D synthetic hydrogels, patterned crosslinking allows for better understanding of processes governing directed migration of individual cells embedded inside naturally-derived fibrous hydrogels.

Collectively, this thesis work investigates how cells respond to and regulate their local ECM stiffness based on a variety of different factors. Local ECM stiffness landscape established by the cells and probed using multi-axes AMR differs with the addition of different treatments regulating cell behavior and it is also strongly dependent on biochemical, mechanical and topographical properties of the ECM.

Chapter 1: Introduction and Background

1.1. Extracellular matrix

Extracellular matrix (ECM) is an assembly of cell-secreted proteins which provides physical and biochemical support to the cells and controls homeostasis, function and development of majority of eukaryotic cells in the human body [1–5]. Changes in biochemical, structural or mechanical properties of the ECM can alter cell development and behavior. In a reciprocal way, composition, structure and function of the ECM are also constantly modified by cells [1–5]. Nonetheless, more comprehensive understanding of bi-directional relationship between cell and surrounding ECM in healthy and diseased tissues is still required. Our interpretation of dynamic cell-ECM interactions is constantly evolving and remains at the core of the field of mechanobiology.

1.1.1. Cell-ECM interactions

Mechanobiology is commonly defined as a study of the role of physical properties of the ECM on cellular behavior and function [6]. While most cells are mechanosensitive and possess the ability to respond to and remodel their surrounding ECM [6], fibroblasts are predominantly associated with regulating and maintaining the properties of the ECM in connective tissue [1]. Fibroblasts can synthesize new ECM by secreting many of the ECM components, including collagen and glycoproteins [1,4]. At the same time, cells can degrade their local matrix by the deposition of different matrix metalloproteinases (MMPs) [1,4]. In healthy tissues, ECM synthesis and degradation are constantly carried out by cells to support cellular and functions and maintain tissue homeostasis, while in diseased tissues, cell-ECM dynamics are disrupted and protease activity is often deregulated [1,5]. The extent of cell-

mediated ECM remodeling is dependent on mechanosensing mechanisms controlled in part by integrins binding the ECM to proteins, Rho-associated protein kinase (ROCK) activity driving acto-myosin contractility and integrin-rich focal adhesions providing physical linkage between the cells and the ECM [6–8].

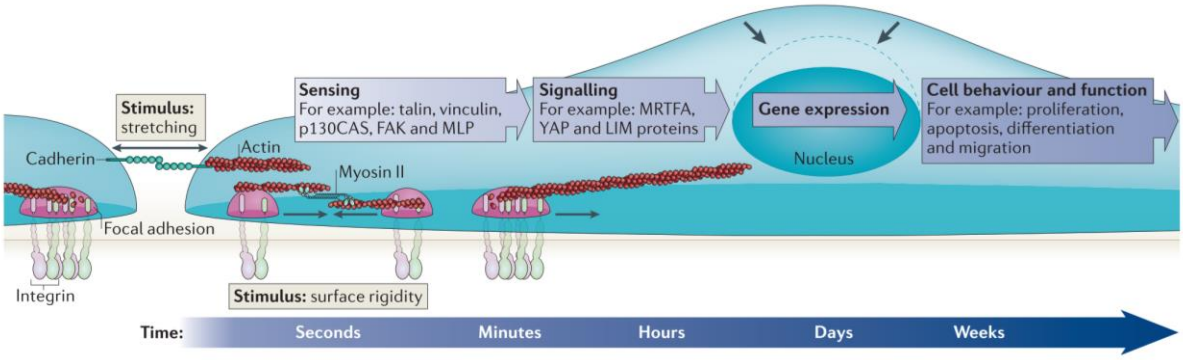

Figure 1.1. Mechanotransduction describes cell response to external mechanical stimuli [7].

Cellular behaviors are also regulated by the ECM properties. In a process known as mechanotransduction, cells respond to their local environment by converting mechanical stimuli into chemical response resulting in change in gene expression and cellular behavior and function (**Figure 1.1.**) [6,7] . For instance, stiffness of the ECM was found to play a crucial role in regulating cell morphology, rate of migration, cell cycle progression and apoptosis [1,5]. Increase in bulk ECM stiffness has also been correlated with cancer invasiveness and ECM stiffness was shown to direct lineage adopted by the stem cells [9]. Nonetheless, the effect of bulk ECM stiffness on cells was reported to vary between different cell lines [1]. Important to my thesis, our group has previously shown that bulk measurements of ECM stiffness do not accurately represent stiffnesses that cells are actually sensing [10]. As shown in **Figure 1.2**, stiffness around individual cells can not only span a few orders of magnitude, but also exceed the range of bulk stiffness of hydrogels reported in literature.

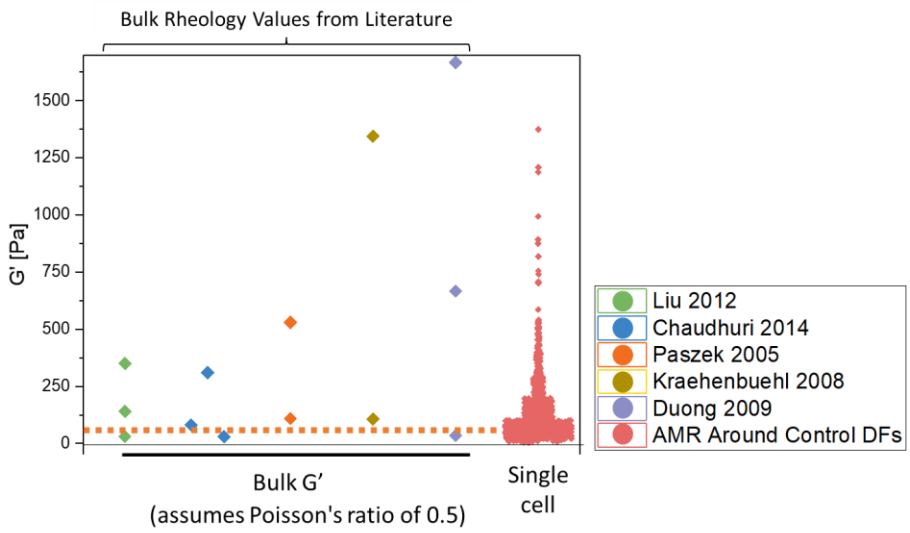

Figure 1.2. Comparison of stiffness values measured in hydrogels with cells using bulk rheology and AMR around single dermal fibroblasts (courtesy of Dr. Mark Keating).

1.1.2. ECM composition

Composition of the ECM was also previously shown to regulate cell properties. The composition of the ECM is highly specialized for individual tissues in the human body, but it is primarily composed of water, structural fibrous proteins (including collagens, laminin, elastin and fibronectins), proteoglycans as well as growth factors and glycoproteins [2–4,11]. Composition of the ECM undergoes dynamic remodeling in response to a variety of stimuli including aging, wound healing processes or cancerous changes, as indicated in **Figure 1.3** [4]. Collagen is typical to many of these tissues and is under investigation in my thesis work.

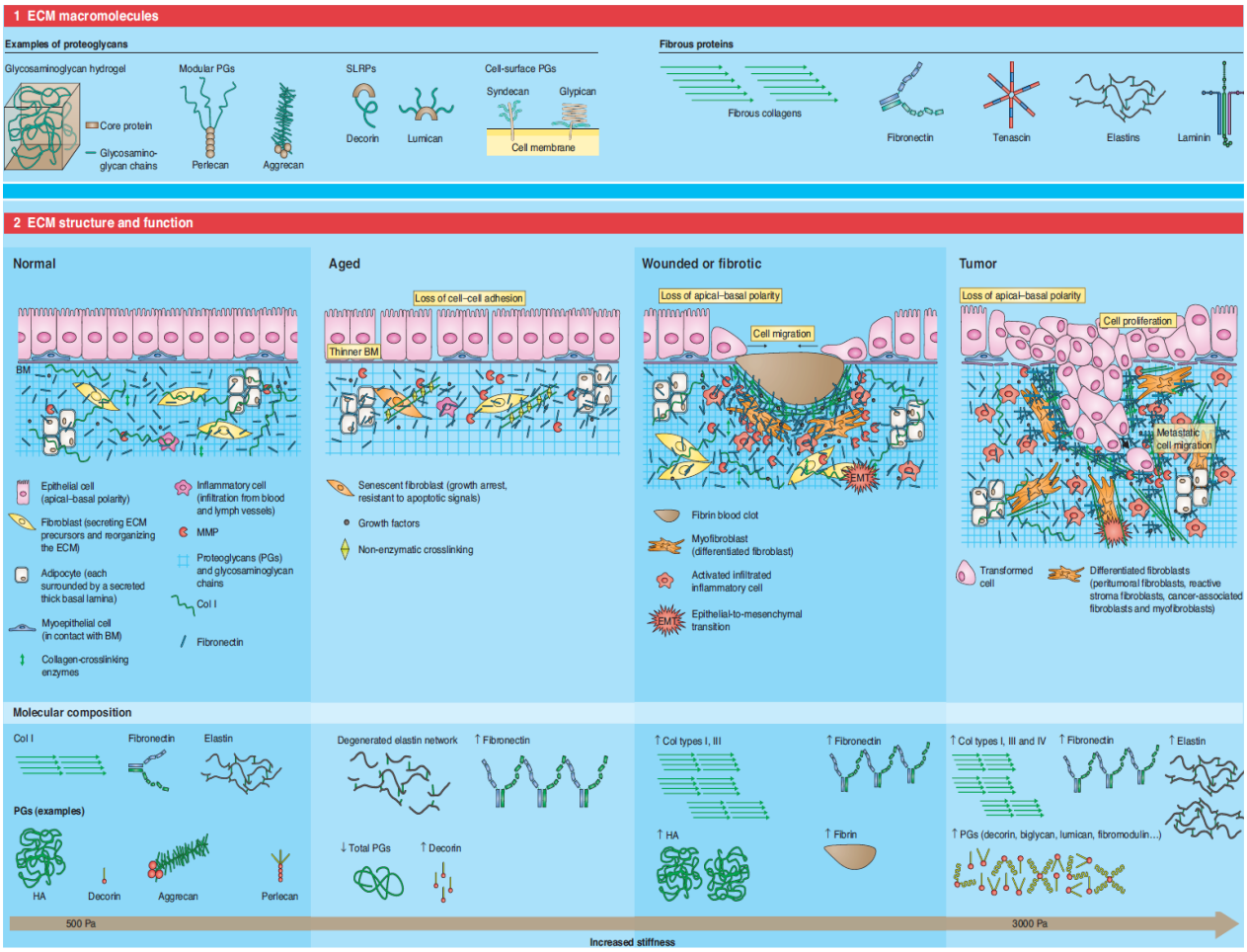

Figure 1.3. Changes in structure and composition of the ECM in response to aging, injury or cancer (adapted from [4]).

1.1.3. Collagen

Collagen is the most dominant component of the natural ECM and it provides most of the structural support for cells in connective tissues [4]. There are at least 28 different types of collagen in the human body, but type 1 collagen (T1C) is the most abundant component of the natural ECM [1]. T1C regulates many cellular processes and behaviours including tissue development, cell migration and chemotaxis [2,4,5]. On a structural level, T1C exhibits organization similar to other fibrillar collagens and T1C is formed by a self-assembly of 3 α chains into right-hand triple helix with repeating motifs of amino acids, as shown in **Figure 1.4A** [3,12]. Collagen molecules form cross-striated microfibrils which then form individual

collagen fibrils and then fibers with a diameter of 0.5-20 μm [1,13,14]. In the cell-free T1C hydrogels, collagen fibers form complex networks with random distributions of fiber alignments. Consequently, isotropy in stiffness of T1C hydrogels is commonly associated with heterogenous alignment of nonlinearly elastic ECM fibers [12,15–17]. Nonetheless, cells can promote more anisotropic fiber distribution [18,19]. Cells can significantly alter fiber architecture and align the ECM fibers in the direction of cell migration [18] or in order to enhance long range stress signaling between neighboring cells [20].

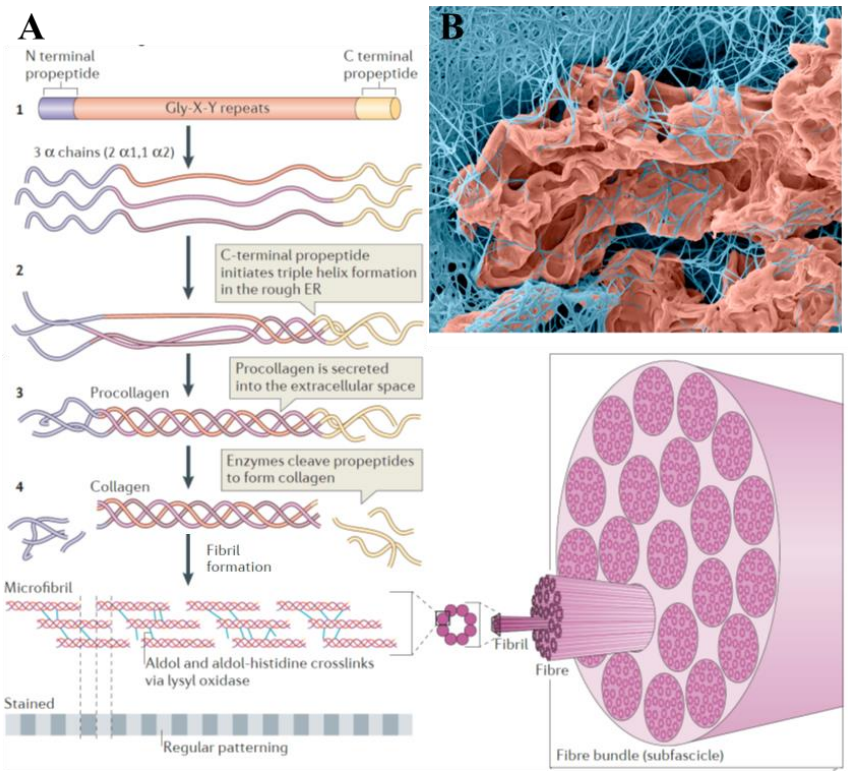

Figure 1.4. (A) Structure of T1C [3]. (B) Psuedocolored SEM image of HT-1080 cell in T1C network [21].

Due to abundance of T1C in natural ECM, T1C provides a more physiologically relevant environment than synthetic ECM [22,23]. Moreover, culturing cells in 3D collagen hydrogels as opposed to on 2D substrates preserves cell polarity and cell anchorage as well as maintains the activity of intracellular signalling pathways [2,12,24–26]. 3D culture also promotes higher rate of cell renewal and growth in stem cell research and was also reported

to improve clinical outcomes of the MSCs due to mimicking their natural *in vivo* interactions with ECM [12,27,28].

Properties of collagen hydrogels, including their bulk stiffness, are affected by T1C concentration, stock, temperature of polymerization, pH, as well as by the source of collagen and method of extraction [29,30]. Extraction method alters molecular structure of collagen and pepsin digested collagen has much lower density of crosslinks and slower rate of polymerization than acid extracted collagens. In my thesis work, I used T1C collagen extracted using acid solubilization, obtained either from rat tail or bovine skin. Even though structure of bovine skin T1C differs from rat tail T1C and *in vivo* collagen, bovine skin T1C is more commonly used in therapeutic applications, due to its minimal antigenicity [29,31–33].

1.1.4. Fibrin

In my work, cells will also be embedded inside fibrin hydrogels. Fibrin is often used as a substitute of natural ECM in the *in vitro* studies and it can be remodeled and degraded by the cells. Nonetheless, properties of fibrin differ significantly from T1C. Fibrin is formed during thrombin-catalyzed extraction of fibrinopeptides from fibrinogen and mechanical properties of fibrin are suited for its role in blood clot formation [13]. Consequently, fibrin does not have the durability of the natural ECM or collagen hydrogels [4]. Elastic (G') and viscous (G'') modulus were previously shown to be significantly higher in fibrin hydrogels than in collagen hydrogels, but collagen fibers exhibit more bundling than single fibrin fibers [13,34,35]. Nonetheless, properties of fibrin and collagen have not been compared at matched bulk stiffness levels.

1.2. Matrix stiffness and cell behavior

1.2.1. ECM stiffness during wound healing

ECM fiber network is significantly altered due to injury and changes in mechanical and chemical properties of the ECM initiate wound healing processes [36]. In skin wound healing, rebuilding of the damaged epidermal barrier starts with hemostasis that results in the formation of the stiff fibrin clot that prevents bleeding from the wound. Subsequent release of cytokines and growth factors promotes recruitment of neutrophils and macrophages during the inflammatory phase. Afterwards, fibroblasts are recruited by inflammatory cells to the site of the injury. Fibroblasts produce high levels of MMPs and deposit collagen and ECM components, forming granulation tissue that replaces the fibrin scab [36–39]. Dermal fibroblasts are also proliferating very fast during wound healing, which additionally elevates mechanical stresses and local ECM stiffness [4,36]. Furthermore, fibroblasts in the presence of TGF-β differentiate into highly contractile myofibroblasts which promote ECM crosslinking and tissue remodeling. Myofibroblasts possess even more prominent capability to secrete ECM components than fibroblasts [4,39]. Due to action of fibroblasts and myofibroblasts, tension of the tissue is much higher than in the intact tissue. Higher tension promotes elevated expression and translocation of Yes-associated protein (YAP) and transcriptional coactivator with PDZ-binding motif (TAZ) to the nucleus of keratinocytes, which drives their proliferation, prevents apoptosis and stimulates wound closure and rebuild of the epidermal layer of skin [36–39]. During the wound healing process, multiple chemical signaling pathways coordinate individual wound healing stages and control behaviors of distinct cell types [38]. Furthermore, elevated levels of fibroblast,

keratinocytes and epidermal growth factors bound to ECM promote chemotaxis of cells towards the wound bed and hence ensure fast wound closure and tissue re-growth [37,40].

Following the reepithelialization of the skin layer, removal of the fibrin clot and completion of the wound healing process, healthy tissue initiates resolution of fibrosis and reinstatement of tissue homeostasis. These processes promote reduction in tissue stiffness [4]. Nonetheless, deeper wounds will result in scar formation. Scar tissue not only lacks hair follicles and sweat glands, but it can also be characterized by longitudinal alignment of thinner and stiffer ECM fibers which results in anisotropic mechanical properties of the tissue [37,38]. Due to functional and esthetic ramifications of scar formation and ineffectiveness of current therapies, mechanomodulatory therapies have been recently suggested as potential alternative [36,40–42]. Alteration of mechanical signaling including hindering of the Rho-Rock pathway and reduction of ECM stiffness at later stages of wound healing process is suggested to potentially reduce the extent of scar formation and improve mechanical properties of the tissue [36,40].

Wound healing is a complex and multi-step process during which local stiffness is significantly altered. Nonetheless, in my thesis, I predominantly focus on how the initial bulk ECM stiffness as well as cell remodeling abilities regulate peri-cellular stiffness. Given that dermal fibroblasts are one of the most important players in wound healing and largely control ECM stiffness, **Chapter 2** and **Chapter 3** seek to better understand interactions of dermal fibroblasts with ECM to elucidate how peri-cellular stiffness is affected by changes in mechanical and biochemical properties of the cell environment.

1.2.2. ECM stiffness in cancer

In a healthy tissue, relaxed networks of fibers surround cells and ensure that tissue can withstand a range of tensile and compressive stresses [4]. On the other hand, aged tissues are mechanically weaker, yet are characterized by higher rigidity and stiffness due to non-enzymatic crosslinking [4]. These changes affect organization of the ECM fibers and promote cancer and age-related diseases. Cancer cells were reported to possess higher contractile properties than healthy cells [43], and consequently exhibit elevated cell traction forces and promote stiffening of the local ECM [44]. Cell response to physical cues from the local ECM results in higher YAP translocation into the nucleus and alters cancer cell morphology. Furthermore, ECM remodeling enzymes, including MMPs, exhibit higher expression levels than in healthy tissue and upregulated oncogenic signaling pathways including Akt, Wnt, p53, TGF-β and Notch pathways further facilitate cancer progression [5,43,45,46].

Furthermore, cancerous tissues exhibit aberrant organization of the ECM, abnormal cell behaviors and chronic inflammation, which result in fibroblasts activation. Cancer-associated fibroblasts promote ECM deposition resulting in even higher stiffness of tumors than in surrounding healthy tissue and myofibroblasts further crosslink ECM and deposit MMPs [5,44,45]. Consequently, many types of tumors, including breast cancer, are characterized and diagnosed by elevated tissue density and upregulated levels of collagen and proteoglycans [5,43–45]. In the human body, ECM also affects other cells near the cancerous tissues and regulates the activity of immune and endothelial cells, resulting in higher rates of angiogenesis, hypoxia and chronic inflammation, processes which further drive cancer progression and promote metastasis [5,44].

Metastasis reduces the effectiveness of the available clinical treatments and approximately 90% of cancer related deaths result from the metastatic changes [47,48]. The first step in the metastasis process is TGF-β-induced epithelial-mesenchymal transition (EMT) which can be observed by higher expression of mesenchymal markers and loss of epithelial markers [43,46]. EMT occurs due to changes in gene expression, cell adhesion and cytoskeletal organization and promotes ECM stiffening by fibroblast-controlled collagen deposition. EMT further stimulates more invasive phenotype of cancer cells and spreading to distant sides [46,49].

Interestingly, while the cancer cell environment undergoes significant stiffening, plasticity of cancer cells was shown to increase with cancer invasiveness [48,50–52]. Increased plasticity of cancer cells also enables higher rates of cell migration and invasion during metastasis as cells can move through stiff ECM and small capillaries [51,53,54]. Cancer cells migrate along the collagen fibers with increased rates of cell migration corresponding to elevated ECM stiffness levels, yet adopt multiple modes of migration during cancer metastasis [55–57].

Tumor formation and cancer progression are regulated by co-operation of a variety of biochemical and mechanical factors altering cancer cell properties and disrupting cell-ECM dynamics. In my thesis, I focus only on the local stiffness around single breast cancer (**Chapter 2**) and fibrosarcoma (**Chapter 3**) cells and establish how peri-cellular stiffness landscapes are affected by changes in mechanical properties of ECM or by altering biochemical properties of cells and promoting more or less invasive cancer cell phenotypes.

1.2.3. Durotaxis and contact guidance

Numerous mechanical and biochemical properties of the environment sensed by the cells were previously shown to regulate the direction of cell migration. Directed cell migration can be divided based on the stimuli sensed by the cells. For instance, cells were previously described to move along chemical gradients (chemotaxis) [58] or along the oxygen gradient (aerotaxis) [59]. Specific to my thesis work, cells can also migrate along the stiffness gradient in a phenomena known as durotaxis [60–62], or exhibit contact guidance and align themselves and migrate along the topographical features of the local environment [63,64].

Durotaxis is exhibited by numerous cell lines including fibroblasts [58], mesenchymal stem cells [65], smooth muscle cells [66] and many cancer cells lines [61,67]. In most cases, cells are shown to migrate towards regions of the higher stiffness, but negative durotaxis towards softer regions has also been reported [68]. Past research on collective and single-cell durotaxis found that durotactic migration can alter cell phenotype, shape and promote tissue fibrosis [69,70]. Deep understanding of processes governing durotaxis is still lacking, but migration towards stiffer ECM is suggested to be regulated by focal adhesion mechanosensing and signaling [61,62,71,72]. Stiffer substates promote faster development of cell protrusions and maturation of focal adhesions than softer materials, facilitating migration towards stiffer regions [62,70,73]. Nonetheless, durotaxis was also shown to depend on the composition of the ECM, range of ECM stiffness or strength of the stiffness gradient [65–67].

Durotaxis has been predominantly studied on 2D substrates with distinct stiffness gradients controlled by varying concentration of the crosslinker, duration of crosslinking or thickness of the substrate [71]. Methods developed for 3D cultures include the use of synthetic hydrogels or colloidal crystals with tunable stiffnesses [67,71,72,74]. Creation of 3D hydrogels

with reproducible stiffness gradients remains a challenge in naturally-derived fibrous hydrogels. Nonetheless, stiffness gradients in fibrous hydrogels can be created by casting hydrogels on wedged molds [75] or by inducing strain gradients, as previously described by our group [76].

Contact guidance of cells has also been shown to regulate numerous physiological processes, including morphogenesis, wound healing and cancer metastasis [77–80]. Past research indicated that cells display contact guidance by sensing local topography via focal adhesions and filopodia [78]. While ROCK-mediated acto-myosin contractility was described to play a crucial role in contact guidance [78,81], the phenomenon was also shown to persist following inhibition of myosin II, which is responsible for regulating cell polarity [82]. Recent studies by our group have also found that cells exhibit contact guidance by sensing and responding to anisotropies in mechanical properties of aligned fibrous hydrogels [83].

Contact guidance is commonly studied by culturing cells on 2D substrates micropatterned with distinct topographical features (grooves, ridges, pillars) [78] or fibronectin lines [80]. Studies on 3D hydrogels are most frequently conducted by aligning hydrogel fibers by magnetic alignment of fibers [81,83] or mechanical hydrogel stretching [77,84] or cellular compaction [85]. The spatial organization of cells on micropatterned substrates or in aligned hydrogels can be modified by altering geometry of topographical features [78,80].

While most studies on durotaxis and contact guidance have been conducted either on 2D substrates or by altering properties of whole 3D hydrogels, method of patterned crosslinking described in **Chapter 4** aims to alter only local ECM properties of naturally-derived fibrous hydrogels and potentially facilitate future studies on processes governing directed cell migration on a single cell level.

1.3. Active microrheology

In my thesis work, I measure stiffness around individual cells using multi-axes optical tweezers active microrheology system. Contrary to bulk rheology, microrheology allows accurate spatial and temporal measurements of material properties on a much smaller scale and hence can detect local heterogeneities obscured by measurements with parallel plate rheometer [86]. Using microrheology techniques, mechanical properties of complex fluids, including local stiffness levels can be obtained by quantifying the displacement of beads embedded in hydrogels [86,87]. While passive microrheology determines the bead displacement due to thermal fluctuations, in active microrheology bead displacement is imposed by external optical, magnetic or micromechanical forces [86,88,89]. In our laboratory, we use AMR incorporating optical tweezers. During AMR measurements, optically trapped bead embedded in 3D hydrogels is oscillated by the sinusoidal displacement of the trapping laser beam. Change in bead position is then detected using laser detection system.

1.3.1. Optical tweezers system

The AMR system used for my experiments is presented in **Figure 1.5**. It incorporates a continuous-wave fiber laser with an emission at 1064 nm (IPG Photonics), that produces the trapping beam with the power of approximately 240 mW. The trapping beam is oscillated by the movement of a pair of galvanometer mirrors (ThorLabs), that are placed conjugate to the back focal plane of the microscope objective lens. The trapping beam is then split by the beam splitter (ThorLabs), which allows beam position to be recorded by a quadrant photo diode (trapQPD, Newport). Detection beam is generated by a single mode fiber-pigtailed laser (ThorLabs) with emission at 785 nm and power of 22 mW. Both beams are coaligned and enter into the white light path of an IX81 inverted microscope (Olympus). As described

in [10], microscope in our laboratory is equipped with the Zero Drift Compensation package (Olympus) with a filter cube below the microscope objective lens and external laser/detector unit replaced by the stock dichroic beam splitting mirror with a short pass dichroic beam splitting mirror (Chroma Technologies). While it passes visible light for confocal and brightfield microscopy, it allows focusing of the light from both beams into the sample by a high numerical aperture microscope objective lens (60x-oil PlanApo TIRFM 1.45 NA, Olympus). Focus height for both beams was adjusted to be approximately the same. Light from the sample is then back reflected and goes through 1064 nm pass dichroic beam splitting mirror (Chroma Technologies) that reflects the light towards the detection beam quadrant photo diode (detQPD, Newport). During the sinusoidal oscillations of the trapping beam, position of the bead is recorded by the detQPD, as the analog signal proportional to the position of the bead.

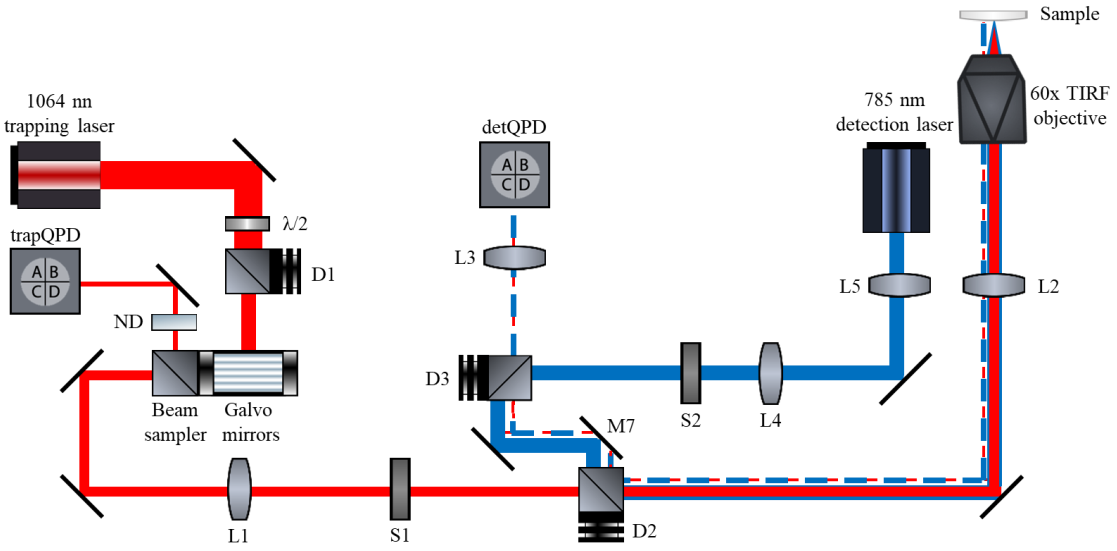

Figure 1.5. Schematics of the AMR system; Optical components: λ/2 – half-wave plate (WPH10M-1064, ThorLabs), ND – neutral density filter (NENIR20A-C, ThorLabs), D1 – polarizing beamsplitter with beam dump (CM1-PBS253, ThorLabs), D2 – dichroic beamsplitter with beam dump (FF875-Di01, Semrock), D3 – pellicle beamsplitter with beam dump (CM1-BP145B2, ThorLabs), D4 - short pass dichroic beam splitting mirror (ET750SP-2P8, Chroma Technologies), L1-L5 – lenses, S1-S2 – shutters (SHB05T, ThorLabs).

AMR system incorporates a robotic system controlled by custom software developed in our laboratory and described in [10]. It allows for stage movement between beads and accurate positioning of the optical trap in the center of each bead. Following the bead centering, optical trap is oscillated sinusoidally at a given frequency and amplitude for 5 s along each specified axis. Using signals recorded by detQPD and trapQPD during bead and trap oscillations, peri-cellular stiffness κ (nN/μm) is calculated as described in [76,88,90] and summarized in **Figure 1.6**. κ corresponds to a real component of κ^*, calculated using **Equation (1)**:

$$\kappa^*(\omega) = \frac{1 - k_t A^*(\omega)}{A^*(\omega)} \qquad (1)$$

where $A^*(\omega)$ is a frequency-dependent complex response function and k_t is a sum of trapping beam and detection beam stiffnesses calculated during calibration in water.

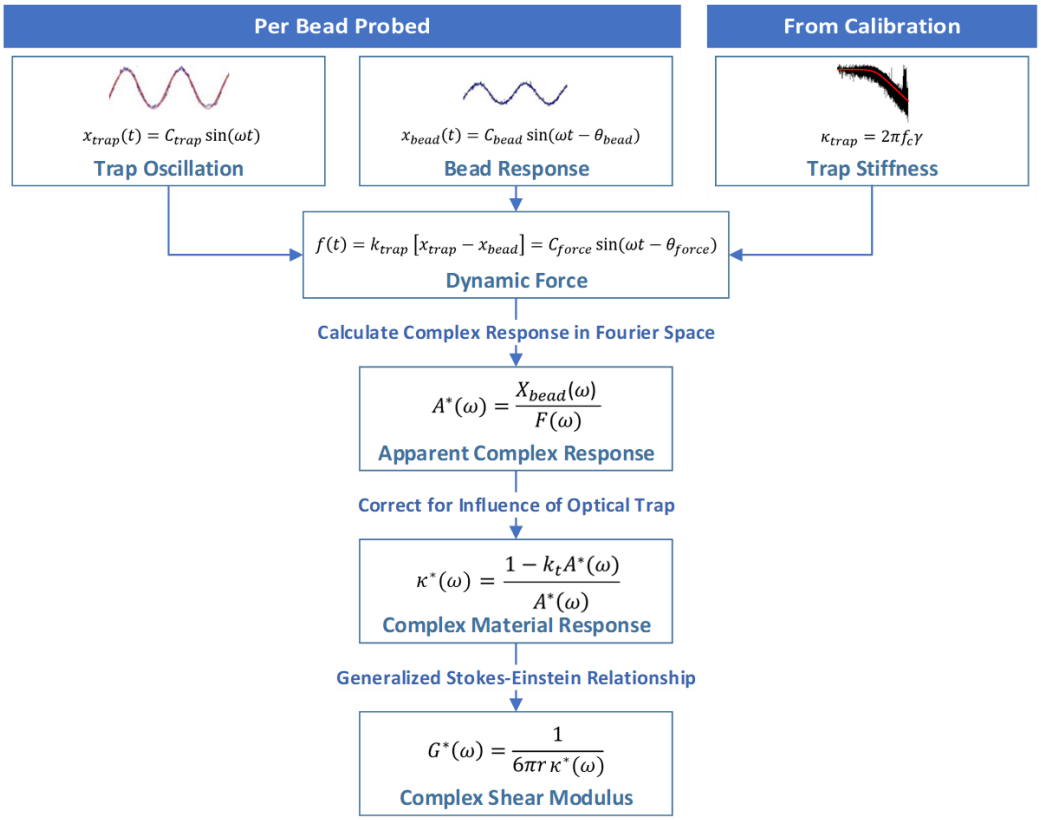

Figure 1.6. Calculations of κ (courtesy of Dr. Mark Keating).

1.3.2. System alignment and calibration

Prior to measurements of stiffness in hydrogels, AMR system is calibrated in a water sample with diluted number of 2 μm microbeads. A single bead is trapped by both lasers and brought to a chosen height from the glass. Lasers beams are then co-aligned and centered on the bead and on detQPD and trapQPD. Afterwards, three calibration factors are calculated for each desired angle of bead oscillation. Trap stiffness k_t is obtained using the power spectrum method [88,91,92]. Briefly, power spectrum of the Brownian motion of the bead collected for 30 s is fit with a Lorenzian equation. Corner frequency (f_c) in the Lorenzian equation is proportional to the trap stiffness and obtained with **Equation (2)**:

$$k_t = 2\pi f_c \gamma \qquad (2)$$

where γ is a viscous drag coefficient, calculated based on the value of water viscosity η and bead radius r [91,93] using **Equation (3)**:

$$\gamma = 6\pi\eta r \qquad (3)$$

Position sweep of the bead is implemented to obtain the voltage-to-bead displacement factors β for detQPD and trapQPD. Trapping beam centered on the bead is subjected to a triangular wave displacement with a frequency of 0.1 Hz and an amplitude of 0.4 μm. β values are calculated based on the signals recorded by detQPD and trapQPD during the bead displacement .

Calibration factors are found for at least 3 beads and average k_t and β values specific for each axis of oscillation are used for AMR measurements. Prior to experiments in hydrogels, system calibration is validated by comparing viscosity calculated during AMR measurements in water with theoretical water viscosity.

1.4. References

1. Humphrey, J. D., Dufresne, E. R. & Schwartz, M. A. Mechanotransduction and extracellular matrix homeostasis. *Nat. Publ. Gr.* **15**, 802-812 (2014).

2. Daley, W. P., Peters, S. B. & Larsen, M. Extracellular matrix dynamics in development and regenerative medicine. *J. Cell Sci.* **121**, 255–264 (2008).

3. Mouw, J. K., Ou, G. & Weaver, V. M. Extracellular matrix assembly : a multiscale deconstruction. *Nat. Rev. Mol. Cell Biol.* **15**, 771–85 (2014).

4. Frantz, C. *et al.* The extracellular matrix at a glance. *J. Cell Sci.* **123**, 4195–4200 (2010).

5. Lu, P., Takai, K., Weaver, V. M. & Werb, Z. Extracellular Matrix Degradation and Remodeling in Development and Disease. *Cold Spring Harb Perspect Biol* **3**, 1–24 (2011).

6. Eyckmans, J., Boudou, T., Yu, X. & Chen, C. S. A Hitchhiker's Guide to Mechanobiology. *Dev. Cell* **21**, 35–47 (2011).

7. Iskratsch, T., Wolfenson, H. & Sheetz, M. P. Appreciating force and shape — the rise of mechanotransduction in cell biology. *Nat. Rev. Mol. Cell Biol.* **15**, 825–833 (2014).

8. Doyle, A. D. & Yamada, K. M. Mechanosensing via cell-matrix adhesions in 3D microenvironments. *Exp. Cell Res.* **343**, 1–7 (2015).

9. Engler, A. J., Sen, S., Sweeney, H. L. & Discher, D. E. Matrix Elasticity Directs Stem Cell Lineage Specification. *Cell* **126**, 677–689 (2006).

10. Keating, M., Kurup, A., Alvarez-Elizondo, M., Levine, A. J. & Botvinick, E. Spatial distributions of pericellular stiffness in natural extracellular matrices are dependent on cell-mediated proteolysis and contractility. *Acta Biomater.* **57**, 304–312 (2017).

11. Halper, J. & Kjaer, M. Basic Components of Connective Tissues and Extracellular Matrix : *Adv Exp Med Biol.* **802**, 31–47 (2014).

12. Nassif, N. & Fernandes, F. M. Collagen-based Materials for Tissue Repair, from Bio-inspired to Biomimetic. in *Material Design Inspired by Nature: Function Through Inner Architecture* 107–126 (2013).

13. Moreno-Arotzena, O., Meier, J., del Amo, C. & García-Aznar, J. Characterization of Fibrin and Collagen Gels for Engineering Wound Healing Models. *Materials (Basel).* **8**, 1636–1651 (2015).

14. Kadler, K. E., Holmes, D. F., Trotter, J. A. & Chapman, J. A. Collagen fibril formation. *Biochem. J.* **316**, 1–11 (1996).

15. Nam, S., Hu, K. H., Butte, M. J. & Chaudhuri, O. Strain-enhanced stress relaxation impacts nonlinear elasticity in collagen gels. **113**, 1–6 (2016).

16. Licup, J. A. *et al.* Stress controls the mechanics of collagen networks. *PNAS* **112**, 9573–9578 (2015).

17. Thomopoulos, S., Fomovsky, G. M., Chandran, P. L. & Holmes, J. W. Anisotropy in Fibroblast Populated Collagen Gels. **129**, 642-650 (2007).

18. Velegol, D. & Lanni, F. Cell Traction Forces on Soft Biomaterials. I. Microrheology of Type I Collagen Gels. *Biophys. J.* **81**, 1786–1792 (2001).

19. Thomopoulos, S., Costa, K. D. & Holmes, J. W. The Development of Structural and Mechanical Anisotropy in Fibroblast Populated Collagen Gels. *J Biomech Eng* **127**, 742–750 (2005).

20. Ma, X. *et al.* Fibers in the extracellular matrix enable long-range stress transmission between cells. *Biophys. J.* **104**, 1410–1418 (2013).

21. Sabeh, F., Shimizu-hirota, R. & Weiss, S. J. Protease-dependent versus -independent cancer cell invasion programs : three-dimensional amoeboid movement revisited. *J. Cell Biol.* **185**, 11–19 (2009).

22. Tibbitt, M. W. & Anseth, K. S. Hydrogels as Extracellular Matrix Mimics for 3D Cell Culture. *Biotechnol Bioeng* **103**, 655–663 (2009).

23. Chen, X. D. Extracellular matrix provides an optimal niche for the maintenance and propagation of mesenchymal stem cells. *Birth Defects Res. Part C - Embryo Today Rev.* **90**, 45–54 (2010).

24. Cavo, M. *et al.* Microenvironment complexity and matrix stiffness regulate breast cancer cell activity in a 3D in vitro model. *Sci. Rep.* **6**, 1–13 (2016).

25. Birgersdotter, A., Sandberg, R. & Ernberg, I. Gene expression perturbation in vitro — A growing case for three-dimensional (3D) culture systems. *Semin. Cancer Biol.* **15**, 405–412 (2005).

26. Charoen, K. M., Fallica, B., Colson, Y. L., Zaman, M. H. & Grinstaff, M. W. Embedded multicellular spheroids as a biomimetic 3D cancer model for evaluating drug and drug-device combinations. *Biomaterials* **35**, 2264–2271 (2014).

27. McKee, C. & Chaudhry, G. R. Advances and challenges in stem cell culture. *Colloids Surfaces B Biointerfaces* **159**, 62–77 (2017).

28. Zhou, Y., Chen, H., Li, H. & Wu, Y. 3D culture increases pluripotent gene expression in mesenchymal stem cells through relaxation of cytoskeleton tension. *J. Cell. Mol. Med.* **21**, 1073–1084 (2017).

29. Antoine, E. E., Vlachos, P. P. & Rylander, M. N. Review of Collagen I Hydrogels for Bioengineered Tissue Microenvironments : Characterization of Mechanics, Structure, and Transport. *Tissue Eng Part B Rev.* **20**, 683–696 (2014).

30. Antoine, E. E., Vlachos, P. P. & Rylander, M. N. Tunable Collagen I Hydrogels for Engineered Physiological Tissue Micro-Environments. *PLoS One* **10**, 1–18 (2015).

31. Doyle, A. D. Generation of 3D collagen gels with controlled, diverse architectures. *Curr Protoc Cell Biol.* **72**, 1–22 (2016).

32. Tronci, G. The application of collagen in advanced wound dressings. in *Advanced Textiles for Wound Care* 363-389 (2019).

33. Holmes, C., Wrobel, J. S., Maceachern, M. P. & Boles, B. R. Collagen-based wound dressings for the treatment of diabetes-related foot ulcers: A systematic review. *Diabetes, Metab. Syndr. Obes. Targets Ther.* **6**, 17–29 (2013).

34. Lai, V. K. *et al.* Microstructural and mechanical differences between digested collagen – fibrin co-gels and pure collagen and fibrin gels. *Acta Biomater.* **8**, 4031–4042 (2012).

35. Frey, C. R., Lai, V. K. & Barocas, V. H. Structural and mechanical differences between pure collagen and fibrin gels. in *ASME 2011 Summer Bioengineering Conference* (2011).

36. Rosinczuk, J., Taradaj, J., Dymarek, R. & Sopel, M. Mechanoregulation of Wound Healing and Skin

Homeostasis. *Biomed Res. Int.* **16**, 1-13 (2016).

37. Evans, N. D., Oreffo, R. O. C., Healy, E., Thurner, P. J. & Hin, Y. Epithelial mechanobiology, skin wound healing, and the stem cell niche. *J. Mech. Behav. Biomed. Mater.* **28**, 397–409 (2013).

38. Tepole, A. B. Computational systems mechanobiology of wound healing. *Comput. Methods Appl. Mech. Engrg.* **314**, 46–70 (2017).

39. Silva, P., Marques, A. P. & Fernandes, M. G. Skin Mechanobiology and Biomechanics: From Homeostasis to Wound Healing. in *Advances in Biomechanics and Tissue Regeneration* 343–360 (2019).

40. Wong, V. W., Akaishi, S., Longaker, M. T. & Gurtner, G. C. Pushing Back : Wound Mechanotransduction in Repair and Regeneration. *J. Invest. Dermatol.* **131**, 2186–2196 (2011).

41. Huang, C., Holfeld, J., Schaden, W., Orgill, D. & Ogawa, R. Mechanotherapy : revisiting physical therapy and recruiting mechanobiology for a new era in medicine. *Trends Mol. Med.* **19**, 555–564 (2013).

42. Ng, J. L., Kersh, M. E., Kilbreath, S. & Tate, M. K. Establishing the Basis for Mechanobiology-Based Physical Therapy Protocols to Potentiate Cellular Healing and Tissue Regeneration. *Front. Physiol* **8**, 1-13 (2017).

43. Lee, G., Han, S., Lee, J., Kim, H. & Kim, D. Cancer Mechanobiology : Microenvironmental Sensing and Metastasis. *ACS Biomater. Sci. Eng.* **5**, 3735–3752 (2019).

44. Choudhury, A. R., Gupta, S., Chaturvedi, P. K., Kumar, N. & Pandey, D. Mechanobiology of Cancer Stem Cells and Their Niche. *Cancer Microenviron.* **12**, 17–27 (2019).

45. Levental, K. R. *et al.* Matrix Crosslinking Forces Tumor Progression by Enhancing Integrin signaling. *Cell* **139**, 891–906 (2009).

46. Dongre, A. & Weinberg, R. A. New insights into the mechanisms of epithelial–mesenchymal transition and implications for cancer. *Nat. Rev. Mol. Cell Biol.* **20**, 69-84 (2019).

47. Gkountela, S. & Aceto, N. Stem-like features of cancer cells on their way to metastasis. *Biol. Direct* **11**, 1–14 (2016).

48. Coceano, G. *et al.* Investigation into local cell mechanics by atomic force microscopy mapping and optical tweezer vertical indentation. *Nanotechnology* **27**, 1-10 (2016).

49. Liu, X. *et al.* Epithelial-type systemic breast carcinoma cells with a restricted mesenchymal transition are a major source of metastasis. *Sci. Adv.* **5**, 1-18 (2019).

50. Alibert, C. *et al.* Are cancer cells really softer than normal cells ? *Biol. Cell* **109**, 167–189 (2017).

51. Quan, F. & Kim, K. S. Medical applications of the intrinsic mechanical properties of single cells. *Acta Biochim Biophys Sin* **48**, 865–871 (2016).

52. Lekka, M. Discrimination Between Normal and Cancerous Cells Using AFM. *BioNanoSci* **6**, 65–80 (2016).

53. Chaffer, C. L., Juan, B. P. S., Lim, E. & Weinberg, R. A. EMT, cell plasticity and metastasis. *Cancer Metastasis Rev.* **35**, 645–654 (2016).

54. Yallapu, M. M. *et al.* The Roles of Cellular Nanomechanics in Cancer Murali. *Med Res Rev* **35**, 198–223 (2015).

55. Chaudhuri, P. K., Low, B. C. & Lim, C. T. Mechanobiology of Tumor Growth. *Chem. Rev.* **118**, 6499–6515 (2018).

56. Goetz, J. G. *et al.* Biomechanical remodeling of the microenvironment by stromal Caveolin-1 favors tumor invasion and metastasis Jacky. *Cell* **146**, 148–163 (2011).

57. Paul, C. D. *et al.* Cancer cell motility: lessons from migration in confined spaces. *Nat Rev Cancer* **17**, 131–140 (2017).

58. Manuscript, A. Chemotaxis in cancer. **11**, 573–587 (2014).

59. Biondo, M. *et al.* The Dynamics of Aerotaxis in a Simple Eukaryotic Model. *Front. Cell Dev. Biol.* **9**, 1–14 (2021).

60. Lo, C. M., Wang, H. B., Dembo, M. & Wang, Y. L. Cell movement is guided by the rigidity of the substrate. *Biophys. J.* **79**, 144–152 (2000).

61. DuChez, B. J., Doyle, A. D., Dimitriadis, E. K. & Yamada, K. M. Durotaxis by Human Cancer Cells. *Biophys. J.* **116**, 670–683 (2019).

62. Espina, J. A., Marchant, C. L. & Barriga, E. H. Durotaxis: the mechanical control of directed cell migration. *FEBS J.* 1-19 (2021).

63. Dunn, G. A. & Ebendal, T. Contact guidance on oriented collagen gels. *Exp. Cell Res.* **111**, 475–479 (1978).

64. Kim, J. *et al.* The mechanics and dynamics of cancer cells sensing noisy 3D contact guidance. *PNAS* **118**, 1-8 (2021).

65. Vincent, L. G., Choi, Y. S., Alonso-Latorre, B., del Álamo, J. C. & Engler, A. J. Mesenchymal stem cell durotaxis depends on substrate stiffness gradient strength. *Biotechnol. J.* **8**, 472–484 (2013).

66. Hartman, C. D., Isenberg, B. C., Chua, S. G. & Wong, J. Y. Vascular smooth muscle cell durotaxis depends on extracellular matrix composition. *Proc. Natl. Acad. Sci. U. S. A.* **113**, 11190–11195 (2016).

67. Chang, C. Y. & Lin, C. C. Hydrogel models with stiffness gradients for interrogating pancreatic cancer cell fate. *Bioengineering* **8**, 1–18 (2021).

68. Isomursu, A. *et al.* Negative durotaxis: cell movement toward softer environments. *bioRxiv* 2020.10.27.357178 (2020).

69. Rens, E. G. & Merks, R. M. H. Cell Shape and Durotaxis Explained from Cell-Extracellular Matrix Forces and Focal Adhesion Dynamics. *iScience* **23**, 1-17 (2020).

70. Yang, S. & Plotnikov, S. V. Mechanosensitive regulation of fibrosis. *Cells* **10**, 1-16 (2021).

71. Sunyer, R. & Trepat, X. Durotaxis. *Curr. Biol.* **30**, R383–R387 (2020).

72. Whang, M. & Kim, J. Synthetic hydrogels with stiffness gradients for durotaxis study and tissue engineering scaffolds. *Tissue Eng. Regen. Med.* **13**, 126–139 (2016).

73. Harland, B., Walcott, S. & Sun, S. X. Adhesion Dynamics and Durotaxis in Migrating Cells. *Biophys. J.* **100**, 1-21 (2011).

74. Wagner, K. *et al.* Colloidal crystals of compliant microgel beads to study cell migration and mechanosensitivity in 3D. *Soft Matter* **15**, 9776–9787 (2019).

75. Hadjipanayi, E., Mudera, V. & Brown, R. A. Guiding cell migration in 3D: A collagen matrix with graded directional stiffness. *Cell Motil. Cytoskeleton* **66**, 121–128 (2009).

76. Kotlarchyk, M. A., Shreim, S. G., Alvarez-elizondo, M. B., Estrada, L. C. & Botvinick, E. L. Concentration Independent Modulation of Local Micromechanics in a Fibrin Gel. **6**, 1-12 (2011).

77. Nuhn, J. A. M., Perez, A. M. & Schneider, I. C. Contact guidance diversity in rotationally aligned collagen matrices. *Acta Biomater.* **66**, 248–257 (2018).

78. Leclech, C. & Villard, C. Cellular and Subcellular Contact Guidance on Microfabricated Substrates. *Front. Bioeng. Biotechnol.* **8**, 1–30 (2020).

79. Kim, J. *et al.* The mechanics and dynamics of cancer cells sensing noisy 3D contact guidance. *Proc. Natl. Acad. Sci. U. S. A.* **118**, 1–8 (2021).

80. Ramirez-San Juan, G. R., Oakes, P. W. & Gardel, M. L. Contact guidance requires spatial control of leading-edge protrusion. *Mol. Biol. Cell* **28**, 1043–1053 (2017).

81. Provenzano, P. P., Inman, D. R., Eliceiri, K. W., Trier, S. M. & Keely, P. J. Contact guidance mediated three-dimensional cell migration is regulated by Rho/ROCK-dependent matrix reorganization. *Biophys. J.* **95**, 5374–5384 (2008).

82. Kubow, K. E., Shuklis, V. D., Sales, D. J. & Horwitz, A. R. Contact guidance persists under myosin inhibition due to the local alignment of adhesions and individual protrusions. *Sci. Rep.* **7**, 1–15 (2017).

83. Thrivikraman, G. *et al.* Cell contact guidance via sensing anisotropy of network mechanical resistance. *Proc. Natl. Acad. Sci. U. S. A.* **118**, 1–11 (2021).

84. Nam, E., Lee, W. C. & Takeuchi, S. Formation of Highly Aligned Collagen Nanofibers by Continuous Cyclic Stretch of a Collagen Hydrogel Sheet. *Macromol. Biosci.* **16**, 995–1000 (2016).

85. Ray, A., Slama, Z. M., Morford, R. K., Madden, S. A. & Provenzano, P. P. Enhanced Directional Migration of Cancer Stem Cells in 3D Aligned Collagen Matrices. *Biophys. J.* **112**, 1023–1036 (2017).

86. Cicuta, P. & Donald, A. M. Microrheology : a review of the method and applications. *Soft Matter* **3**, 1449–1455 (2007).

87. Waigh, T. A. Microrheology of complex fluids. *Rep. Prog. Phys.* **68**, 685–742 (2005).

88. Mizuno, D., Head, D. A., MacKintosh, F. C. & Schmidt, C. F. Active and passive microrheology in equilibrium and nonequilibrium systems. *Macromolecules* **41**, 7194–7202 (2008).

89. Robertson-Anderson, R. M. Optical Tweezers Microrheology: From the Basics to Advanced Techniques and Applications. *ACS Macro Lett.* **7**, 968–975 (2018).

90. Brau, R. R. *et al.* Passive and active microrheology with optical tweezers. *J. Opt. A Pure Appl. Opt. 9* **9**, 103–112 (2007).

91. Flyvbjerg, H. & Introduction, I. Power spectrum analysis for optical tweezers. **75**, 594–612 (2004).

92. Horst, A. Van Der & Forde, N. R. Power spectral analysis for optical trap stiffness calibration from high-speed camera position detection with limited bandwidth. **18**, 7670–7677 (2010).

93. Tassieri, M. Linear microrheology with optical tweezers of living cells 'is not an option'! *Soft Matter* **11**, 5792–5798 (2015).

Chapter 2: Dermal fibroblasts and triple-negative mammary epithelial cancer cells differentially stiffen their local matrix

Alicja Jagiełło[1], Micah Lim[1], Elliot Botvinick[1,2,3,4]

[1] Department of Biomedical Engineering, University of California Irvine, Irvine, CA, 92697-2730, United States

[2] Beckman Laser Institute and Medical Clinic, University of California Irvine, Irvine, CA, 92612, United States

[3] Department of Surgery, University of California Irvine, 333 City Boulevard, Suite 700, Orange, CA, 92868, United States

[4] The Edwards Lifesciences Foundation Cardiovascular Innovation and Research Center, University of California Irvine, Irvine, CA, 92697-2730, United States

2.1. Abstract

The bulk measurement of extracellular matrix (ECM) stiffness is commonly used in mechanobiology. However, past studies by our group show that peri-cellular stiffness is quite heterogeneous and divergent from the bulk. We use optical tweezers active microrheology (AMR) to quantify how two phenotypically distinct migratory cell lines establish dissimilar patterns of peri-cellular stiffness. Dermal fibroblasts (DFs) and triple-negative human breast cancer cells MDA-MB-231 (MDAs) were embedded within type 1 collagen (T1C) hydrogels polymerized at two concentrations: 1.0 mg/ml and 1.5 mg/ml. We found DFs increase the local stiffness of 1.0 mg/ml T1C hydrogels but, surprisingly, do not alter the stiffness of 1.5 mg/ml T1C hydrogels. In contrast, MDAs predominantly do not stiffen T1C hydrogels as compared to cell-free controls. The results suggest that MDAs adapt to the bulk ECM stiffness, while DFs regulate local stiffness to levels they intrinsically prefer. In other experiments, cells were treated with transforming growth factor-b1 (TGF-b1), glucose, or ROCK inhibitor Y27632, which have known effects on DFs and MDAs related to migration, proliferation, and contractility. The results show that TGF-b1 alters stiffness anisotropy, while glucose increases stiffness magnitude around DFs but not MDAs and Y27632 treatment inhibits cell-mediated stiffening. Both cell lines exhibit an elongated morphology and local stiffness anisotropy, where the stiffer axis depends on the cell line, T1C concentration, and treatment. In summary, our findings demonstrate that AMR reveals otherwise masked mechanical properties such as spatial gradients and anisotropy, which are known to affect cell behavior at the macro-scale. The same properties manifest with similar magnitude around single cells.

2.2. Introduction

Bulk stiffness of the extracellular matrix (ECM) has been previously shown to regulate cellular processes and correspond with invasiveness of cancer cells [1–3]. ECM stiffness is a measure of ECM resistance to deformation and is primarily regulated by ECM remodeling, strain stiffening, degradation and deposition carried out by cells in response to a variety of biochemical cues [1]. Factors including aging, genetic mutations, diabetes and other medical conditions have also been shown to modify mechanical properties of the ECM [4]. The majority of research related to mechanical aspects of cell-ECM interactions relies on measuring the bulk ECM stiffness as a single parameter [5–7], or otherwise equating stiffness with the density or concentration of hydrogels or substrates to which cells are exposed [8,9]. These approaches do not directly measure the stiffness of the peri-cellular region within naturally derived fibrous three-dimensional ECMs, such as those comprising type 1 collagen (T1C) or fibrin. Our laboratory uses optical tweezers active microrheology (AMR) that provides access to the peri-cellular region. In fact, past research in our laboratory has shown that the peri-cellular stiffness on a single cell level can span orders of magnitude [10]. These findings prompted us to investigate how cells remodel their local stiffness in correlation to bulk (e.g., cell-free) ECM stiffness and other mechanical and biochemical cues.

In this study, we use AMR to measure stiffness around two migratory cell types - highly invasive, triple-negative breast cancer cells MDA-MB-231 (MDAs), and normal human dermal fibroblasts (DFs). While highly migratory and dynamic DFs are key regulators of ECM stiffness and composition [11,12], MDAs are thought to be regulated by tissue stiffness, which relates to early screening for breast cancer by detecting elevated breast density and stiffness [13]. Consequently, measuring stiffness around both cell lines is of scientific interest to the field

of mechanobiology. DFs and MDAs were cultured within T1C hydrogels, chosen because T1C is the most abundant component of these cells' ECM [12] and is known to regulate cell processes and behaviors [14,15]. Also, collagens are known to be remodeled and crosslinked during cancer progression [13–15].

In this study, we assess changes in peri-cellular stiffness of MDAs and DFs in response to (1) human transforming growth factor-β1 (TGF-β1), (2) glucose and (3) Y27632. These factors were shown to alter cell migration, proliferation and cell contractility of MDAs and DFs [16–20]. In cancer cells, TGF-β1 was shown to promote immunosuppression, angiogenesis and epithelial-mesenchymal transition (EMT), which are primary mechanisms leading to breast cancer metastasis [13]. Moreover, TGF-β1 was reported to strengthen focal adhesions and result in increased migration of different cancer cell lines, including MDAs [2,18]. Its effect on cell migration was further correlated with cell invasiveness and metastatic potential [17,21]. Addition of TGF-β1 also promotes collagen synthesis in DFs and might even result in differentiation of DFs into myofibroblasts under high tensile stresses [12]. The addition of TGF-β1 to media was therefore expected to increase stiffness around both DFs and MDAs.

Elevated concentrations of glucose were reported to promote cancer cell proliferation, a phenomenon attributed to the Warburg effect which favors aerobic glycolysis over oxidative phosphorylation in cancer cells [22]. Hyperglycemia additionally lowers survival rates in malignant breast cancer patients and mitigates the efficacy of cancer treatments by promoting chemoresistance and aggressiveness of cancer cells including MDAs [4,23], as indicated by their increased proliferation and reduced apoptosis [24]. We therefore assumed that glucose addition to the media would also result in larger peri-cellular stiffness levels. In contrast, the addition of glucose to fibroblasts was previously described

to promote collagen deposition, but reduce both the proliferation and migration rate of fibroblasts, as commonly observed in delayed wound healing responses in diabetic patients [25–28]. Nonetheless, despite reduced migratory capabilities of DFs, contractile properties were shown to be increased in fibroblasts cultured in high glucose media as opposed to low glucose media [28]. Thus, we expected that increased cell contractility should result in elevated peri-cellular stiffness levels as compared to control cells cultured in low glucose media.

Next, we targeted Rho-associated protein kinase (ROCK) that is overexpressed in tumorigenic and metastatic breast cancer cell lines, including MDAs [19,29]. ROCK is primarily responsible for organizing the cell cytoskeleton and stimulating cancer cell metastasis by increasing focal adhesions and disrupting cell-cell junctions. Consequently, ROCK enhances cell contractility, migration and proliferation, all of which promote cancer invasiveness [30]. Inhibition of the ROCK signaling pathway is hence expected to prevent strain stiffening of peri-cellular collagen fibers and consequently reduce peri-cellular stiffness around MDAs. In our experiments, we use the ROCK inhibitor Y27632, which has widely documented anti-invasive, anti-migratory [29,31] and anti-proliferative [9] properties in breast cancer studies. Previous studies in our laboratory indicate that Y27632 prevents cell contractility and ECM stiffening by DFs [10] and Y27632 was also expected to yield a similar effect on MDAs.

The AMR results described below demonstrate that both MDAs and DFs can adapt to their environment and modify it in response to a variety of mechanical or biochemical factors which were previously shown to either promote or reduce cancer cell invasiveness and fibroblast contractility. Unlike bulk stiffness measurements, experiments at the single cell level allow us also to better explain how cell-ECM interactions are spatially dependent on these different treatments and collagen concentrations.

2.3. Methods

Ethics approval is not required for the methods of this study.

2.3.1. Cell culture

Normal human dermal fibroblasts (DFs) cells were cultured in Dulbecco's Modified Eagle's Medium (DMEM) with low glucose, L-glutamate, and sodium pyruvate (ThermoFisher) with 10% Fetal Bovine Serum (FBS) (Gibco) and 1% penicillin streptomycin (Gibco). All cells were used prior to passage 8.

Human breast cancer cells MDA-MB-231 (MDAs) were cultured in DMEM with high glucose, L-glutamate, and sodium pyruvate (ThermoFisher) with 10% FBS (Gibco) and 1% penicillin streptomycin (Gibco).

2.3.2. Collagen hydrogel preparation

Cells were embedded in type I collagen due to its abundance in the natural ECM of MDAs and DFs. Hydrogels at 1.0 and 1.5 mg/ml concentrations were prepared using type I rat tail telocollagen (Advanced Biomatrix), 10X Phosphate-Buffered Saline (PBS) with added calcium and magnesium (ThermoFisher), 10X DMEM (Sigma), 10X reconstitution buffer prepared as described by Doyle [32], 1 N NaOH (ThermoFisher), 2 μm carboxylated silica microbeads (0.8 mg/ml, Bangs Laboratories), and cells (50 k/ml) in 35 mm glass bottom dishes (MatTek). Each hydrogel was allowed to polymerize for 30 min in a standard tissue culture incubator at 37 °C and 5% CO_2 prior to adding 2 ml of media. Media was supplemented with 25 mM HEPES (ThermoFisher) and different treatments: 10 ng/ml TGF-β1 (PeproTech), 25 mM glucose (Sigma) or 20 μM Y27632 (PeproTech). Gels were incubated for 24 h prior to AMR measurements.

2.3.3. Active microrheology (AMR)

The AMR system used in our laboratory is described in **Chapter 1.3.1** and presented in **Figure 1.5**. During the sinusoidal oscillations of the trapping beam (x_T), position of the bead (x_B) in the direction of bead oscillation is recorded by the detQPD, which provides analog signals proportional to the displacement of the bead. Ignoring any small off axis movements of the bead, we can treat the experiment as a one-dimensional problem. The applied optical force acting in the direction of bead oscillation (either *X'* or *Y'* direction) is expressed by:

$$f(t) = k_T\,(x_T(t) - x_B(t)), \qquad (1)$$

where k_T corresponds to the trap stiffness that is calculated during calibration.

Local complex material response is described in the Fourier space as

$$\alpha^*(\omega) = X_B(\omega) \;/\; (F(\omega) - k_T X_B(\omega)), \qquad (2)$$

where X_B and F are the Fourier transforms of x_B and f. Stiffness κ is then defined as the real component of $1/\alpha^*(\omega)$. Under the assumption of a continuum, the complex shear modulus $G^*(\omega)$ can be defined as

$$G^*(\omega) = 1 \;/\; 6\pi r\alpha^*(\omega), \qquad (3)$$

where r corresponds to the radius of the bead (1 μm). *G'* and *G''* for DFs and MDAs are included in **Suppl. Figures 3 and 4**, respectively, and the data shows the hydrogels are viscoelastic having storage modulus greater in magnitude than loss modulus, at the probed frequency.

Our AMR system is controlled by custom software developed in our laboratory and described in [10]. It allows for precise stage positioning to center a microbead in the optical trap. Each bead was probed by the optical trap oscillating at frequencies of 20 (**Suppl. Figure 1**), 50 and 100 Hz (**Suppl. Figure 2**) in both horizontal (*X'*) and vertical (*Y'*) axis. 50 Hz measurements were repeated twice. Each bead was probed for 5 s at each frequency for a total of 40 s measurement time. In all hydrogels, probed beads were only treated as outliers and discarded if, during the AMR measurements, bead centering was observed to be inaccurate or stiffness values were either negative or exceeded 60 nN/μm.

For stiffness measurements, collagen gels were incubated on the microscope stage using a Culture Dish Incubator (Warner Instruments) and an Objective Warmer (Warner Instruments) and allowed 20 min to equilibrate to 37 °C prior to AMR. At least 30 beads in close proximity to each cell were analyzed. The AMR system and stage incubator were turned on at least 1.5 h prior to system calibration and measurements on collagen gels to alleviate effects of alignment drift as the system comes to temperature.

κ was measured around 10 cells per condition in both 1.0 and 1.5 mg/ml T1C hydrogels. Cells included in the study had to meet the following criteria: a) cells had to be predominantly in focus in the *XY* plane; b) cells had to be isolated from other cells by few camera fields-of-views and c) cells had to exhibit elongated morphology, characteristic of both cell lines. Up to two cells were studied per hydrogel, with probing at least 30 beads located within an in-focus image area bounded by 100 μm from the cell surface (in plane) and +/- 6 μm in depth. For each bead, κ was measured along both the *X'* and *Y'* axes with respect to the image field-of-view. κ measurements were then projected onto a new set of

axes (X and Y) by rotating the κ values by the cell orientation angle, as described in Chapter 2.3.5.

2.3.4. System validation and calibration

The AMR system was calibrated in water prior to each experiment. A frequency sweep was conducted for at least 3 beads oscillated first in X' (horizontal) and then in Y' (vertical) direction, as previously described in [10]. Briefly, a bead is trapped by both lasers and brought to a height of 35 μm above the glass. With great care, both lasers are co-aligned in X',Y', and Z', and individually centered on the bead. Next, the detQPD and trapQPD are positioned by a 2-axis mount until mean voltages have a value of zero. Brownian motion of each bead is recorded for 30 s and analyzed using the power spectrum method, as described in **Chapter 1.3.2.** Trap stiffness k_t was found separately in the X' and Y' direction. Afterwards, a position sweep of the bead was used to obtain the detQPD voltage-to-bead displacement factor β for each axis. Average k_t and β values specific for each axis of oscillation were then used for AMR measurements in water (for calibration validation) as well as T1C hydrogels.

The viscosity η of water is known to be equal to 0.69 mPa·s at 37 °C [33]. AMR measurements at $f = [10\ 20\ 50\ 75\ 100]$ Hz were conducted in water samples maintained at 37 °C. Experimentally determined viscosity values were calculated as $\eta = G"/2\pi f$ and compared to the theoretical value (0.69 mPa·s). Based on 8 separate calibrations at 50 Hz, each with at least 3 different beads, η values differed from the theoretical value, on average, by 3.95% in the X' and 5.64% in the Y' direction.

Errors due to automated motorized-stage and objective lens positioning were characterized. Beads were suspended in 1.0 mg/ml T1C hydrogels maintained at 37°C. In a first experiment, we selected 29 beads across several fields of view and the automated system centered each bead to conduct AMR measurements. The purpose of this experiment was to determine errors in κ due to stage/objective positioning. In a second experiment the system positioned each of 32 beads and made 5 repeated measurements without moving the stage. The purpose of this experiment was to determine errors due to the system exclusive of bead positioning. For the first experiment, measurement error in κ, defined as standard deviation/mean $\cdot$ 100%, was equal to 7.52% and 6.56% along the X' and Y' direction, respectively. For the second experiment, error was a 4.03% and 4.56% in the X' and Y' direction respectively.

Frequency AMR sweeps at 10, 20, 50, 75 and 100 Hz indicated an increase in stiffness with frequency of bead oscillations both in X' (30 beads, $p << 0.01$) and Y' direction (29 beads, $p << 0.01$), based on the Friedman test for repeated measures. These findings are in agreement with widely reported frequency effect on stiffness levels in microrheological studies [34–36].

2.3.5. Cell orientation assessment

AMR measurements around each cell were divided into several fields-of-view. Brightfield images of the cells were taken before AMR measurements on each field-of-view using an EO-4010 Monochrome USB 3.0 Camera (Edmund Optics) incorporated in our AMR system. Brightfield images were then processed in MATLAB (The MathWorks Inc.) using the image processing toolbox. Cell morphology was quantified by manual tracing, and MATLAB functions computed angle of cell orientation, position of the cell centroid and long and short

axes of the cell, per field-of-view. Further, spatial location of each bead with respect to the position and orientation of each cell was calculated in MATLAB. The shortest distance between the bead and cell profile was found by comparing pixel coordinates of each bead probed in a given field-of-view with the pixel coordinates of the manually traced cell shape. Distance in pixels was converted into micrometers. Angular position θ from -180 to 180° relative to the X axis was found by calculating the angle between the pixel position of the bead and centroid of the cell and subtracting the angle of cell orientation. The coordinate system was then folded upon itself along the X axis, under the assumption of symmetry, thus θ ranged from 0 to 180°.

After AMR measurements, brightfield and reflection confocal images of the cells were acquired every 30 s for an additional 10 min. Confocal images were acquired using the 488 nm laser of the Fluoview 1200 laser scanning confocal microscope (Olympus) integrated into the AMR system. Analysis of the image series identifies direction of cell migration and consequently, the leading and trailing edge of the cells. If the direction of cell migration was not obvious during these 10 min, then brightfield images were compared with brightfield images taken at the start of the AMR measurements, which typically occurred 30-40 min earlier. Beads distal to the cell served as fiducial markers for cell migration.

2.3.6. Statistical analyses

Data was not normally distributed ($p << 0.01$, Kolmogorov-Smirnov test) necessitating non-parametric statistical analyses. The Wilcoxon test was used for the comparison of correlated measurements in X and Y directions (**Figure 2.1D**) and the Kruskal-Wallis test for the comparison of multiple groups, with the post-hoc Tukey-Kramer

test to compare specific groups (**Suppl. Tables 2, 4-6**). Statistical testing was conducted at a significance level of 0.05. p values smaller than 0.01 were reported as $p << 0.01$ and p values larger than 0.99 were reported as $p > 0.99$.

2.4. Results

ECM mechanical stiffness (κ) was measured using optical tweezers AMR (**Figure 2.1A**) [10]. κ was measured around each cell along both horizontal (X') and vertical (Y') axes of the image field-of-view. Cells rarely align with the X' and Y' axes, so stiffness was projected onto two new axes aligning with the long (X) and short (Y) axis of each cell, with the origin at the cell centroid (**Figure 2.1B-C**). Stiffnesses in this new coordinate system are denoted as κ_X and κ_Y.

2.4.1. Effects of ECM concentration and treatments on T1C hydrogel stiffness

Stiffness distributions are plotted in **Figure 2.1E-G**. These plots aggregate κ_X and κ_Y for each probed bead. The aggregate stiffnesses are referred to as κ. Cell-free T1C hydrogels having an initial concentration of 1.0 mg/ml (1.0T1C) or 1.5 mg/ml (1.5T1C) were probed (**Figure 2.1E, Suppl. Table 2.1**). Stiffnesses of the gels were investigated 24 h after sample preparation and addition of treatment media. Treatment media included Dulbecco's Modified Eagle's Medium (DMEM) supplemented with either 25 mM glucose, 10 ng/ml TGF-β1 or 20 μM Y27632. κ of cell-free hydrogels in control (untreated) conditions increased with concentration ($p << 0.01$; n_{beads} = 136 for 1.0T1C, n_{beads} = 127 for 1.5T1C). Treatment conditions did not significantly affect κ within 1.0T1C (p = 0.79) or 1.5T1C (p = 0.32) hydrogels.

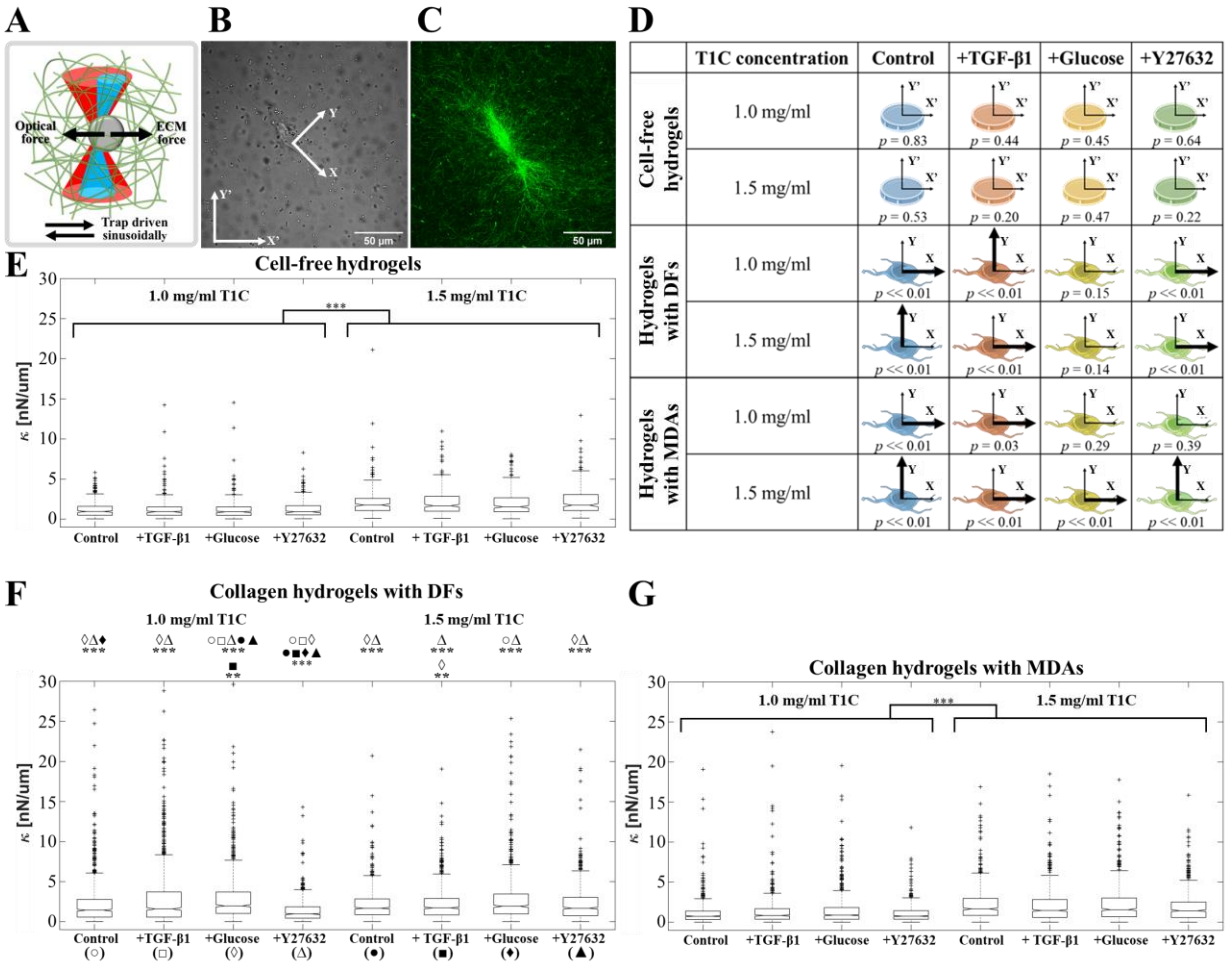

Figure 2.1. Aggregated stiffness values assessed by optical tweezers active microrheology. (A) Diagram of optical tweezers active microrheology. The optical tweezers beam (red) is oscillated sinusoidally in the horizontal (*X'*) or vertical (*Y'*) direction with respect to the field-of-view. The optical trap exerts oscillatory forces on a probed microbead (gray), while ECM (green) resists the bead displacement. The bead displacement is probed by a stationary detection beam (blue). (B) Brightfield and (C) reflection confocal microscopy images of a DF embedded in a 1.0T1C hydrogel. Stiffness measured along the *X'* and *Y'* axes is projected onto axes corresponding to the long (*X*) and short (*Y*) axes of the cell with origin at the cell centroid. (D) Graphical representation of stiffness anisotropy. Thicker arrows indicate the stiffer axis. (E-G) Box plots comparing aggregated κ_X and κ_Y values between treatments and T1C concentrations in (E) cell-free hydrogels and around (F) DFs and (G) MDAs. *** $p << 0.01$ and ** $p < 0.05$ for (E-G).

Next, ECM stiffness around DFs and MDAs was measured at the two T1C concentrations and three treatment conditions. Statistical testing results are found in **Suppl. Table 2.2.** *p* values smaller than 0.01 were reported as $p << 0.01$ and *p* values larger than 0.99 were reported as $p > 0.99$. **Figure 2.1F** summarizes results for DFs. For 1.0T1C

hydrogels, κ was greater in control and treated DF cultures as compared to cell-free hydrogels, with the exception of Y27632 treatment, which did not differ from the cell-free condition ($p > 0.99$). As compared to DF control conditions, treatment with Y27632, glucose or TGF-β1 decreased ($p << 0.01$), increased ($p << 0.01$) or did not significantly change ($p = 0.65$) stiffness, respectively. For DFs in 1.5T1C hydrogels, significant differences in stiffness were not detected between all treatment and cell-free conditions (**Suppl. Table 2.2**). Differences in κ were not detected between paired treatment groups at the two T1C concentrations (except for Y27632), which was surprising given that κ in cell-free hydrogels increased with T1C concentration.

For MDA cultures, κ in control and treatment groups at either T1C concentration was not significantly different from respective cell-free conditions, with the exception of Y27632 treatment in 1.5T1C hydrogels, for which κ decreased ($p << 0.01$, **Suppl. Table 2.2, Figure 2.1G**). For all treatments κ increased with T1C concentration ($p << 0.01$).

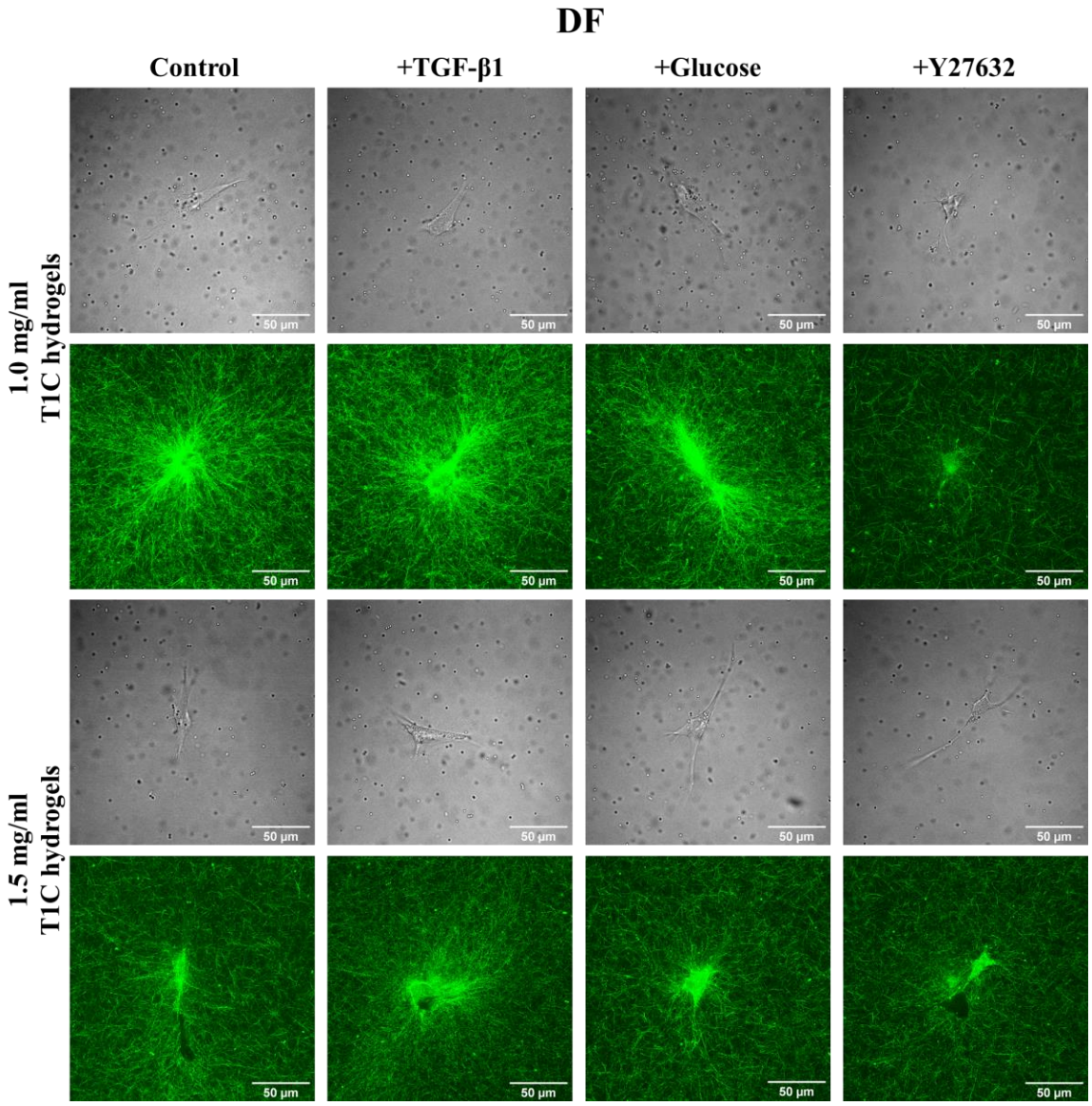

Figure 2.2. Brightfield and reflection confocal microscopy images of DFs embedded in T1C hydrogels with 2 µm diameter silica microbeads.

Figures 2.2 and 2.3 show that the two cell types take on different morphologies in T1C concentration and treatment conditions. These morphologies can be described as elongated, and MDAs appear less contractile as compared to DFs. We investigated differences in stiffness anisotropy around these cells (**Figure 2.1D, Suppl. Table 2.3**). In **Figure 2.1D**, the axis of greater stiffness is indicated by the thicker arrow. Differences between κ_X *and* κ_Y were tested by the Wilcoxon signed rank test. Anisotropy was not detected

in cell-free conditions. For both control DFs and MDAs, the stiffer axis transitioned from *X* to *Y* with increasing T1C concentration. Treatment conditions promoted distinct cell-line and T1C concentration dependent trends in stiffness anisotropy.

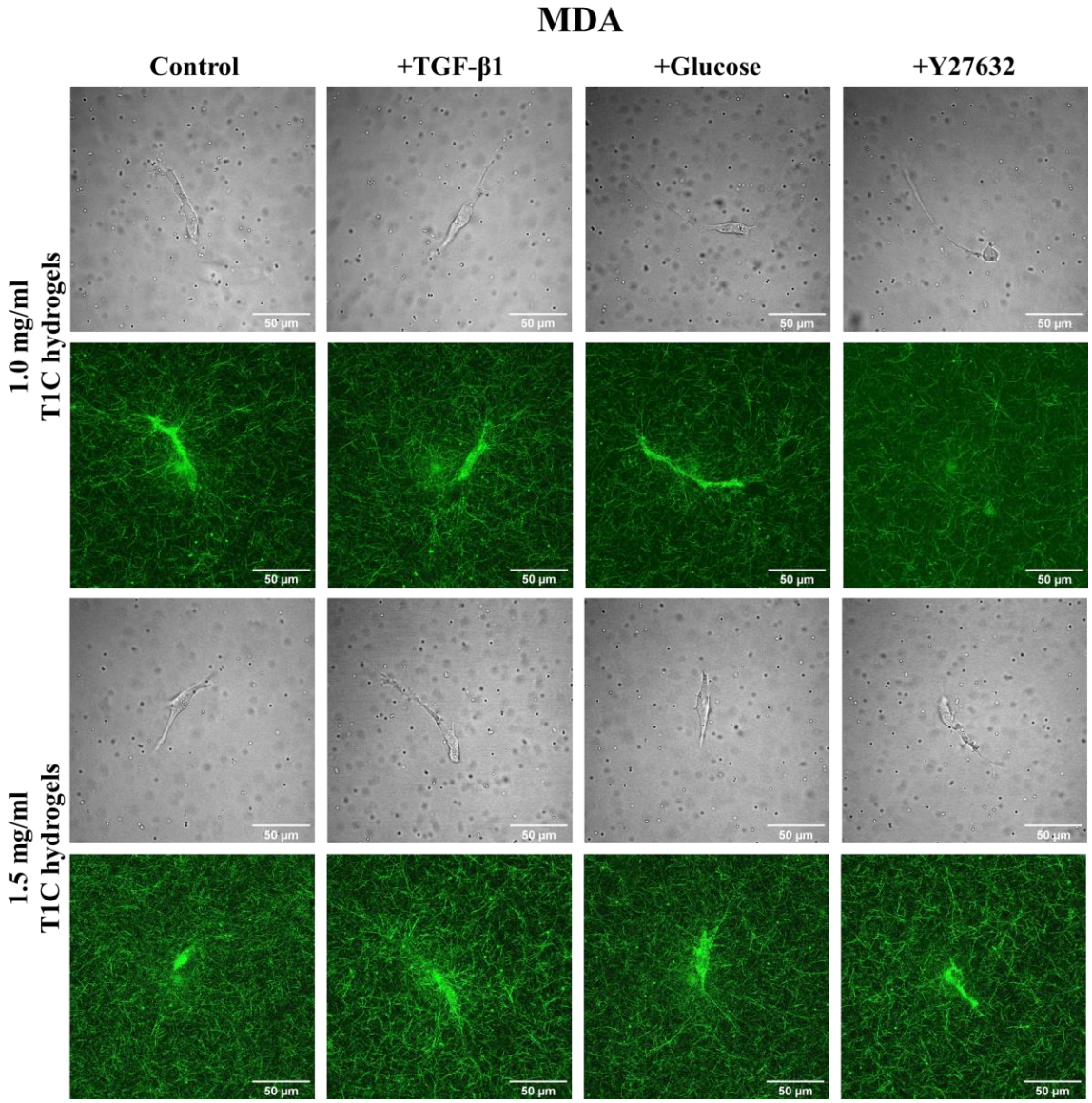

Figure 2.3. Brightfield and reflection confocal microscopy images of MDAs embedded in T1C hydrogels with 2 µm diameter silica microbeads.

2.4.2. Peri-cellular stiffness distributions and anisotropy

κ_X and κ_Y values in **Figure 2.1** are aggregated for all beads independent of location relative to their respective cell. We next examined the spatial distribution of κ_X and κ_Y relative to DFs and MDAs. Stiffness values were not normally distributed ($p << 0.01$ by Kolmogorov–Smirnov testing) and compared using the Kruskal-Wallis test with Tukey-Kramer post-hoc testing at a significance level of 0.05. Results of the Tukey-Kramer tests are included in **Suppl. Tables 2.4-6**. Our method for graphing κ stiffness distribution is illustrated in **Figure 2.4A**. Each probed bead is assigned two coordinates. The first coordinate is the shortest distance between the bead and cell profile. The second coordinate is the angular position θ relative to the X axis in the counterclockwise direction (with origin at the cell centroid). These two coordinates place each bead within one of the eighteen annular bins. The coordinate system was folded upon itself along the X axis, under the assumption of symmetry. By definition, beads having θ: 0-30° are located in the region of the cell leading edge (front), while beads having θ: 150-180° are located in the region of the trailing edge (back). The inner annulus from 0 to 20 μm is considered the peri-cellular region, previously shown to stiffen around DFs cultured in T1C hydrogels [10]. **Figure 2.4B-C** summarizes the spatial distribution of κ surrounding DFs and MDAs at both T1C concentrations and all treatment groups. Each bin in **Figure 2.4B-C** is shaded according to the median value of κ in that bin. Each point is a single probed bead and color-coded for κ.

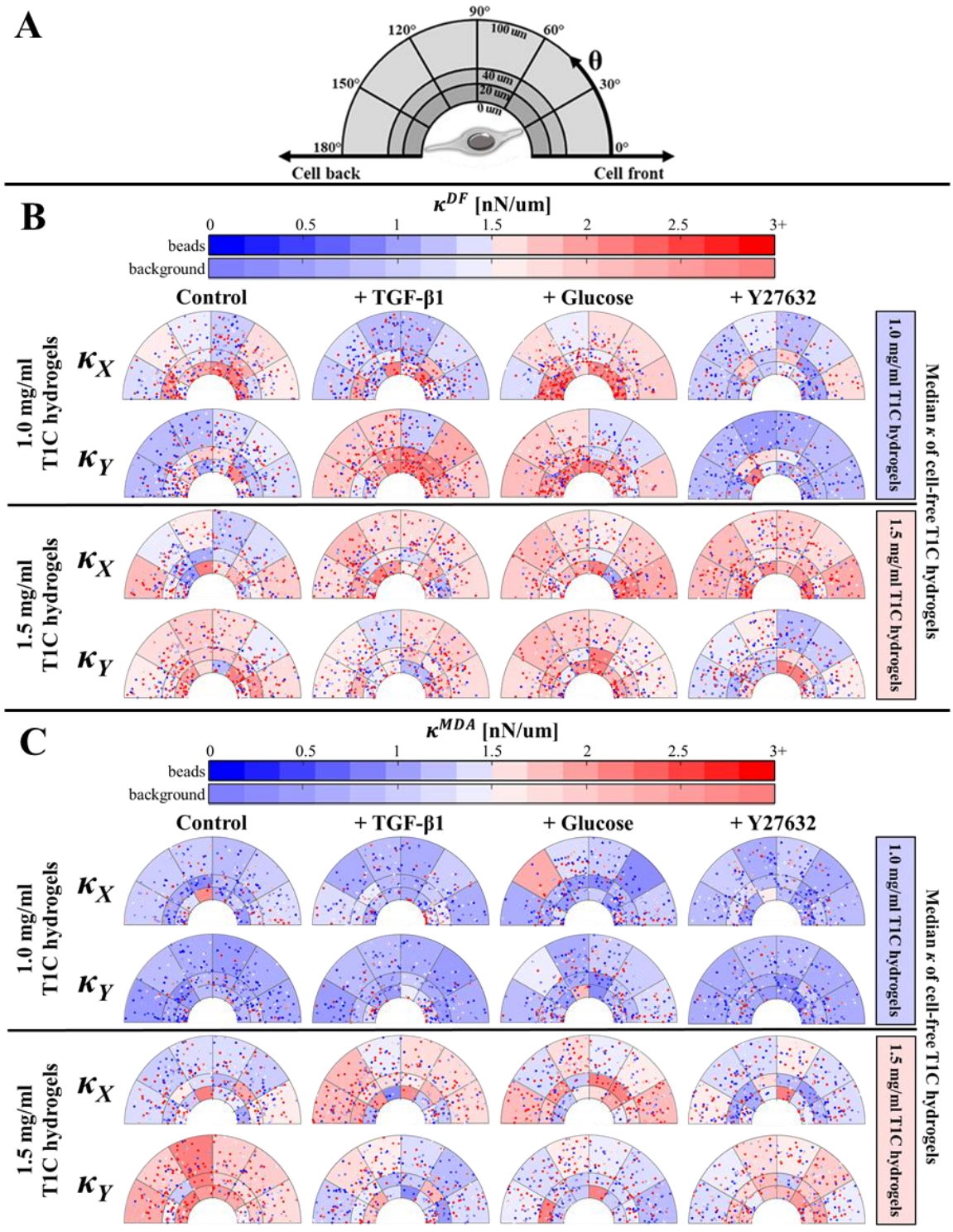

Figure 2.4. Hydrogel stiffness distributions for cell type, T1C concentration, and treatment groups. (A) Graphical representation of coordinate system to discretize ECM region around a cell. This coordinate system has the origin at the cell centroid with 0° pointing towards the leading edge of the cell. The coordinate system was folded upon itself along the *X* axis under the assumption of symmetry. Distribution of κ_X and κ_Y around (B) DFs and (C) MDAs in 1.0T1C and 1.5T1C. Bin background color is shaded according to the median value of κ in each bin (background color bar). Each data point is a single probed bead, color-coded for κ (beads color bar).

2.4.3. DFs increase local ECM stiffness of 1.0T1C but not 1.5T1C hydrogels

We first considered κ_X under control conditions, where κ_X is stiffness in the direction parallel to cell elongation. Peri-cellular (inner annulus) κ_X values were comparable between T1C concentrations ($p = 0.85$, **Suppl. Table 2.5**). This observation holds for the distal (outer annulus) region ($p > 0.99$, **Suppl. Table 2.6**). These results are surprising considering that stiffnesses of cell-free hydrogels increased with T1C concentration (**Figure 2.1E**). For 1.0T1C hydrogels, κ_X in the peri-cellular region was greater than that of cell free hydrogels ($p << 0.01$), a finding that did not hold for the distal region ($p = 0.29$) and is suggestive of cell-mediated peri-cellular stiffening. For 1.5T1C hydrogels, κ_X was not significantly different from κ_X of cell free hydrogels in either peri-cellular ($p > 0.99$) or distal region ($p > 0.99$).

κ_Y, which is defined as stiffness in the direction perpendicular to cell elongation, showed T1C concentration dependency in the distal ($p << 0.01$), but not the peri-cellular region ($p > 0.99$). Our results suggest that DFs in 1.0T1C, but not in 1.5T1C hydrogels, preferentially stiffen ECM in the direction of cell migration.

2.4.4. MDAs do not increase local stiffness of T1C hydrogels

Control MDAs produced a relatively mild effect on their ECM (**Figure 2.4C**). Both κ_X and κ_Y increased with T1C concentration ($p << 0.01$, **Suppl. Table 2.4**). However, κ_X was not different from cell-free conditions at either T1C concentration in both peri-cellular (**Suppl. Table 2.5**) and distal (**Suppl. Table 2.6**) regions. Similarly, κ_Y around MDAs did not differ from κ_Y of cell-free hydrogels, with the exception of κ_Y in the distal region in 1.0T1C, which was significantly reduced ($p = 0.04$), but only by 0.41 nN/μm when comparing medians. Overall, MDAs did not alter their local stiffness to the extent observed for DFs.

Comparison between cell lines showed that DFs established higher ECM stiffness values than MDAs when cultured in 1.0T1C hydrogels ($p << 0.01$). A difference in ECM stiffness was not detected between cell types cultured in 1.5T1C hydrogels, nor were these stiffness values different from that of cell-free 1.5T1C hydrogels (**Suppl. Table 2.2**). The degree of stiffness anisotropy was similar for both cell lines and dependent on T1C concentration. Both cell lines established an ECM that is stiffer in *X* than *Y* in 1.0T1C hydrogels ($p << 0.01$), but stiffer in *Y* than *X* in 1.5T1C hydrogels ($p << 0.01$, **Figure 2.1D**).

2.4.5. TGF-β1-treated cells establish different stiffness anisotropy than control cells

Treatment of DFs and MDAs with TGF-β1 was expected to promote peri-cellular stiffening based on the role of TGF-β1 in DF-stimulated collagen synthesis and EMT initiation in MDAs. For DFs in 1.0T1C hydrogels, the peri-cellular region stiffened along the *X* and *Y* directions when compared to cell-free conditions, but κ_X and κ_Y did not differ from control DF hydrogels (**Suppl. Table 2.5**). In the distal region, κ_Y but not κ_X was higher than respective stiffnesses of both cell-free and control DF hydrogels (**Suppl. Table 2.6**). For DFs in 1.5T1C hydrogels, treatment with TGF-β1 did not result in significant changes in κ_X or κ_Y when compared to either cell-free hydrogels or control DF hydrogels in either region or direction (**Suppl. Table 2.5-6**).

For MDAs, a treatment effect was observed only in the distal region along the *Y* direction in 1.5T1C hydrogels. There, κ_Y around cells was significantly lower than around control cells ($p << 0.01$), but not different from cell-free hydrogels ($p = 0.77$, **Suppl. Table 2.6**).

Stiffness values around cells treated with TGF-β1 exhibited a reversed-directional bias in stiffness anisotropy. As shown above, both control DFs and control MDAs cultured in 1.0T1C hydrogels established an ECM stiffer in the *X* than *Y* direction ($\kappa_X > \kappa_Y$). The opposite was true in 1.5T1C hydrogels ($\kappa_X < \kappa_Y$). However, TGF-β1-treated DFs showed the reverse dependency on T1C concentration such that $\kappa_X < \kappa_Y$ in 1.0T1C hydrogels and $\kappa_X > \kappa_Y$ in 1.5T1C hydrogels ($p << 0.01$, **Figure 2.1D**). TGF-β1-treated MDAs established an ECM that is stiffer in the *X* direction at both T1C concentrations ($p << 0.01$). These findings indicate that TGF-β1 promotes diverse and anisotropic patterns of κ around both cell lines, with stiffness anisotropy affected more than overall stiffness magnitude.

2.4.6. Glucose-treated DFs, but not MDAs establish stiffer and isotropic ECM

The addition of glucose was expected to increase κ around both cell lines, because glucose was previously reported to promote collagen synthesis by fibroblasts and invasiveness of MDAs [4,24,28,37]. When looking at the overall κ (analyzing all beads probed up to 100 μm from the cell) around DFs in 1.0T1C hydrogels, glucose treatment increased both κ_X and κ_Y as compared to control and cell-free hydrogels (**Suppl. Table 2.4**). Stiffness around glucose-treated DFs in 1.5T1C hydrogels did not differ from that of cell-free hydrogels (**Suppl. Table 2.4**). The overall stiffness around glucose-treated DFs was not significantly different between the two tested T1C concentrations ($p > 0.99$, **Suppl. Table 2.4**). Stiffness anisotropy was not detected at either T1C concentration (**Figure 2.1D**).

MDAs treated with glucose established an isotropic κ distribution within 1.0T1C hydrogels ($p = 0.29$, **Figure 2.1D**) resulting from a stiffening in the *Y* direction as compared to control cells ($p << 0.01$, **Suppl. Table 2.4**). Stiffness around glucose-treated MDAs in 1.5T1C hydrogels was higher in the *X* direction ($p << 0.01$), resulting from an increase in κ_X

(p = 0.04) and a decrease in κ_Y (p << 0.01) as compared to stiffness around control MDAs (**Suppl. Table 2.4**). Interestingly, while κ around glucose-treated MDAs increased with T1C concentration (p << 0.01 in X, p = 0.03 in Y), κ did not differ significantly from the stiffness of corresponding cell-free hydrogels (**Suppl. Table 2.4**). Consequently, glucose might have a less potent, but more complex effect on MDAs than on DFs.

2.4.7. Y27632-treated cells establish an ECM similar in stiffness to cell-free conditions

Y27632 treatment was selected to inhibit cell contractility and thus strain stiffening. Y27632 was previously shown by our group to reduce stiffness in the peri-cellular region of DFs to levels comparable to cell-free regions [10]. In our current study, we first compared DFs peri-cellular κ to the cell-free conditions. We found that peri-cellular κ at either T1C concentration did not differ from κ of cell-free hydrogels following Y27632 treatment (**Suppl. Table 2.5**). A similar result was found for distal regions, with the exception of κ_Y around DFs within 1.5T1C hydrogels, which was lower than stiffness of cell-free hydrogels (p = 0.02, **Suppl. Table 2.6**). We next compared κ around control and Y27632-treated DFs. When considering all beads in all regions, Y27632 treatment resulted in an overall decrease in ECM stiffness around DFs cultured in 1.0T1C hydrogels when compared to control cells (**Suppl. Table 2.4**). For DFs in 1.5T1C hydrogels, stiffness increased in the X direction (p = 0.01), but decreased in the Y direction (p = 0.01) as compared to control cells. However, when considering only the peri-cellular space around DFs treated with Y27632, only κ_X in 1.0T1C hydrogels was different (reduced) from stiffness around control cells (**Suppl. Table 2.5**).

For MDAs treated with Y27632, stiffness did not differ significantly from cell-free conditions with the exception of κ_X in 1.5T1C hydrogels, which was lower than stiffness of cell-free hydrogels (p = 0.01, **Suppl. Table 2.4**). We did not observe a difference in κ_X or κ_Y

between control and Y27632-treated cells in either peri-cellular or distal regions (**Suppl. Table 2.5-2.6**), which was not surprising given the insignificant strain stiffening by control cells (stiffness around control MDAs was not significantly different from cell-free conditions, **Suppl. Table 2.4**).

2.5. Discussion

Cell contractile forces were previously shown by our group to establish highly heterogeneous κ distributions around individual DFs with significant ECM stiffening in the peri-cellular region as compared to cell-free hydrogels [10]. Here, we investigated κ distributions around DFs and invasive triple-negative breast cancer MDAs embedded at two different T1C concentrations. Both cell lines were previously reported to be highly migratory, yet phenotypically and morphologically different [38,39]. Thus, we investigated if and how patterns of κ distribution differ between these two cell lines. In a first set of experiments, we simply cultured these cells in fibrous T1C hydrogels polymerized at 1.0 mg/ml and 1.5 mg/ml. While the concentration of T1C does increase by 50%, the absolute concentration difference is modest as compared to previously published experimental systems that used T1C hydrogels in the range of 0.5-4.0 mg/ml [9,40–43]. DFs were found to be considerably more responsive to the change in concentration than the MDAs – and in some surprising ways. For example, stiffness in cell-free hydrogels increases with T1C concentration (by 84%; comparing median values) as expected and verified by both AMR (**Figure 2.1E**) and macrorheology [9,44,45]. As replicated in previous work [10], we found DFs increase their local stiffness in 1.0T1C hydrogels as compared to cell-free conditions. Surprisingly, when cultured in 1.5T1C hydrogels, these cells "chose" not to stiffen their local ECM values. In fact, when considering all probed regions and both probed axes, there are no

significant differences in stiffness between the groups of control DFs in 1.5T1C hydrogels, control DFs in 1.0T1C hydrogels, and cell-free 1.5T1C hydrogels (**Figure 2.1F**).

Closer examination of the peri-cellular region of DFs shows differential stiffness with T1C concentration, if considering local anisotropies. In cell-populated T1C hydrogels, anisotropy of collagen fiber alignment is attributed to cell-induced alignment of the matrix fibers during migration, contraction, or enhanced long range stress signaling between neighboring cells [46–48]. While stiffness along the axis perpendicular to cell elongation is equivalent between T1C concentrations ($p > 0.99$), stiffness parallel to migration is larger in 1.0T1C hydrogels than in 1.5T1C hydrogels ($p << 0.01$). Overall, our findings show that DFs in 1.0T1C hydrogels respond to and considerably increase local ECM stiffness as compared to values in the cell-free condition. ECM stiffening is also much more prominent in the peri-cellular region than in the distal region ($p << 0.01$ in X direction and $p = 0.02$ in Y direction). This finding is in agreement with the previous studies showing that ECM accumulation decreases as a function of distance to the cell [49]. By contrast, the DF cells do little to change their local stiffness landscape in 1.5T1C hydrogels, in which ECM stiffness is comparable between peri-cellular and distal regions ($p = 0.74$ in X direction and $p = 0.14$ in Y direction). This differential behavior indicates DFs might intrinsically prefer certain stiffness levels or have a setpoint. While such effect of T1C concentration on peri-cellular stiffness has not been reported previously, it has been shown that contractility of human fetal lung fibroblasts, human aortic adventitial fibroblasts, bone marrow stromal cells and DFs decreases with T1C concentration [43,50–53].

MDAs, the other migratory cell line under investigation, do not behave similarly to DFs. MDAs do not appear to significantly alter local stiffness values when comparing

treatment and cell-free conditions, but stiffness did increase with T1C concentration. As compared to DFs, MDAs exhibit a smaller extent of ECM stiffening with less matrix reorganization (**Figure 2.3**), which is in agreement with past studies [54]. Studies also indicate that MDAs can employ different strategies and modes of migration to adapt to ECMs of varying stiffness, which promotes invasion mechanisms and cancer metastasis [55]. Consequently, unlike DFs which utilize pseudopodia-based migration, MDAs might favor protrusion-based amoeboidal migration in our experimental conditions. Such migration is usually observed in migratory cells exhibiting a lesser degree of cell contractility and adhesion [38,54,56]. Amoeboidal migration should thus result in a lesser degree of strain stiffening, as our results show. Further, we expected that TGF-β1 and glucose, known to increase MDA invasiveness, would invoke an increase in MDA-mediated matrix stiffness. Such stiffening was not observed, but changes in anisotropy were observed (**Figure 2.4C**). This finding is corroborated by previous work showing the invasive potential of breast cancer cells was more correlated with the directionality of the cell contractility than magnitude of cell traction forces [57]. Of note, a finite element analysis of principal matrix stiffness around MDAs in 1.2T1C hydrogels predicts a decrease in κ close to cells [44], as we observed. However, another study used AMR with larger microbeads (4.5 μm) and found MDAs establish long range stiffening in 1.5T1C hydrogels [58], which is in disagreement with both the FEM model and our own results, yet might be observed in mesenchymal (as opposed to amoeboidal) MDAs [54]. In support of our findings, confocal reflection images of MDAs (**Figure 2.3**) demonstrate that MDAs do not significantly contract their local ECM and, as a result, the values of κ are lower than around DFs, which visibly stiffen and contract their surrounding ECM (**Figure 2.2**).

Here, we also test three different treatments which were expected to alter κ levels. TGF-β1 and glucose were expected to stiffen the local ECM of both DFs and MDAs because of their effect on increasing contractility of DFs [12,28,43] and invasiveness of MDAs [13,21]. As anticipated, when analyzing all probed beads, treatment with glucose does lead to an overall stiffer ECM near DFs. Interestingly, glucose treatment also promotes isotropic stiffening at both concentrations, with no preference to the axis of migration. In contrast, treatment with TGF-β1 did not result in prominent stiffening, which is in agreement with past studies that found limited effect of TGF-β1 on contractility of fibroblasts 24 h after treatment [59] or when cells were seeded at low density [43]. However, TGF-β1 did alter the extent of stiffness anisotropy around DFs (**Figure 2.4B**). In 1.0T1C hydrogels, control DFs establish local anisotropy and larger stiffness in the direction of migration, but this trend reverses with TGF-β1 treatment. The opposite relationship is observed for 1.5T1C hydrogels. Our results may be explained in part by findings that TGF-β1 promotes actin reorganization and stress fiber formation [60], which might manifest as a change in stiffness anisotropy due to strain stiffening. Furthermore, our finding that overall stiffness was not increased with TGF-β1 treatment may not hold over longer culture times as supported by studies showing that effects of TGF-β1 on contractility continue to increase beyond our 24 h time point [43,59].

Surprisingly, unlike DFs, the addition of either glucose or TGF-β1 to MDAs does not affect overall stiffness values, but does alter anisotropy (**Figure 2.1G**). For control cells, ECM stiffness is higher along the axis of migration in 1.0T1C hydrogels but in 1.5T1C hydrogels, anisotropy patterns are switched so that ECM is up to 2.2 times stiffer orthogonal to cell migration. By contrast, TGF-β1 treatment results in higher stiffness along the axis of migration at both T1C concentrations. This effect of TGF-β1 on stiffness anisotropy can be

corroborated by past studies which attributed higher motility, deformability and a more amoeboidal phenotype of MDAs to TGF-β1 treatment [38,61]. In the case of glucose treatment, this anisotropy favoring the direction of cell migration became more pronounced with T1C concentration even though overall stiffness did not significantly change as compared to cell-free conditions. This lack of overall stiffening is consistent with studies showing that the degree of glycolysis within MDAs did not change significantly as glucose in the media increased from 25 to 50 mM glucose [62], or when T1C concentration increased from 1.2 to 3.0 mg/ml [9]. Our culture conditions overlap those of these studies, and collectively our findings suggest that to better elucidate the effect of glucose on peri-cellular stiffness, a wider range of glucose and T1C concentrations altering cell metabolic activity should be investigated. Nonetheless, while neither treatment significantly alters overall stiffness (**Figure 2.1G**), accounting for spatial information of probed beads and axis of measurements elucidates more complex treatment effects (**Figure 2.4C**).

Lastly, the addition of Y27632 was expected to lower κ levels, as previously reported by our group [10]. Y27632-induced reduction in cell contractility was previously described for both DFs and MDAs [29,63]. Here, we find that Y27632 treatment significantly lowers overall κ around DFs as compared to control cells at both tested T1C concentrations. However, ECM stiffening as compared to cell-free conditions can still be observed in the peri-cellular region, which is in agreement with past studies [10,49] and may be indicative of ECM remodeling. Previous studies have shown that Y27632 does not fully prevent local strain stiffening around highly contractile DFs, which can still deposit T1C and crosslink existing ECM to an extent comparable with control cells in the peri-cellular region [49]. Studies on rat embryo fibroblasts in T1C hydrogels have also shown only 52% reduction in cell contractility 27 h

after adding Y27632 (10 μM) [64]. While treatment of MDAs with Y27632 was shown to reduce ROCK activity by ~ 50% [29], in our study, treatment effects on MDAs were mild with respect to stiffness. Stiffness was comparable to, or even lower than, that of cell-free conditions, suggesting that MDAs are still capable of proteolysis induced by matrix metalloproteinases activity [10]. The relative insensitivity of MDAs to Y27632 can be explained in part by the observation that these cells did not stiffen their ECM as compared to cell-free conditions. In other words, there may not be very much strain stiffening to alleviate.

In summary, AMR measurements reveal highly heterogeneous patterns of ECM stiffness around individual cells. Heterogeneities in local ECM properties have been widely reported and are also observed in cell-free hydrogels. Heterogeneities in stiffness to some extent can be indicative of differences in local fiber mesh architecture as well as properties of the collagen fibers. However, given that all cells were cultured in similar T1C hydrogels polymerized at either 1.0 or 1.5 mg/ml, we can assume that differences in local stiffness and isotropy are primarily attributed to cell-induced changes. Cells were previously shown to dynamically alter local ECM density by incessant interplay of ECM compaction and crosslink unbinding [65]. While we are unable to identify whether probed beads are attached to fibers undergoing compaction or crosslink unbinding, optical tweezers AMR is sensitive to changes in stiffness of the local mesh ensemble of these fibers. Compared to other techniques for quantifying cell-induced changes in ECM properties, AMR is not as invasive as atomic force microscopy or as destructive as laser ablation [66]. One limitation to our microrheology method is the technical inability to align the axes of bead oscillation with the cell, and reliance on projecting the *X* and *Y* axes. Future experiments will aim to align these axes and eliminate the potential errors associated with such projection. Nonetheless, we found κ levels around

both cell lines to be dependent on tested treatment and axis of measurement, yet to different extents, with MDAs establishing overall lower κ than DFs. Our results not only illustrate how cells can both adapt and modify their local ECM in response to different factors, but also highlight shortcomings of bulk stiffness measurements. Bulk rheology obscures microscopic understanding of treatment effects, which show notable heterogeneity by microrheology. Notably, despite an increase in bulk (cell-free) stiffness with increase in T1C concentration, the peri-cellular stiffness around DFs was actually found to be comparable between T1C concentrations, and in some instances, stiffness decreased with T1C concentration. Additional studies are required to further investigate this relationship between initial and final ECM stiffness and to investigate if particular cell types remodel their ECM to achieve a stiffness setpoint.

2.6. Acknowledgments

Funding was generously provided by the NSF-Simons Center for Multiscale Cell Fate Research (NSF 1763272) and the University of California Multicampus Research Programs and Initiatives Award (MRI-17-454791).

2.7. Supplementary material

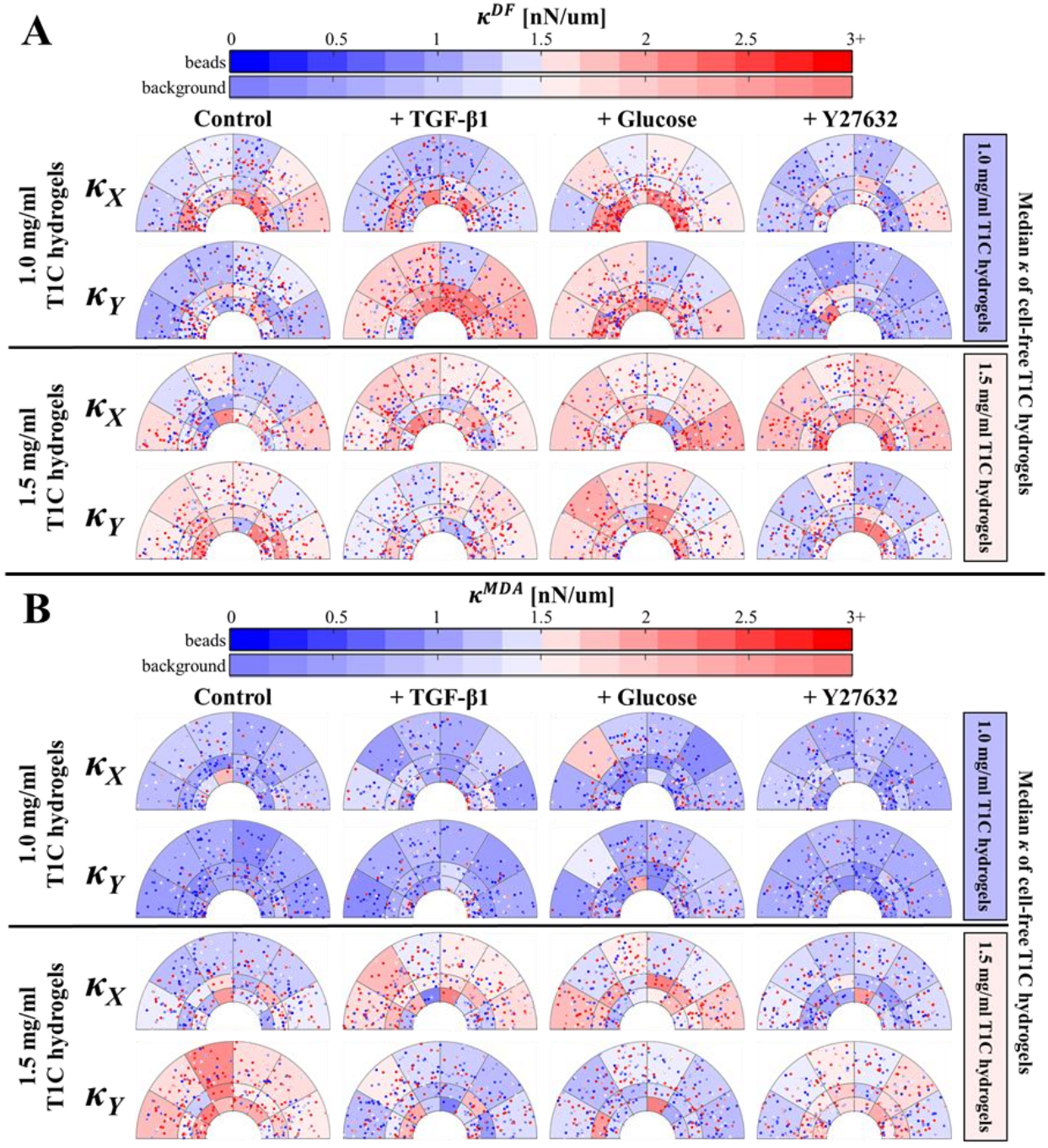

Suppl. Figure 2.1. Stiffness measurements around DFs (A) and MDAs (B) at 20 Hz.

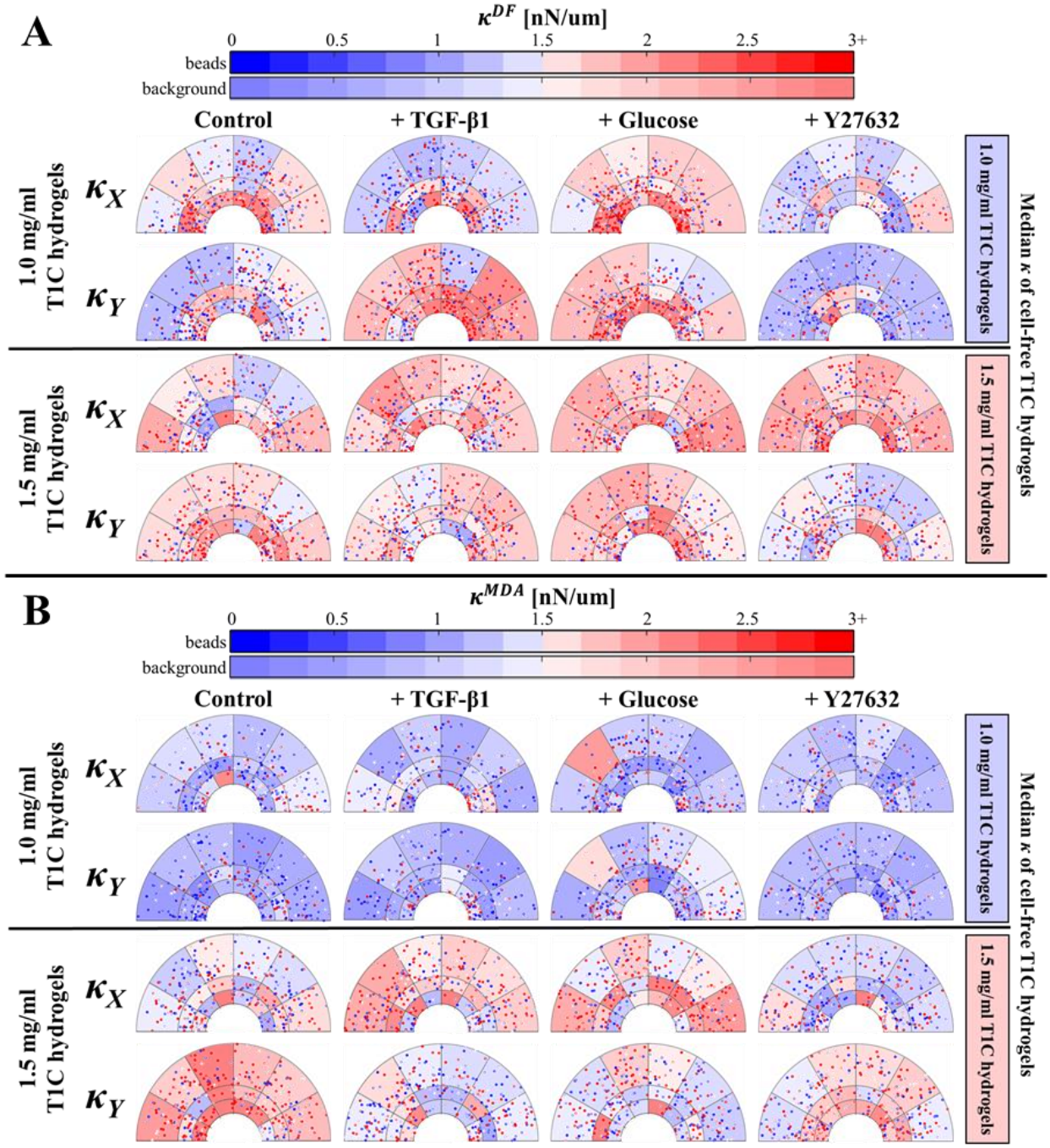

Suppl. Figure 2.2. Stiffness measurements around DFs (A) and MDAs (B) at 100 Hz.

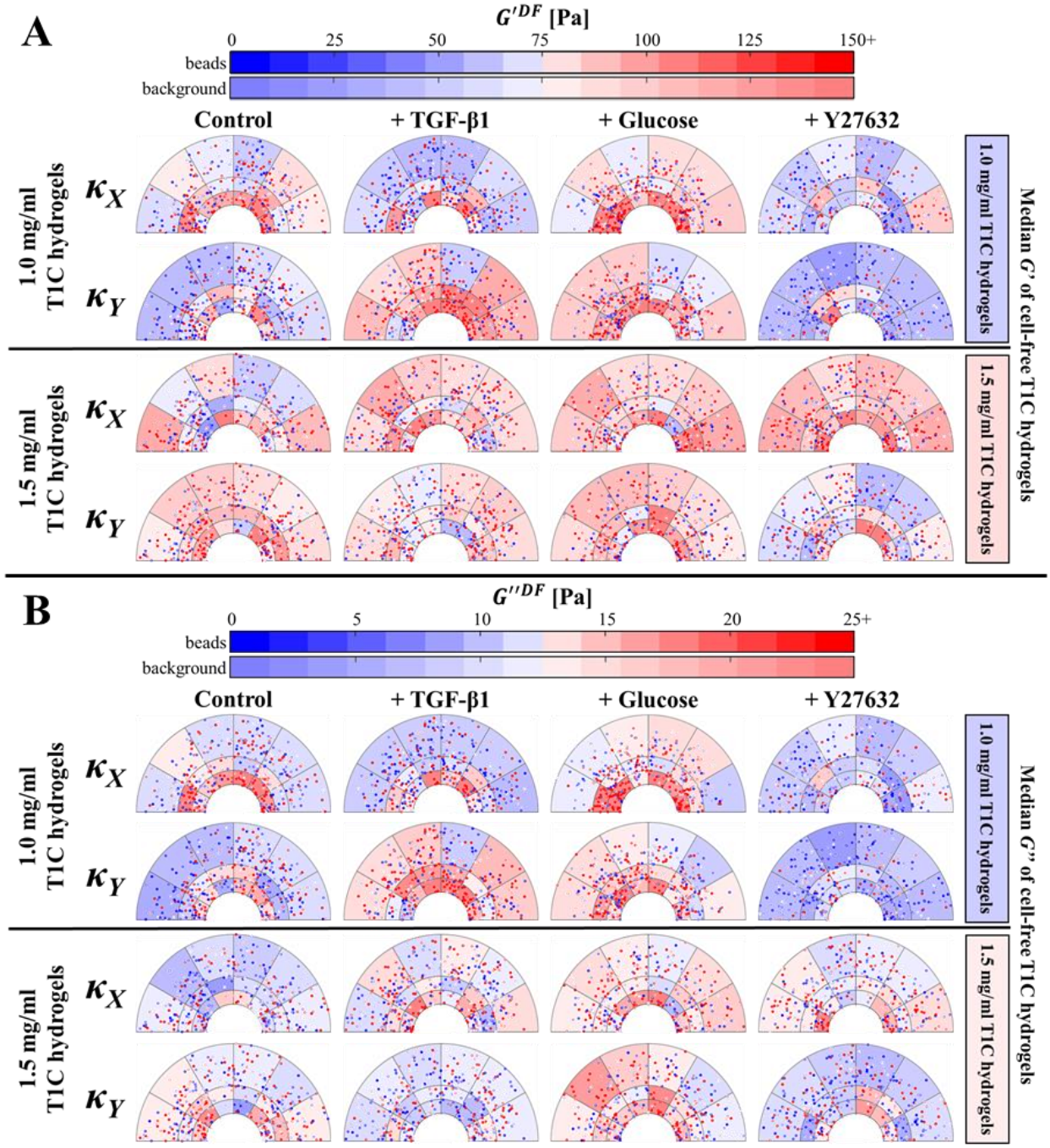

Suppl. Figure 2.3. G' (A) and G'' (B) measurements around DFs.

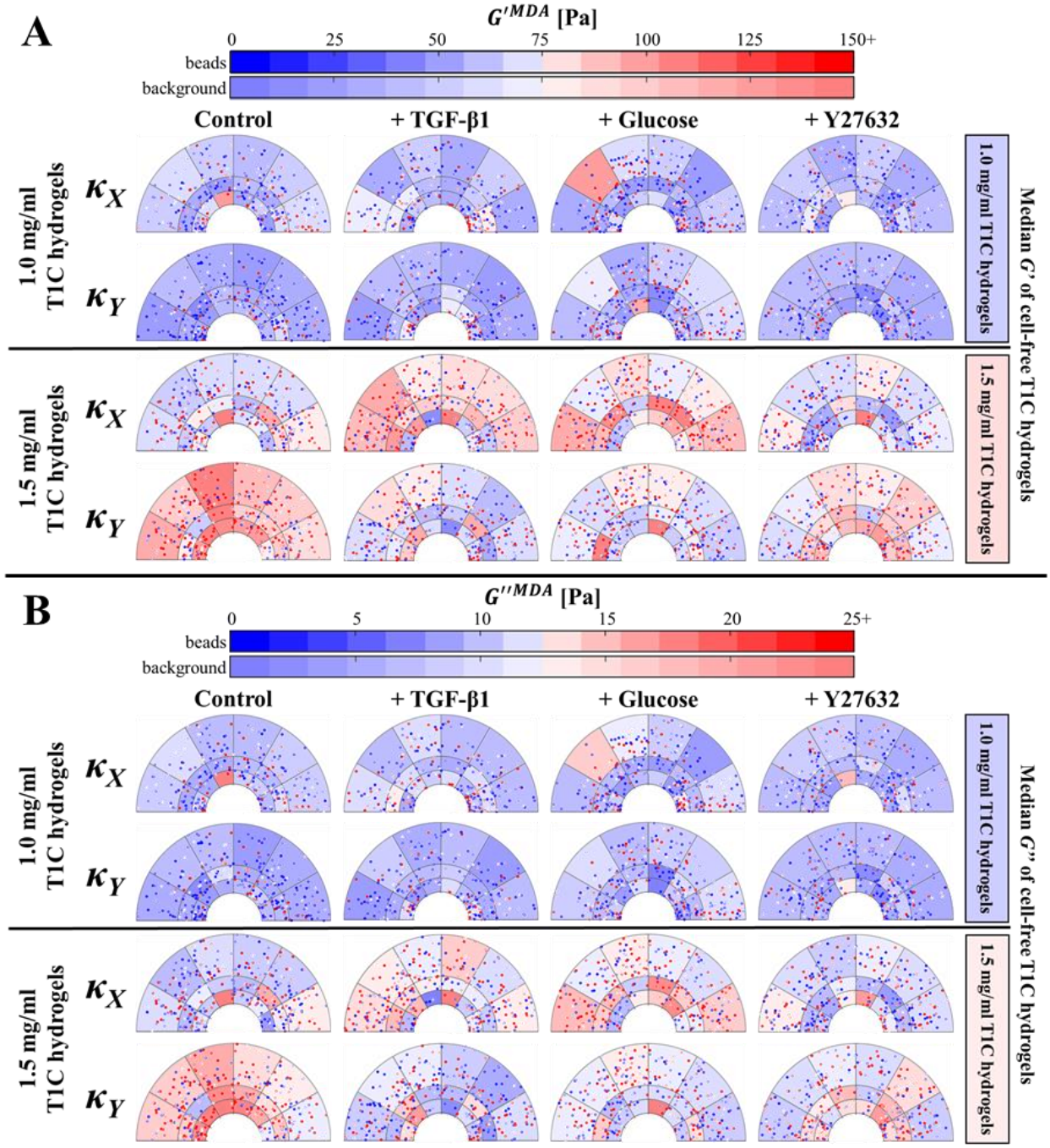

Suppl. Figure 2.4. G' (A) and G'' (B) measurements around MDAs.

Suppl. Table 2.1. Supplementary table to Figure 2.1E-2.1G.

	T1C concentration	κ values (median + std, nN/µm)			
		Control	+TGF-β1	+Glucose	+Y27632
Cell-free hydrogels	1.0 mg/ml	0.96 ± 1.08	0.93 ± 1.45	0.91 ± 1.44	0.91 ± 1.11
	1.5 mg/ml	1.77 ± 1.94	1.68 ± 1.78	1.54 ± 1.62	1.74 ± 1.74
Hydrogels with DFs	1.0 mg/ml	1.44 ± 2.99	1.59 ± 4.20	1.98 ± 3.22	0.96 ± 1.45
	1.5 mg/ml	1.68 ± 1.95	1.72 ± 2.03	1.93 ± 3.86	1.68 ± 2.29
Hydrogels with MDAs	1.0 mg/ml	0.75 ± 1.56	0.84 ± 2.07	0.88 ± 1.97	0.76 ± 1.11
	1.5 mg/ml	1.66 ± 2.21	1.46 ± 2.17	1.57 ± 2.43	1.44 ± 1.91

Suppl. Table 2.2. Supplementary table to Figure 2.1E-2.1G; *p*-statistics using Tukey-Kramer test.

		Cell-free 1.0 mg/ml				Cell-free 1.5 mg/ml				DF 1.0 mg/ml				DF 1.5 mg/ml				MDA 1.0 mg/ml				MDA 1.5 mg/ml			
		C	T	G	Y	C	T	G	Y	C	T	G	Y	C	T	G	Y	C	T	G	Y	C	T	G	Y
Cell-free 1.0 mg/ml	C		>0.99	>0.99	>0.99	<<0.01	<<0.01	<<0.01	<<0.01	<<0.01	<<0.01	<<0.01	>0.99	<<0.01	<<0.01	<<0.01	<<0.01	0.52	>0.99	>0.99	0.58	<<0.01	<<0.01	<<0.01	<<0.01
	T			>0.99	>0.99	<<0.01	<<0.01	<<0.01	<<0.01	<<0.01	<<0.01	<<0.01	>0.99	<<0.01	<<0.01	<<0.01	<<0.01	0.66	>0.99	>0.99	0.72	<<0.01	<<0.01	<<0.01	<<0.01
	G				>0.99	<<0.01	<<0.01	<<0.01	<<0.01	<<0.01	<<0.01	<<0.01	>0.99	<<0.01	<<0.01	<<0.01	<<0.01	0.97	>0.99	>0.99	0.98	<<0.01	<<0.01	<<0.01	<<0.01
	Y					<<0.01	<<0.01	<<0.01	<<0.01	<<0.01	<<0.01	<<0.01	>0.99	<<0.01	<<0.01	<<0.01	<<0.01	0.27	>0.99	>0.99	0.33	<<0.01	<<0.01	<<0.01	<<0.01
Cell-free 1.5 mg/ml	C						>0.99	>0.99	>0.99	0.15	>0.99	>0.99	<<0.01	>0.99	>0.99	>0.99	>0.99	<<0.01	<<0.01	<<0.01	<<0.01	>0.99	0.25	0.94	0.03
	T							>0.99	>0.99	0.47	>0.99	0.93	<<0.01	>0.99	>0.99	>0.99	>0.99	<<0.01	<<0.01	<<0.01	<<0.01	>0.99	0.63	>0.99	0.16
	G								>0.99	0.89	>0.99	0.53	<<0.01	>0.99	>0.99	0.93	>0.99	<<0.01	<<0.01	<<0.01	<<0.01	>0.99	0.95	>0.99	0.55
	Y									<<0.01	0.76	>0.99	<<0.01	0.88	0.98	>0.99	0.90	<<0.01	<<0.01	<<0.01	<<0.01	0.94	0.02	0.39	<<0.01
DF 1.0 mg/ml	C										0.65	<<0.01	<<0.01	0.44	0.10	<<0.01	0.45	<<0.01	<<0.01	<<0.01	<<0.01	0.45	>0.99	0.99	>0.99
	T											<<0.01	<<0.01	>0.99	>0.99	0.08	>0.99	<<0.01	<<0.01	<<0.01	<<0.01	>0.99	0.86	>0.99	0.19
	G												<<0.01	<<0.01	0.04	>0.99	<<0.01	<<0.01	<<0.01	<<0.01	<<0.01	0.02	<<0.01	<<0.01	<<0.01
	Y													<<0.01	<<0.01	<<0.01	<<0.01	0.02	>0.99	>0.99	0.04	<<0.01	<<0.01	<<0.01	<<0.01
DF 1.5 mg/ml	C														>0.99	0.18	>0.99	<<0.01	<<0.01	<<0.01	<<0.01	>0.99	0.69	>0.99	0.09
	T															0.51	>0.99	<<0.01	<<0.01	<<0.01	<<0.01	>0.99	0.25	>0.99	0.01
	G																0.22	<<0.01	<<0.01	<<0.01	<<0.01	0.34	<<0.01	0.01	<<0.01
	Y																	<<0.01	<<0.01	<<0.01	<<0.01	>0.99	0.70	>0.99	0.10
MDA 1.0 mg/ml	C																		0.86	0.21	>0.99	<<0.01	<<0.01	<<0.01	<<0.01
	T																			>0.99	0.90	<<0.01	<<0.01	<<0.01	<<0.01
	G																				0.29	<<0.01	<<0.01	<<0.01	<<0.01
	Y																					<<0.01	<<0.01	<<0.01	<<0.01
MDA 1.5 mg/ml	C																						0.68	>0.99	0.10
	T																							>0.99	>0.99
	G																								0.81
	Y																								

Suppl. Table 2.3. Supplementary table to Figure 2.1D.

	T1C concentration	Axis of measurement	κ values (median + std, nN/μm)			
			Control	+TGF-β1	+Glucose	+Y27632
Cell-free hydrogels	1.0 mg/ml	*X'*	0.98 ± 0.97	0.98 ± 1.60	0.89 ± 0.89	0.90 ± 1.11
		Y'	0.95 ± 1.18	0.85 ± 1.29	0.92 ± 1.84	0.93 ± 1.11
	1.5 mg/ml	*X'*	1.64 ± 1.75	1.80 ± 1.61	1.44 ± 1.62	1.67 ± 1.64
		Y'	1.88 ± 2.12	1.66 ± 1.95	1.58 ± 1.62	1.86 ± 1.84
Hydrogels with DFs	1.0 mg/ml	*X*	1.57 ± 3.12	1.22 ± 3.94	2.10 ± 3.21	1.06 ± 1.47
		Y	1.34 ± 2.85	2.17 ± 4.41	1.86 ± 3.23	0.85 ± 1.43
	1.5 mg/ml	*X*	1.43 ± 1.63	1.81 ± 2.13	1.93 ± 4.48	2.12 ± 2.27
		Y	1.81 ± 2.20	1.65 ± 1.90	1.93 ± 3.10	1.31 ± 2.26
Hydrogels with MDAs	1.0 mg/ml	*X*	0.94 ± 1.80	0.94 ± 2.17	0.86 ± 2.15	0.84 ± 1.04
		Y	0.63 ± 1.27	0.74 ± 1.97	0.93 ± 1.78	0.69 ± 1.19
	1.5 mg/ml	*X*	1.22 ± 1.74	1.77 ± 2.25	1.79 ± 2.40	1.19 ± 1.99
		Y	2.05 ± 2.52	1.19 ± 2.08	1.27 ± 2.44	1.71 ± 1.82

Suppl. Table 2.4. Supplementary table to Figure 2.4; *p*-statistics using Tukey-Kramer test.

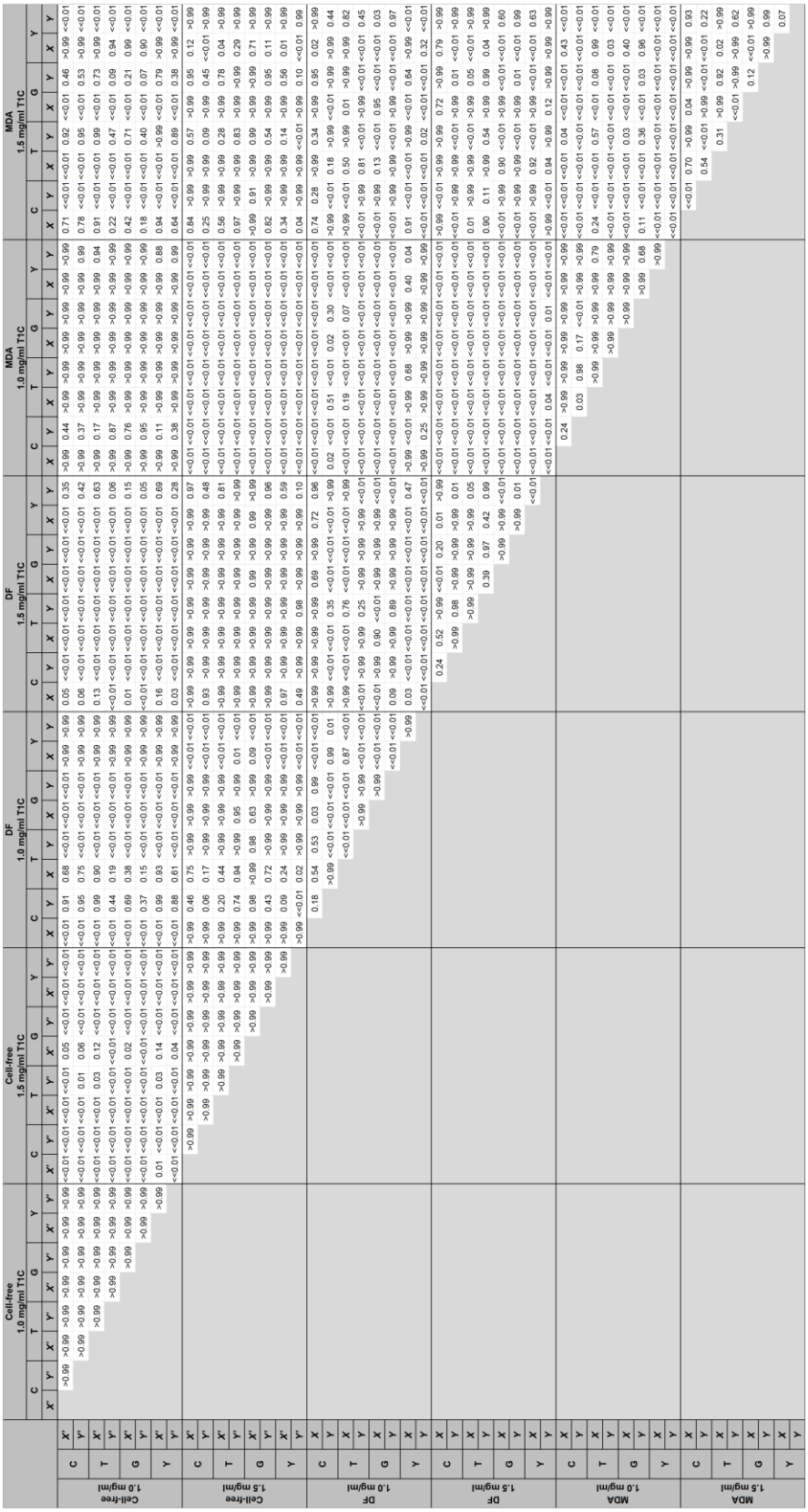

Suppl. Table 2.5. Supplementary table to Figure 2.4; *p*-statistics using Tukey-Kramer test on stiffness measurements collected in the peri-cellular region.

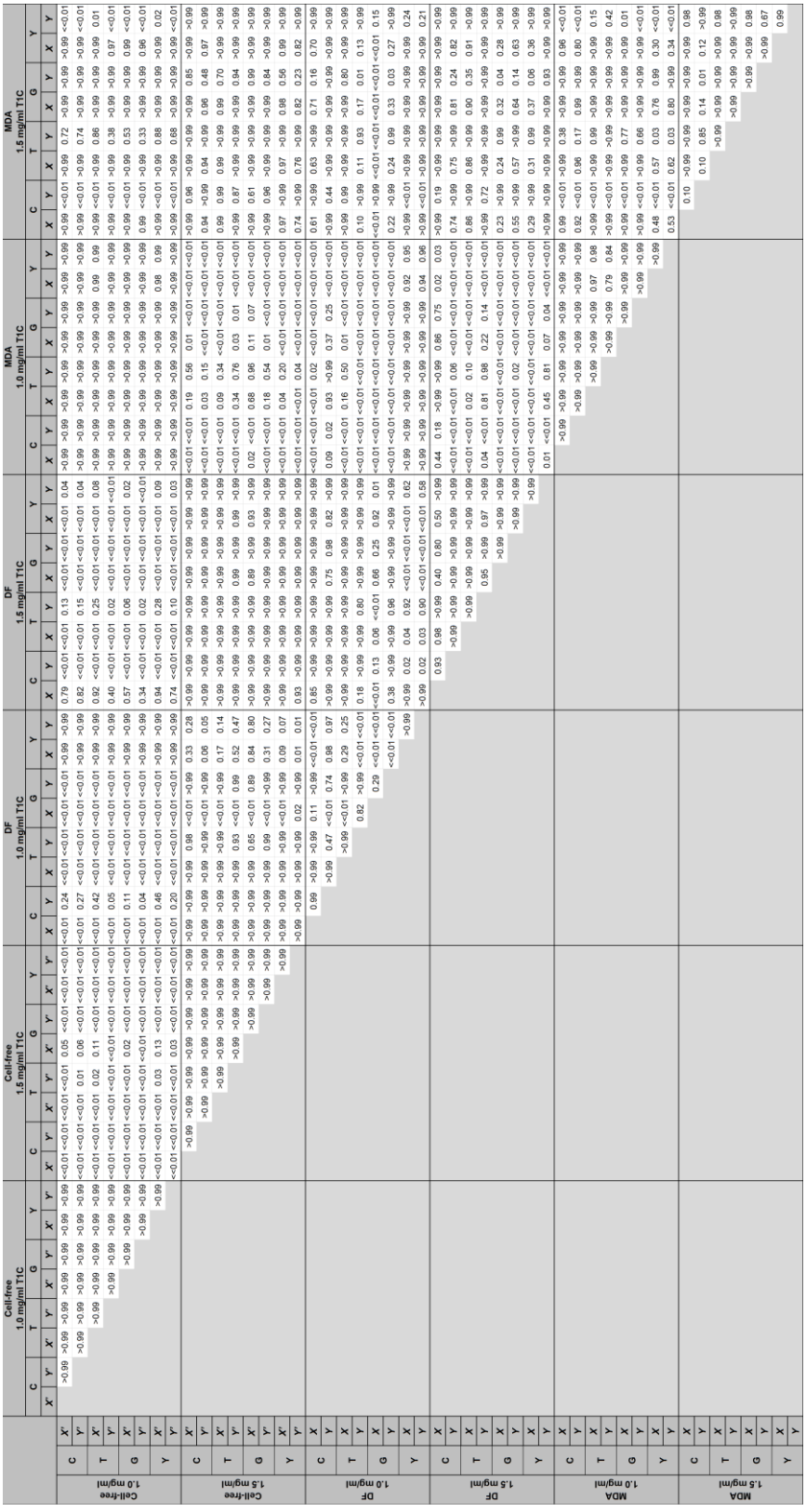

Suppl. Table 2.6. Supplementary table to Figure 2.4; *p*-statistics using Tukey-Kramer test on stiffness measurements collected in the distal region.

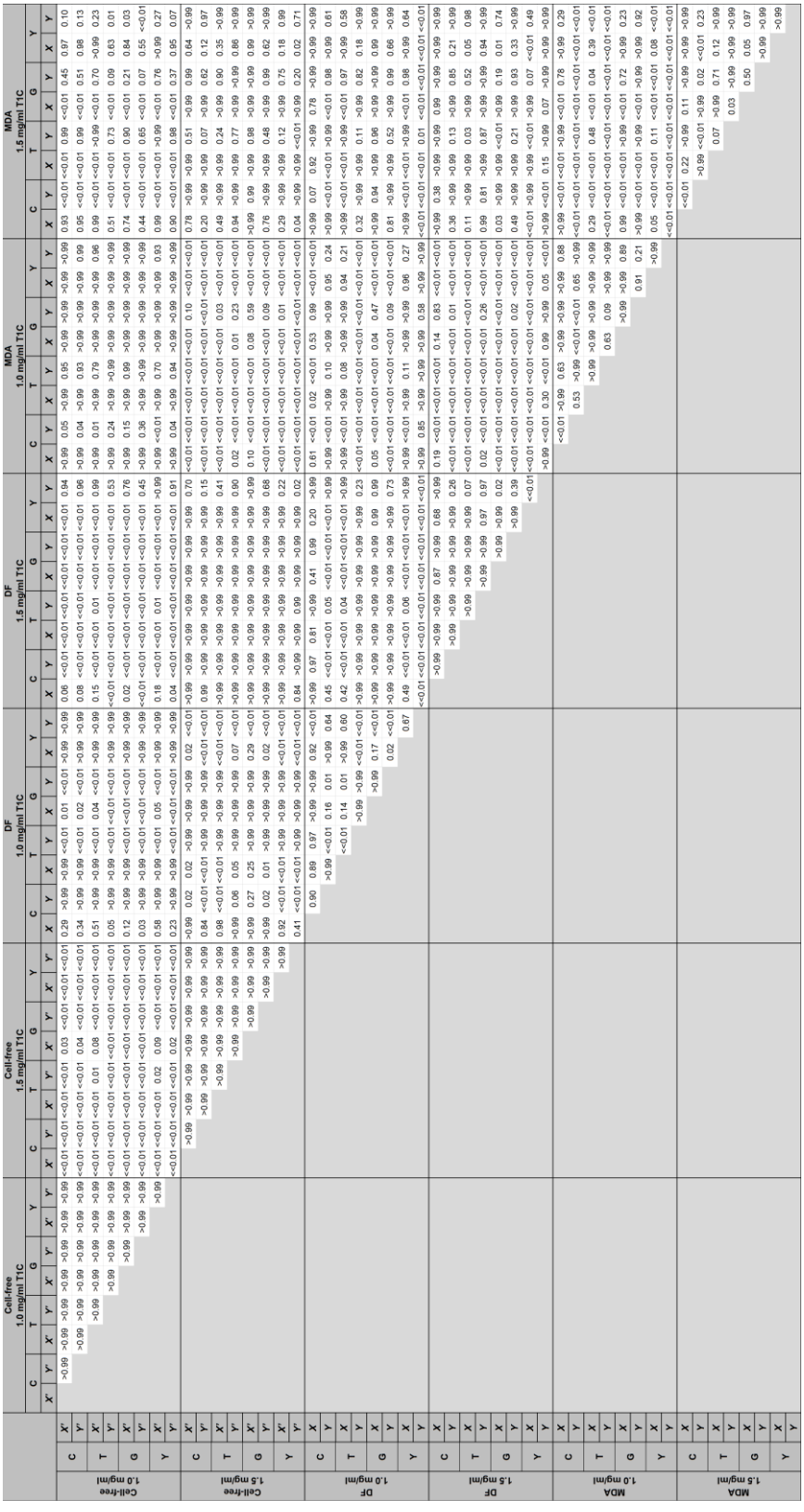

2.8. References

1. Kumar, S. & Weaver, V. M. Mechanics, malignancy, and metastasis: The force journey of a tumor cell. *Cancer Metastasis Rev.* **28**, 113–127 (2009).

2. Gkretsi, V. & Stylianopoulos, T. Cell Adhesion and Matrix Stiffness : Coordinating Cancer Cell invasion and Metastasis. *Front. Oncol.* **8**, 1–7 (2018).

3. Li, Z. *et al.* Cellular traction forces: a useful parameter in cancer research. *Nanoscale* **9**, 19039–19044 (2017).

4. Varghese, S., Samuel, S. M., Varghese, E., Kubatka, P. & Büsselberg, D. High Glucose Represses the Anti-Proliferative and Pro-Apoptotic Effect of Metformin in Triple Negative Breast Cancer Cells. *Biomolecules* **9**, (2019).

5. Wu, P. *et al.* A comparison of methods to assess cell mechanical properties. *Nat. Methods* **15**, 491–498 (2018).

6. Vader, D., Kabla, A., Weitz, D. & Mahadevan, L. Strain-induced alignment in collagen gels. *PLoS One* **4**, (2009).

7. Ferreira, S. A. *et al.* Bi-directional cell-pericellular matrix interactions direct stem cell fate. *Nat. Commun.* **9**, 4049 (2018).

8. Kalli, M. & Stylianopoulos, T. Defining the Role of Solid Stress and Matrix Stiffness in Cancer Cell Proliferation and Metastasis. *Front. Oncol.* **8**, 1-7 (2018).

9. Mah, E. J., Lefebvre, A. E. Y. T., Mcgahey, G. E., Yee, A. F. & Digman, M. A. Collagen density modulates triple-negative breast cancer cell metabolism through adhesion- mediated contractility. *Sci. Rep.* **8**, 1–11 (2018).

10. Keating, M., Kurup, A., Alvarez-Elizondo, M., Levine, A. J. & Botvinick, E. Spatial distributions of pericellular stiffness in natural extracellular matrices are dependent on cell-mediated proteolysis and contractility. *Acta Biomater.* **57**, 304–312 (2017).

11. Tracy, L. E., Minasian, R. A. & Caterson, E. J. Extracellular Matrix and Dermal Fibroblast Function in the Healing Wound. *Adv. Wound Care* **5**, 119–136 (2016).

12. Humphrey, J. D., Dufresne, E. R. & Schwartz, M. A. Mechanotransduction and extracellular matrix homeostasis. *Nat. Rev. Mol. Cell Biol.* **15**, 802–812 (2014).

13. Najafi, M. Extracellular matrix (ECM) stiffness and degradation as cancer drivers. *J Cell Biochem.* **120**, 2782–2790 (2019).

14. Daley, W. P., Peters, S. B. & Larsen, M. Extracellular matrix dynamics in development and regenerative medicine. *J. Cell Sci.* **121**, 255–264 (2008).

15. Lu, P., Takai, K., Weaver, V. M. & Werb, Z. Extracellular Matrix Degradation and Remodeling in Development and Disease. *Cold Spring Harb Perspect Biol* **3**, 1–24 (2011).

16. Ansardamavandi, A., Tafazzoli-shadpour, M., Ali, M. & Group, F. Behavioral remodeling of normal and cancerous epithelial cell lines with differing invasion potential induced by substrate elastic modulus. *Cell Adh. Migr.* **12**, 472–488 (2018).

17. Mandel, K. *et al.* Characterization of Spontaneous and TGF- b -Induced Cell Motility of Primary

Human Normal and Neoplastic Mammary Cells In Vitro Using Novel Real-Time Technology. **8**, 1-10 (2013).

18. Liu, F., Gu, L.-N., Shan, B.-E., Geng, C.-Z. & Sang, M.-X. Biomarkers for EMT and MET in breast cancer : An update (Review). *Oncol. Lett.* **12**, 4869–4876 (2016).

19. Pille, J.-Y. *et al.* Anti-RhoA and Anti-RhoC siRNAs Inhibit the Proliferation and Invasiveness of MDA-MB-231 Breast Cancer Cells in Vitro and in Vivo. **11**, 267–274 (2005).

20. Tavares, S. *et al.* Actin stress fiber organization promotes cell stiffening and proliferation of pre-invasive breast cancer cells. *Nat. Commun.* **8**, 1-18 (2017).

21. Lin, F., Zhang, H., Huang, J. & Xiong, C. Substrate Stiffness Coupling TGF-β1 Modulates Migration and Traction Force of MDA-MB-231 Human Breast Cancer Cells in Vitro. *ACS Biomater. Sci. Eng.* **4**, 1337–1345 (2018).

22. Liberti, M. V, Locasale, J. W., Biology, C. & Biology, C. The Warburg Effect: How Does it Benefit Cancer Cells? *Trends Biochem Sci.* **41**, 211–218 (2016).

23. Gupta, C. & Tikoo, K. High glucose and insulin differentially modulates proliferation in MCF-7 and MDA-MB-231 cells. *J. Mol. Endocrinol.* **51**, 119–129 (2012).

24. Wahdan-Alaswad, R. *et al.* Glucose promotes breast cancer aggression and reduces metformin efficacy. *Cell Cycle* **12**, 3759–3769 (2013).

25. Buranasin, P. *et al.* High glucose-induced oxidative stress impairs proliferation and migration of human gingival fibroblasts. *PLoS One* **13**, 1–19 (2018).

26. Sibbit, W. L. *et al.* Glucose Inhibition of Human Fibroblast Proliferation and Response to Growth Factors is Prevented by Inhibitors of Aldose Reductase. *Mech. Ageing Dev.* **47**, 265–279 (1989).

27. Lamers, M. L., Almeida, M. E. S., Vicente-Manzanares, M., Horwitz, A. F. & Santos, M. F. High glucose-mediated oxidative stress impairs cell migration. *PLoS One* **6**, 1–9 (2011).

28. Zhang, X., Jr, J. A. S. & Kane, I. D. Effects of elevated glucose levels on interactions of cardiac fibroblasts with the extracellular matrix. *Vitr. Cell.Dev.Biol. - Anim.* **43**, 297–305 (2007).

29. Liu, S., Goldstein, R. H., Scepansky, E. M. & Rosenblatt, M. Inhibition of Rho-Associated Kinase Signaling Prevents Breast Cancer Metastasis to Human Bone. *Cancer Res* **69**, 8742–8752 (2009).

30. Nakagawa, O. *et al.* ROCK-I and ROCK-II, two isoforms of Rho-associated coiled-coil forming protein serine/threonine kinase in mice. *FEBS Lett.* **392**, 189–193 (1996).

31. Lane, J., Martin, T. A., Watkins, G., Mansel, R. E. & Jiang, W. E. N. G. The expression and prognostic value of ROCK I and ROCK II and their role in human breast cancer. *Int. J. Oncol.* **33**, 585–593 (2008).

32. Doyle, A. D. Generation of 3D collagen gels with controlled, diverse architectures. *Curr Protoc Cell Biol.* **72**, 1–22 (2016).

33. Kestin, J., Sokolov, M. & Wakeham, W. A. Viscosity of liquid water in the range -8°C to 150°C. *J. Phys. Chem. Ref. Data* **7**, 941–948 (1978).

34. Mizuno, D., Head, D. A., MacKintosh, F. C. & Schmidt, C. F. Active and passive microrheology in equilibrium and nonequilibrium systems. *Macromolecules* **41**, 7194–7202 (2008).

35. Shayegan, M. & Forde, N. R. Microrheological Characterization of Collagen Systems : From Molecular Solutions to Fibrillar Gels. *PLoS One* **8**, 23–28 (2013).

36. Nijenhuis, N., Mizuno, D., Spaan, J. A. E. & Schmidt, C. F. High-resolution microrheology in the pericellular matrix of prostate cancer cells. *J. R. Soc. Interface* **9**, 1733–1744 (2012).

37. Han, D. C., Isono, M., Hoffman, B. B. & Ziyadeh, F. N. High glucose stimulates proliferation and collagen type I synthesis in renal cortical fibroblasts: Mediation by autocrine activation of TGF-β. *J. Am. Soc. Nephrol.* **10**, 1891–1899 (1999).

38. Geiger, F., Rüdiger, D., Zahler, S. & Engelke, H. Fiber stiffness, pore size and adhesion control migratory phenotype of MDA-MB-231 cells in collagen gels. *PLoS One* **14**, 1–13 (2019).

39. Wessels, D. J. *et al.* Reciprocal signaling and direct physical interactions between fibroblasts and breast cancer cells in a 3D environment. *PLoS One* **14**, 1–27 (2019).

40. Yakut Ali, M., Chuang, C.-Y. & Saif, M. T. A. Reprogramming Cellular Phenotype by Soft Collagen Gels. *Soft Matter* **10**, 8829–8837 (2014).

41. Licup, J. A. *et al.* Stress controls the mechanics of collagen networks. *PNAS* **112**, 9573–9578 (2015).

42. Shariatzadeh, M., Cm, P. & Lacroix, D. Stiffness of Cell Micro-Environment Guides Long Term Cell Growth in Cell Seeded Collagen Microspheres. *Arch Clin Biomed Res* **2**, 167–182 (2018).

43. Liu, X. D. & Rennard, S. I. Persistence of TGF-β1 induction of increased fibroblast contractility. *Vitr. Cell.Dev.Biol. - Anim.* **37**, 193–201 (2001).

44. Steinwachs, J. *et al.* Three-dimensional force microscopy of cells in biopolymer networks. *Nat. Methods* **13**, 171–176 (2016).

45. Baker, E. L., Bonnecaze, R. T. & Zaman, M. H. Extracellular matrix stiffness and architecture govern intracellular rheology in cancer. *Biophys. J.* **97**, 1013–1021 (2009).

46. Thomopoulos, S., Fomovsky, G. M., Chandran, P. L. & Holmes, J. W. Anisotropy in Fibroblast Populated Collagen Gels. *J Biomech Eng* **129**, 642–650 (2007).

47. Thomopoulos, S., Costa, K. D. & Holmes, J. W. The Development of Structural and Mechanical Anisotropy in Fibroblast Populated Collagen Gels. *J Biomech Eng* **127**, 742–750 (2005).

48. Velegol, D. & Lanni, F. Cell Traction Forces on Soft Biomaterials. I. Microrheology of Type I Collagen Gels. *Biophys. J.* **81**, 1786–1792 (2001).

49. Shakiba, D. *et al.* The Balance between Actomyosin Contractility and Microtubule Polymerization Regulates Hierarchical Protrusions That Govern Efficient Fibroblast–Collagen Interactions. *ACS Nano* **14**, 7868–7879 (2020).

50. Jin, T., Li, L., Siow, R. C. M. & Liu, K. K. Collagen matrix stiffness influences fibroblast contraction force. *Biomed. Phys. Eng. Express* **2**, 1-5 (2016).

51. Zhu, Y. K. *et al.* Contraction of fibroblast-containing collagen gels: Initial collagen concentration regulates the degree of contraction and cell survival. *Vitr. Cell. Dev. Biol. - Anim.* **37**, 10–16 (2001).

52. Chieh, H. F. *et al.* Effects of cell concentration and collagen concentration on contraction kinetics and mechanical properties in a bone marrow stromal cell-collagen construct. *J. Biomed. Mater. Res. - Part A* **93**, 1132–1139 (2010).

53. Freyman, T. M., Yannas, I. V., Yokoo, R. & Gibson, L. J. Fibroblast contractile force is independent of the stiffness which resists the contraction. *Exp. Cell Res.* **272**, 153–162 (2002).

54. Hall, M. S. *et al.* Fibrous nonlinear elasticity enables positive mechanical feedback between cells and ECMs. *Proc. Natl. Acad. Sci. U. S. A.* **113**, 14043–14048 (2016).

55. Sun, W., Lim, C. T. & Kurniawan, N. A. Mechanistic adaptability of cancer cells strongly affects anti-migratory drug efficacy. *J. R. Soc. Interface* **11**, 1-11 (2014).

56. Paul, C. D. *et al.* Cancer cell motility : lessons from migration in confined spaces. *Nat Rev Cancer* **17**, 131–140 (2017).

57. Bonakdar, N., Butler, J. P., Fabry, B., Koch, T. M. & Mu, S. 3D Traction Forces in Cancer Cell Invasion. *PLoS One* **7**, 1-8 (2012).

58. Han, Y. L. *et al.* Cell contraction induces long-ranged stress stiffening in the extracellular matrix. *Proc. Natl. Acad. Sci. U. S. A.* **115**, 4075–4080 (2018).

59. Tingstrom, A., Heldin, C. H. & Rubin, K. Regulation of fibroblast-mediated collagen gel contraction by platelet-derived growth factor, interleukin-1 α and transforming growth factor-β1. *J. Cell Sci.* **102**, 315–322 (1992).

60. Sandbo, N. & Dulin, N. Actin cytoskeleton in myofibroblast differentiation: Ultrastructure defining form and driving function. *Transl. Res.* **158**, 181–196 (2011).

61. Kulkarni, A. H., Chatterjee, A., Kondaiah, P. & Gundiah, N. TGF-β induces changes in breast cancer cell deformability. *Phys. Biol.* **15**, 1-13 (2018).

62. Zanotelli, M. R. *et al.* Regulation of ATP utilization during metastatic cell migration by collagen architecture. *Mol. Biol. Cell* **29**, 1–9 (2018).

63. Han, Y., Nien, Y. & Garner, W. L. Recombinant human platelet-derived growth factor and transforming growth factor-β mediated contraction of human dermal fibroblast populated lattices is inhibited by Rho/GTPase inhibitor but does not require phosphatidylinositol-3' kinase. *Wound Rep Reg* **10**, 169–176 (2002).

64. Gates, D. H., Lee, J. S., Hultman, C. S. & Cairns, B. A. Inhibition of rho-kinase impairs fibroblast stress fiber formation, confluence, and contractility in vitro. *J. Burn Care Res.* **28**, 507–513 (2007).

65. Malandrino, A., Trepat, X., Kamm, R. D. & Mak, M. Dynamic filopodial forces induce accumulation, damage, and plastic remodeling of 3D extracellular matrices. *PLoS Comput. Biol.* **15**, 1–26 (2019).

66. Malandrino, A., Mak, M., Kamm, R. D. & Moeendarbary, E. Complex mechanics of the heterogeneous extracellular matrix in cancer. *Extrem. Mech. Lett.* **21**, 25–34 (2018).

Chapter 3: Stiffness-matched extracellular matrices comprising collagen or fibrin differentially affect cell-mediated remodeling and peri-cellular stiffness

Alicja Jagiełło[1], Ulysses Castillo[1], Elliot Botvinick[1,2,3,4]

[1] Department of Biomedical Engineering, University of California Irvine, Irvine, CA, 92697-2730, United States

[2] Beckman Laser Institute and Medical Clinic, University of California Irvine, Irvine, CA, 92612, United States

[3] Department of Surgery, University of California Irvine, 333 City Boulevard, Suite 700, Orange, CA, 92868, United States

[4] The Edwards Lifesciences Foundation Cardiovascular Innovation and Research Center, University of California Irvine, Irvine, CA, 92697-2730, United States

3.1. Abstract

Cells are known to continuously remodel their local extracellular matrix (ECM) and in a reciprocal way, they can also respond to mechanical and biochemical properties of their fibrous environment. In this study, we measured how stiffness around dermal fibroblasts (DFs) and human fibrosarcoma HT1080 cells differs with concentration of rat tail type 1 collagen (T1C) and type of ECM. Peri-cellular stiffness was probed in four directions using multi-axes optical tweezers active microrheology (AMR). First, we found that neither cell type significantly altered local stiffness landscape at different concentrations of T1C. Next, rat tail T1C, bovine skin T1C and fibrin cell-free hydrogels were polymerized at concentrations formulated to match median stiffness value. Each of these hydrogels exhibited distinct fiber architecture. Stiffness landscape and fibronectin secretion, but not nuclear-cytoplasmic YAP ratio differed with ECM type. Further, cell response to Y27632 or BB94 treatments, inhibiting cell contractility and activity of matrix metalloproteinases, respectively, was also dependent on ECM type. Given differential effect of tested ECMs on peri-cellular stiffness landscape, treatment effect and cell properties, this study underscores the need for peri-cellular and not bulk stiffness measurements in studies on cellular mechanotransduction.

3.2. Introduction

Extracellular matrix (ECM) provides physical and biochemical support and controls homeostasis, function and development of majority of eukaryotic cells in the human body [1–4]. While natural ECM is mostly comprised of type I collagen (T1C), even small changes in composition or biochemical and mechanical properties of the ECM can alter cell development and behavior [2–5]. For instance, bulk stiffness of the ECM was found to regulate cell morphology, rate of migration, stem cell differentiation and cancer cell invasiveness [6–9]. In a reciprocal way, ECM is also constantly remodeled by the cells [3–5]. Past research by our group has shown that 24 hours after hydrogel polymerization, cells alter local and peri-cellular stiffness by a few orders of magnitude, even on a single cell level [10]. Further, cells can promote distinct stiffness anisotropies which vary with cell line, T1C concentration and biochemical treatments [11]. Nonetheless, more comprehensive understanding of bi-directional relationship between cell behavior and ECM stiffness is still lacking.

In this study, we assessed the effect of hydrogel concentration and ECM type on stiffness around two distinct types of cells – normal human dermal fibroblasts (DFs) and human fibrosarcoma HT1080 cells. Our laboratory uses multi-axes optical tweezers active microrheology (AMR) to measure stiffness around cells along four distinct axes. In the first set of experiments, cells were cultured inside rat tail T1C hydrogels prepared at 4 different concentrations (1.0, 1.5, 2.0 and 3.0 mg/ml). AMR measurements were conducted 48 hours after sample preparation to investigate if local stiffness levels established by the cells are influenced by the initial concentration of hydrogels or whether cells have a stiffness setpoint and remodel their local environment to promote stiffness levels they intrinsically prefer, as previously suggested by our group [11].

In the second set of experiments, cells were subjected to three different types of ECM – rat tail T1C, bovine skin T1C and fibrin. While rat tail T1C is most frequently used in *in vitro* research [12,13], bovine skin T1C is more commonly utilized in therapeutic applications, due to its minimal antigenicity [13,14]. Conversely, less durable fibrin forms temporary and provisional matrix during wound healing processes [15,16]. At much higher concentration, fibrin sealant is used as a tissue adhesive approved for laboratory and clinical use [17–19]. Hydrogel mechanics, fiber architecture and porosity are known to vary between different ECMs [12,13,16,20,21], yet studies comparing properties of hydrogels prepared at similar concentrations often fail to account for difference in stiffness sensed by the cells. Consequently, in this study, concentrations of rat tail T1C, bovine skin T1C and fibrin were chosen to ensure similar initial stiffness of hydrogels. The effect of ECM on cell behavior was further investigated by analyzing the impact of two treatments on peri-cellular stiffness and cell morphology. Rho-kinase inhibitor Y27632 is known to alter cell morphology and reduce contractility and migration of fibroblasts [22–24] and HT1080s [25–28]. Broad-spectrum zinc metalloproteinase (MMP) inhibitor batimastat (also known as BB94) was previously shown to prevent MMP secretion [29–31] and collagenolytic activity of DFs and HT1080s [31]. Past studies by our group [10] found that both Y27632 and BB94 promote decrease in stiffness around the DFs, but the effect of type of ECM on cell response to treatments has not been previously investigated.

Results reported in this study demonstrate that peri-cellular stiffness of DFs and HT1080s varies depending on type of ECM, hydrogel concentration and tested treatment. Interestingly, cell properties including nuclear/cytoplasmic YAP ratio and proportion of secreted fibronectin do not correlate with peri-cellular stiffness levels in our experiments.

Cell environment is shown to affect cellular response to treatments, underscoring the need for peri-cellular and not bulk stiffness measurements in studies on cellular mechanotransduction.

3.3. Methods

3.3.1. Cell culture

Normal human dermal fibroblasts (DFs, Lonza) were cultured in Dulbecco's Modified Eagle's Medium (DMEM) with low glucose, L-glutamate, and sodium pyruvate (ThermoFisher) and supplemented with 10% Fetal Bovine Serum (FBS, Gibco) and 1% penicillin streptomycin (Gibco). Human fibrosarcoma HT1080 cells (ATCC) were cultured in Eagle's Minimum Essential Medium (EMEM, ATCC) supplemented with 10% FBS and 1% penicillin streptomycin.

3.3.2. Collagen hydrogel preparation

Rat tail collagen hydrogels were prepared at 1.0, 1.5, 2.0 and 3.0 mg/ml concentrations using type I rat tail telocollagen (Advanced Biomatrix, #7858). Bovine skin collagen hydrogels were prepared at 1.75 mg/ml concentration using type I bovine skin telocollagen (Advanced Biomatrix, #7811). As described in **Chapter 2.3**, collagen was supplemented with 10X Phosphate-Buffered Saline (PBS, ThermoFisher), 10X DMEM (Sigma), 10X reconstitution buffer[32], 1 N NaOH (ThermoFisher), 2 μm carboxylated silica microbeads (0.8 mg/ml, Bangs Laboratories), and cells (50 k/ml). Hydrogels were polymerized inside 35 mm glass bottom dishes (MatTek) in a standard tissue culture incubator at 37 °C and 5% CO2. After 30 min, hydrogels were hydrated with 2 ml of culture media supplemented with 25 mM HEPES (Gibco). Treatment of 20 μM Y27632 (Sigma,

#0000097404) or 10 μM BB94 (Sigma, #3560212) was added to media 1 hour or 48 hours before AMR measurements, respectively.

3.3.3. Fibrin hydrogel preparation

Fibrin hydrogels were prepared at 2.7 mg/ml concentration as previously described [33,34]. Bovine stock fibrinogen (Sigma, SLCG6303) was dissolved in PBS, filtered and supplemented with 2 μm carboxylated silica microbeads and 50 k/ml of cells. 1 ml hydrogel was polymerized inside of a 35 mm glass bottom dish (MatTek), following the addition of bovine thrombin (4 U/ml, Sigma, SLBW2056). Hydrogels were incubated in a standard tissue culture incubator at 37 °C and 5% CO2 for 30 min and then hydrated with 2 ml of culture media supplemented with 25 mM HEPES (Gibco). Treatment of 20 μM Y27632 or 10 μM BB94 was added to media 1 hour or 48 hours before AMR measurements, respectively.

3.3.4. Microstructural assessment of hydrogels

Cell-free hydrogels were prepared 48 hours before imaging and stained with Atto 488 NHS ester dye (Sigma). Fluorescent images were obtained with the 488 nm laser line using Fluoview3000 laser scanning microscope equipped with a UPlanSApo 40x/1.25 NA silicone immersion objective lens (Olympus). Z-stacks of images were collected between 30 and 50 μm from the glass height using a step size of 0.25 μm, a scanning speed of 2 μs/pixel and a total scan resolution of 1024 pixels x 1024 pixels across a 96.72 μm x 96.72 μm field-of-view (FOV).

Porosity of cell-free hydrogels was assessed by Ulysses Castillo using deconvoluted and binarized images from 6 FOVs per hydrogel obtained from 3 distinct hydrogels per condition. Pore size in cell-free hydrogels was calculated as the maximum diameter of a

sphere inscribed inside each pore. Individual pores were identified using Distance Transport Watershed 3D algorithm and quantified using Analyze Regions 3D algorithm, both of which are incorporated into MorphoLibJ plug-in [35] for Fiji software [36].

3.3.5. Active and passive microrheology

Stiffness was measured using multi-axes optical tweezers active microrheology system previously described in **Chapter 1.3.1** and in **Chapter 2.3**, but optimized to allow measurements in arbitrary number of directions. Briefly, each hydrogel sample was mounted in a dish holder placed inside the stage-top nanopositioning piezoelectric stage (P-545.xR8S PInano® XYPiezoSystem,PI). Individual microbeads were oscillated by applying optical forces applied with a continuous-wave fiber laser with an emission at 1064 nm (YLR-5–1064-LP, IPG Photonics). Trapping beam oscillations with an amplitude of 60 nm and frequency of 50 Hz, unless specified otherwise, were produced by the movement of a pair of galvanometer mirrors (GVS012, ThorLabs), located conjugate to the back focal plane of the microscope objective lens (60x-oil PlanApo TIRFM 1.45NA, Olympus). A detection laser beam of wavelength 785 nm generated by a single mode fiber-pigtailed laser diode (LP785-SF100, ThorLabs) was co-aligned with the trapping beam at the center of the bead. Change in bead position and trapping beam position were recorded by two quadrant photodiodes (detQPD and trapQPD, 2901 and 2903, respectively, Newport) and used to calculate a complex material response ($\alpha^*(\omega)$) by the relationship X= $\alpha^*(\omega)F$, where X and F are the Fourier components of bead displacement and optical force, respectively. $\alpha^*(\omega)$ is computed once for each oscillation direction under the assumption that $\alpha^*(\omega)$ oscillates purely along that axis. Reported stiffness $\kappa^*(\omega)$ represents the real component of inverse α^*. Using generalized Stokes relation, $\kappa^*(\omega)$ can be used to calculate complex shear response $G^*(\omega)$,

which is represented as $G^*(\omega) = G'(\omega) + G''(\omega) = (\omega)/6\pi r$, where r is the radius of the bead (1 μm) [37,38]. The proportionality parameter relating detQPD signals to bead displacements was measured *in situ* per bead and per angle of oscillation. After centering the stage on each bead, the stage was moved 200 nm across the bead with a constant velocity of 100 nm/s. Recorded detQPD voltages were used to quantify the voltage-to-μm conversion factor [39–41], which was later used to calculate bead displacement during AMR measurements. Prior to AMR measurements in hydrogels, the AMR system was calibrated in water, as previously described [10,11,37]. 10 cells across 5 samples were analyzed per condition. At least 40 beads were probed around each cell and each probed bead was located approximately 35 μm from the cover glass and oscillated along 4 different directions. In cell-free hydrogels and around HT1080s, beads were oscillated at 0°, 45°, 90° and 135° with respect to the horizontal axis of the camera image FOV. Around DFs, beads were oscillated at 0°, 45°, 90° and 135° with respect to the long axis of the cell. All reported AMR measurements were found to be above our limit of detection [42]. In addition to AMR measurements, passive microrheology (PMR) data was collected by recording detQPD signals for 30 s with only detection laser beam positioned at the center of the bead. G' and G'' values were calculated from PMR data using the code developed by the Kilfoil lab at University of Massachusetts at Amherst [43].

3.3.6. Immunostaining

HT1080 and DF cells were cultured for 48 hours inside collagen hydrogels prepared in 12 well glass bottom plates (Cellvis) or inside fibrin hydrogels prepared in 35 mm glass bottom dishes (MatTek). Cells were then fixed in 4% paraformaldehyde (PFA, VWR) for 10 min at room temperature (RT), washed three times with PBS and permeabilized using 0.3% Triton X-100 (Sigma) diluted in PBS. Afterwards, cells were incubated in anti-YAP1 (G6)

antibody (sc-376830, Santa Cruz Biotechnologies) for 1 hour at RT, washed with 2% bovine serum albumin (BSA, VWR) diluted in PBS and incubated with secondary Alexa Fluor 594 Goat anti-Mouse IgG (BioLegend) antibody for another hour at RT. Subsequently, cells were washed with BSA, incubated with anti-fibronectin antibody (F3648, Sigma) for 1 hour at RT, washed again with 2% BSA and incubated with secondary Cyanine5 Goat anti-Rabbit IgG (Invitrogen) antibody for 1 hr at RT. Nuclei and F-actin were stained using NucBlue™ Live ReadyProbes™ Reagent (Hoechst 33342, Invitrogen) and Alexa Fluor 488 Phalloidin (Invitrogen) diluted in 2% BSA in PBS for 30 min at RT, respectively. Lastly, hydrogels were washed with PBS and covered with Fluoromount-G (Invitrogen).

3.3.7. Confocal microscopy and image analysis

Prior to AMR measurements, brightfield image of each cell was acquired using an EO-4010 Monochrome USB 3.0 Camera (Edmund Optics) incorporated in our AMR system and analyzed as described previously in **Chapter 2.3**. Briefly, images were processed in MATLAB (The MathWorks Inc.) using the image processing toolbox. The cell orientation was quantified by manually tracing the outline of the cell and using the *regionprops* function in MATLAB. After AMR measurements, the shortest distance between the pixel location of each probed bead and the manually traced cell shape cell was calculated in MATLAB and converted into micrometers. Angular position θ from 0° (cell front) to 180° (cell rear) relative to the long axis of the cell was found by calculating the angle between the pixel position of the bead and centroid of the cell.

Following AMR measurements, brightfield and reflection confocal microscopy (RCM) images of the probed FOV were collected using the 488 nm laser of the Fluoview 1200 laser scanning confocal microscope (Olympus) with the microscope objective lens used for AMR.

For DFs, brightfield images collected after AMR measurements were compared with brightfield images collected after AMR to identify the direction of cell migration and, consequently, cell front and cell rear. Beads distal to the cell served as fiducial markers for cell migration. In contrast, HT1080s did not migrate visibly during data acquisition and had more circular morphology, with no clear leading and trailing edge. Thus, cells were assumed to migrate towards the right direction with the exception of HT1080s cultured in fibrin that were assumed to migrate away from the ECM region broke down by fibrinolytic processes.

Immunostained cells were imaged one at a time using Fluoview3000 laser scanning microscope equipped with a UPlanXApo 10X/0.40 NA objective lens (Olympus). Z-stacks of images were collected with a step size of 1-2 μm, a scanning speed of 2 μs/pixel and a total scan resolution of 3.22 pixels per micron across area occupied by the cell. For each condition, 50 cells across 3 samples were imaged. Z-stacks of images were first analyzed in Fiji software [36] to find maximum intensity projection (MIP) across all image planes. MIP images were then processed using custom code written in MATLAB that masked the nuclei, F-actin and fibronectin regions. Nuclear/cytoplasmic ratio of YAP was calculated by dividing mean intensity of YAP inside the nuclei by mean intensity of YAP inside the cytoplasm colocalized with F-actin mask. Proportion of fibronectin found inside the cell was found by calculating the percentage of colocalization of fibronectin mask within F-actin mask. Cell morphological features including cell circularity calculated as $(4 \cdot Area \cdot \pi)/ (Perimeter)^2$ and solidity computed as $Area/ Convex\ Area$ [44] were analyzed using F-actin mask and *regionprops* function in MATLAB.

3.3.8. Statistical analysis

The effect and predictive power of various parameters on stiffness distribution around the cells was assessed using multivariate exponential regression (MER) conducted in R software [45,46]. All other statistical tests were performed in MATLAB. Comparison of non-normally distributed ($p < 0.01$, Kolmogorov-Smirnov test) stiffness values and parameters obtained from image analysis was conducted using non-parametric statistical analyses at a significance level of 0.05. The Friedman test was used to compare stiffness measurements between each oscillation axes. The Kruskal–Wallis test was performed for comparison of multiple groups. The post-hoc Tukey–Kramer test was used to compare specific groups. The Pearson correlation coefficient was used to quantify the correlation between stiffness and frequency of bead oscillation. The Ansari-Bradley test was used to compare differences in spread of data across tested types of ECM.

3.4. Results

3.4.1. Fibroblast response to type 1 collagen ECM of increasing concentration

Past studies by our group observed comparable stiffness levels around DFs cultured for 24 hours in rat tail T1C prepared at 1.0 mg/ml and 1.5 mg/ml [11]. In order to more thoroughly explore the effect of initial collagen concentration on peri-cellular stiffness, DFs were cultured for 48 hours inside rat tail T1C hydrogels polymerized at 4 different concentrations – 1.0 mg/ml (1.0T1C), 1.5 mg/ml (1.5T1C), 2.0 mg/ml (2.0T1C) and 3.0 mg/ml (3.0T1C). Prior to cell experiments, properties of cell-free hydrogels were assessed (**Figure 3.1A**). Median pore size decreased with concentration from 2.52 μm in 1.0T1C hydrogels to 1.39 μm in 3.0T1C hydrogels (**Figure 3.1B**). Stiffness (κ) of hydrogels was probed by oscillating at least 40 microbeads per hydrogel at 50 Hz along 4 different axes - at

0°, 45°, 90°, 135° with respect to the horizontal axis of the image (n_{sample} = 3). Just prior to each ECM measurement, AMR was first conducted in water to validate no bias towards any of the probed axes. As expected, κ of cell-free hydrogels increased with concentration (**Figure 3.1C**) and κ was found to be isotropic at each concentration (**Suppl. Figure 3.1**).

Next, κ was measured around DFs, which were found to have similar elongated morphology when cultured at all tested concentrations of rat tail T1C (**Figure 3.1E**). Stiffness was probed at 0°, 45°, 90°, 135° with respect to the long axis of the cell and graphed as illustrated in **Figure 3.1D**. For each probed bead, two coordinates were determined – a) the shortest distance between the bead and cell profile and b) angular position θ relative to the long axis of the cell in the counterclockwise direction, with origin at the cell centroid. Thus, each bead was placed within one of the twenty annular bins. Each bin is shaded according to the median κ value based on all beads analyzed in a particular bin. Each point corresponds to a probed bead and is color-codded for κ. Under the assumption of symmetry, the coordinate system was folded upon itself along the long axis of the cell. Spatial distribution of κ probed along the long axis of DFs is shown in **Figure 3.1F**, while κ probed in other directions is illustrated in **Suppl. Figure 3.2A-C**.

When analyzing all beads probed around DFs along all 4 axes (**Suppl. Figure 3.2D**), κ around cells was found to be higher than cell-free stiffness in 1.0T1C hydrogels ($p < 0.01$), but not different from cell-free stiffness in 1.5T1C ($p = 0.96$) and 2.0T1C ($p = 0.63$) hydrogels. For 3.0T1C hydrogels, stiffness around DFs was actually lower than cell-free stiffness ($p < 0.01$) at that concentration and comparable with κ around DFs embedded inside 2.0T1C hydrogels ($p = 0.88$).

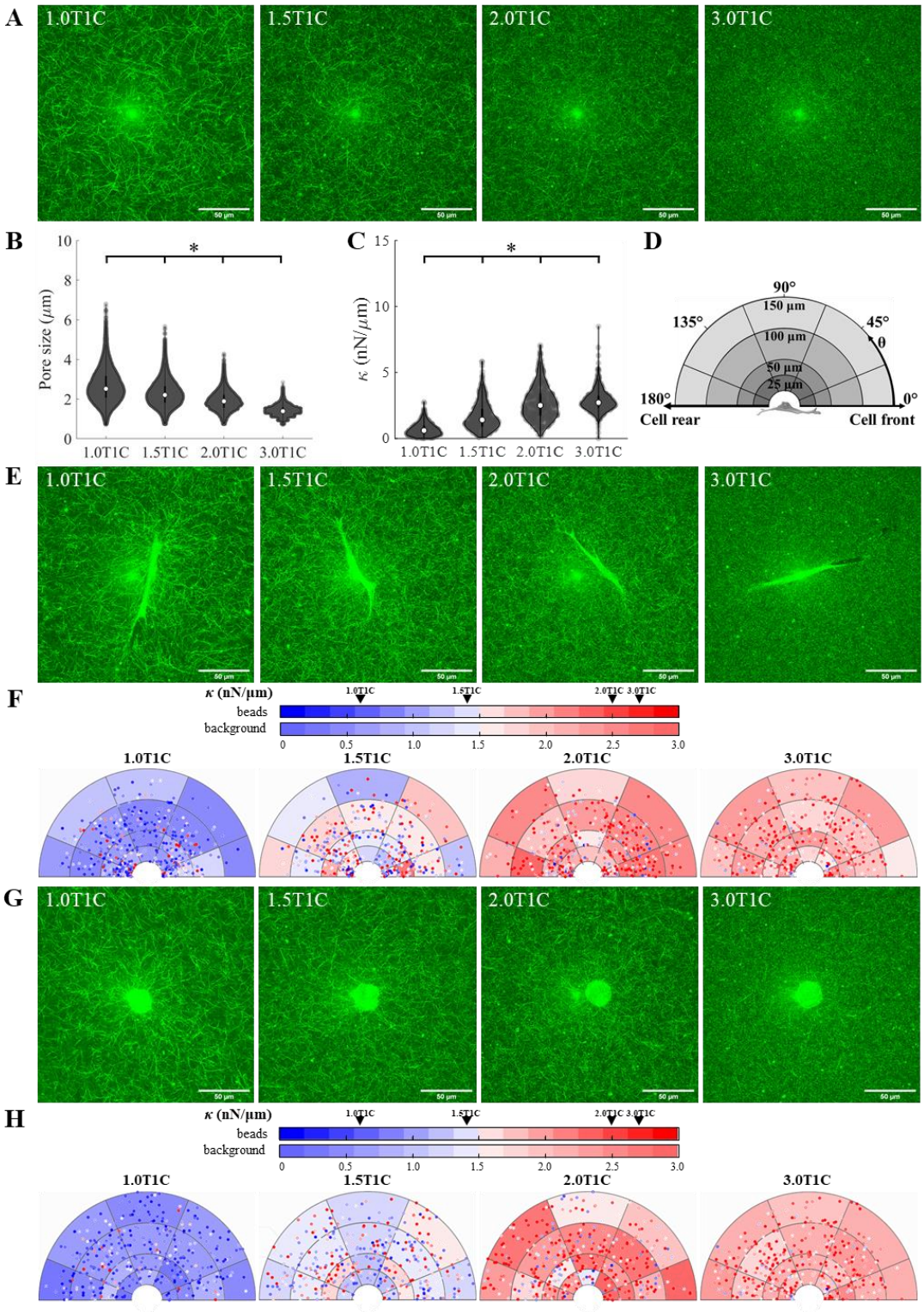

Figure 3.1. The effect of rat tail T1C concentration on stiffness distribution around DF and HT1080 cells. (A) Reflection confocal microscopy (RCM) images of cell-free hydrogels prepared at 4 concentrations (1.0, 1.5, 2.0, 3.0 mg/ml). (B) Pore size and (C) stiffness (κ) distribution of cell-free hydrogels. Median values are denoted by white markers. (D) Graphical representation of the coordinate system used to discretize the ECM region around a cell. (E) RCM images of DFs. (F)

Distribution of stiffness around DFs probed along the long axis of the cell. (G) RCM images of HT1080s. (H) Distribution of stiffness around HT1080s probed along the horizontal direction of the image. Background color is shaded according to the median κ value in each bin (background color bar). Each data point is a single probed bead, color-coded for κ (beads color bar). * $p < 0.05$

Multivariate exponential regression (MER) was used to determine significant predictors of κ from multiple independent parameters (**Suppl. Figure 3.2E**). Analyzed parameters included the continuous variables of shortest distance between the bead and cell profile and angular position θ, as well as the discrete variables of T1C concentration and axis of bead oscillation. Discrete variables were simply encoded with the reference to 1.0T1C concentration and oscillation along the long axis of the cell [45]. MER indicated that T1C concentration was a dominant predictor. κ increased with T1C concentration, but decreased with θ position. Surprisingly, distance away from the cell (up to 150 μm) and axes of bead oscillation were not found to be significant predictors of κ probed 48 hours after sample preparation. This finding is in contrast to our previously published data collected 24 hours after sample preparation [11]. Analysis of the peri-cellular region (< 25 μm, inner annulus) similarly found that κ was isotropic in 1.0T1C ($p = 0.93$), 1.5T1C ($p = 0.58$), 2.0T1C ($p = 0.75$) and 3.0T1C ($p = 0.72$) hydrogels. The parameters analyzed here were only able to explain 31.5% of the variance in κ, indicating that factors outside our consideration play an important role in predicting local ECM stiffness.

3.4.2. HT1080 response to type 1 collagen ECM of increasing concentration

In addition to analyzing stiffness around DFs, κ was also probed around highly invasive human fibrosarcoma HT1080 cells. Like DFs, HT1080s were cultured in rat tail T1C hydrogels for 48 hours prior to AMR measurements. In agreement with past studies [26,47], isolated HT1080 cells cultured in 3D rat tail T1C hydrogels exhibit rounded morphology (**Figure 3.1G**), preventing identification of a cell front. Thus, κ results are represented in a

similar way as for DFs, with the exception that stiffness was probed at 0°, 45°, 90°, 135° with respect to the horizontal axis of the image. For purposes of analysis and data presentation, a cell front was arbitrarily assigned as the right side of the cell with respect to the image.

When analyzing all beads in all directions of bead oscillation (**Suppl. Figure 3.3D**), κ around HT1080s was found to be comparable to cell-free stiffness for cells embedded in 1.0T1C (p = 0.98), 1.5T1C (p > 0.99) and 2.0T1C (p = 0.15) hydrogels. Stiffness around HT1080s in 3.0T1C hydrogels was lower than in cell-free 3.0T1C hydrogels (p < 0.01), but did not differ from κ around cells measured in 2.0T1C hydrogels (p = 0.38).

Spatial distribution of κ probed at 0° is visualized in **Figure 3.1H**. κ probed at other directions is included in **Suppl. Figure 3.3A-C**. MER of stiffness was conducted as for DF cells and analyzed parameters predicted 42.8% of variance in data (**Suppl. Figure 3.3E**). T1C concentration was found to be a dominant predictor of stiffness. Distance away from the cell, direction of bead oscillation and angular position θ were not significant predictors of stiffness. Analysis of the peri-cellular region indicated that stiffness was isotropic in 1.0T1C (p = 0.58), 1.5T1C (p = 0.94), 2.0T1C (p = 0.99) and 3.0T1C (p = 0.99) hydrogels.

In order to assess frequency effect on κ, AMR was conducted in the peri-cellular region of DFs and HT1080s (< 25 μm, n_{beads} ≥ 10 per cell) using wider range of frequencies. AMR data was collected at 20, 50 and 200 Hz at 0° and 90° with respect to long axis of the DFs or with respect to the horizontal axis of the image for HT1080s and cell-free measurements. As observed previously by us [11] and widely reported by other groups [37,48,49], κ increased with frequency of bead oscillation, but with the tenfold increase in frequency, κ changed on average only by 24% (**Suppl. Figure 3.4**).

10 beads closest to each cell were also used as probes for passive microrheology (PMR), during which the trapping beam, but not the detection beam, was blocked by a mechanical shutter. Data was recorded for 30 s, with a sampling frequency of 10,000 Hz. Viscoelasticity of hydrogels, reported as the complex valued shear modulus $G^* = G' + iG''$ (Pa), was calculated from the mean-square displacement spectrum of each bead for PMR data [43,50]. For AMR data, G^* was calculated from κ^* using the generalized Stokes relation [37,38]. G' values from PMR were higher than G'' from PMR (**Suppl. Figure 3.5**), but significantly lower than G' measured by AMR (**Suppl. Figure 3.6**). In contrast, G'' values were larger when measured by PMR than by AMR ($p < 0.01$).

3.4.3. Fibroblast response to stiffness-matched type 1 collagens and fibrin ECMs

In the next set of experiments, we assessed the effect of ECM type on peri-cellular stiffness. Instead of matching matrix concentrations, concentrations of fibrin and bovine skin T1C hydrogels were selected to result in median stiffness levels matching the cell-free stiffness of rat tail T1C polymerized at 1.5 mg/ml. Thus, bovine skin T1C hydrogels were prepared at 1.75 mg/ml and fibrin hydrogels were polymerized at 2.7 mg/ml (**Figure 3.2A**). Despite having similar median stiffness values ($p = 0.94$), the dispersion of stiffness values was much greater for bovine skin T1C ($p < 0.01$) and much smaller for fibrin ($p < 0.01$) than for rat tail T1C (**Figure 3.2B**, **Suppl. Figure 3.1C**). Different types of ECM also resulted in distinct fiber architectures. As compared to rat tail T1C hydrogels, median pore size and dispersion of pore size values was greater for bovine skin T1C hydrogels ($p < 0.01$) and lesser for fibrin hydrogels ($p < 0.01$, **Figure 3.2C**).

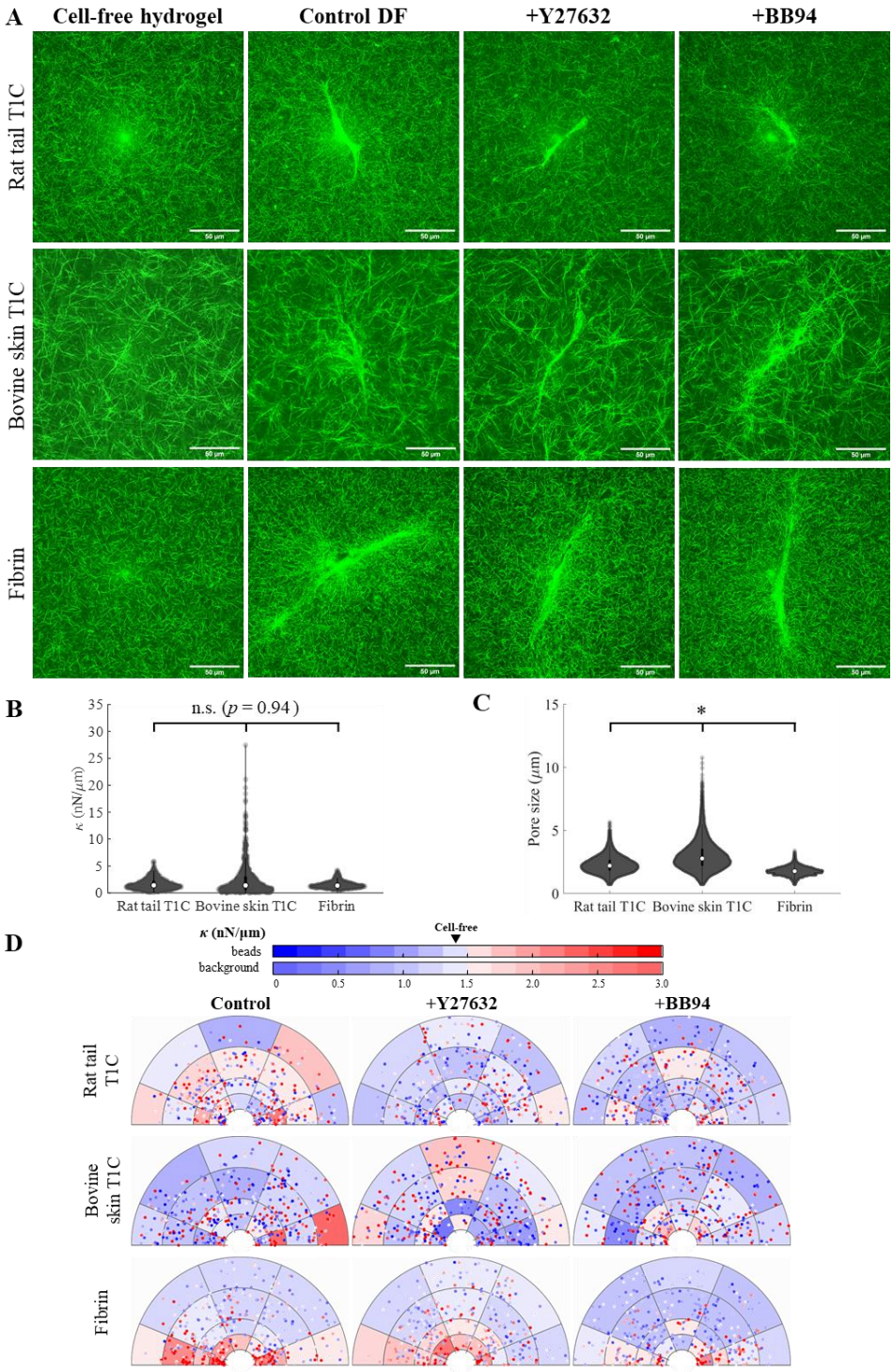

Figure 3.2. The effect of ECM type and treatment on stiffness distribution around DFs. (A) RCM images of cell-free hydrogels (rat tail T1C, bovine skin T1C, fibrin) and hydrogels containing DFs either untreated or treated with Y27632 and BB94. (B) Stiffness κ and (C) pore size distribution of cell-free hydrogels. Median values are denoted by white markers. (D) κ distribution around DFs, probed along long axis of the cell. Background color is shaded according to the median κ value in each bin (background color bar). Each data point is a single probed bead, color-coded for κ (beads color bar). * $p < 0.05$

DFs were shown to regulate their local ECM stiffness differently based on type of hydrogel in which they were cultured in for 48 hours. Spatial stiffness distribution probed along the long axis of the cell is shown in **Figure 3.2D**. Results showing κ distribution along other directions are included in **Suppl. Figure 3.7A-C**. MER was used to assess whether type of ECM as well as axis of bead oscillation, the shortest distance between the probed bead and a cell and angular position θ are significant predictors of κ (**Suppl. Figure 3.7D**). Discrete variables of oscillation axis and ECM type were simply encoded with the reference to cell orientation angle and rat tail T1C, respectively. While analyzed parameters explained only 5% of data variance, κ was found to strongly depend on type of ECM. Cells in bovine skin T1C established lower κ ($p < 0.01$), and cells in fibrin hydrogels promoted higher κ ($p < 0.01$) as compared to κ around cells in rat tail T1C or κ of cell free hydrogels. In contrast, κ around cells cultured in rat tail T1C did not differ from the cell-free stiffness ($p = 0.96$). Distance from the cell profile was also found to be a significant predictor of κ. Distance-dependance on κ is especially evident when stiffness was probed around DFs cultured in fibrin hydrogels. Peri-cellular stiffening was observed in fibrin and while stiffness decreased with distance away from the cell ($p < 0.01$), stiffening in regions towards cell front and cell back was evident up to 100 μm away from the cell, when beads are oscillated along the long axis of the cell (**Figure 3.2D**, $p < 0.01$).

Next, the effect of two treatments (Y27632 and BB94) on stiffness landscape around DFs was assessed. MER indicated that cell response to treatments varied depending on ECM type (**Suppl. Figure 3.7E**). As compared to control conditions (no treatment), addition of Y27632 or BB94 resulted in lower κ values in rat tail T1C and fibrin hydrogels, but treatment effect was not observed in bovine skin T1C. In rat tail T1C hydrogels, Y27632 or BB94

lowered stiffness to levels below cell-free κ ($p < 0.01$), but in fibrin hydrogels BB94 was more effective than Y27632 in reducing peri-cellular stiffening. However, following treatment with either Y27632 or BB94, κ in fibrin hydrogels remained higher in the peri-cellular region (< 25 μm, inner annulus) than in the distal region (>25 μm, $p < 0.01$). Further, only in fibrin hydrogels, κ around DFs varied based on axis of bead oscillation (**Suppl. Figure 3.7**).

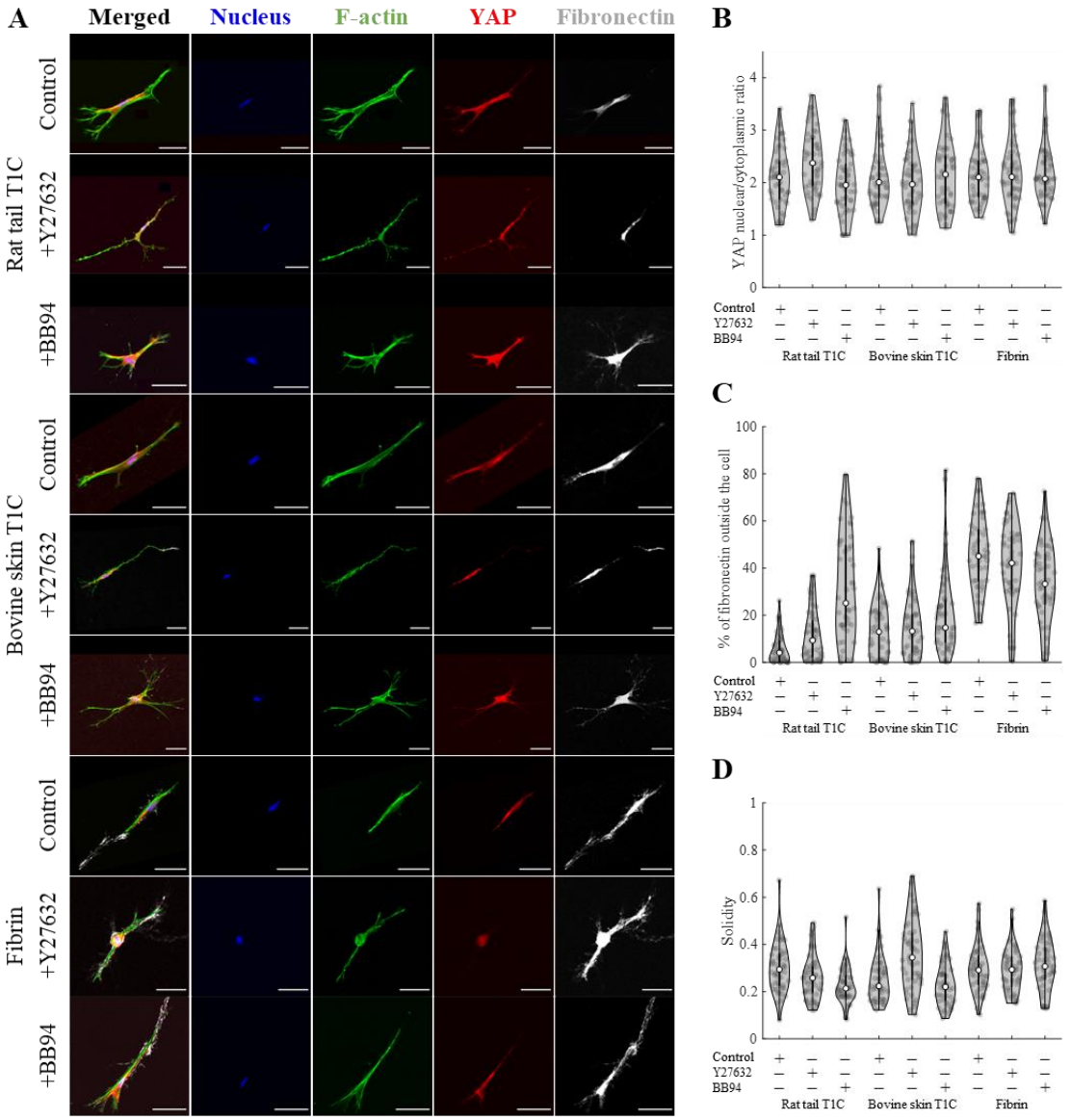

Figure 3.3. The effect of ECM type and treatment on nuclear/cytoplasmic YAP ratio, fibronectin secretion and solidity of DFs. (A) Immunofluorescent confocal images of DFs. Scale bar = 50 μm. Quantification of (B) nuclear/cytoplasmic YAP ratio, (C) fibronectin secretion, described as % of fibronectin signal found outside of the cell and (D) cell solidity. Statistical comparison between the groups for (B-D) is shown in Suppl. Table 3.1.

In addition to probing local stiffness, confocal microscopy was conducted to image relative expressions and/or locations of F-actin, YAP, fibronectin, and the cell nucleus (**Figure 3.3A**). Despite considerably different κ landscapes around DFs cultured in different types of ECM, nuclear/cytoplasmic YAP ratio was found to be comparable for control cells cultured in different types of hydrogels ($p = 0.77$, **Figure 3.3B**, **Suppl. Table 3.1A**). Similarly, addition of either Y27632 or BB94 did not alter nuclear/cytoplasmic YAP ratio as compared to control cells in any type of ECM. Fibronectin secretion, reported as % of total detected fibronectin found outside of the cell, was shown to differ more prominently between the ECM types, but treatment effect was not widely observed (**Figure 3.3C**, **Suppl. Table 3.1B**). In contrast, solidity of DFs did not differ across the tested types of ECM, but addition of either BB94 or Y27632 altered solidity of cells in collagen hydrogels (**Figure 3.3D**, **Suppl. Table 3.1C**). Nonetheless, fibroblasts exhibited mostly elongated cell morphology, which did not differ greatly between tested conditions.

3.4.4. HT1080 response to stiffness-matched type 1 collagens and fibrin ECMs

Next, fibrosarcoma HT1080 cells were subjected to different types of ECM (**Figure 3.4A**). Of note, significant fibrinolysis was observed when cells were cultured in fibrin hydrogels. Consequently, while stiffness κ was still probed at 0°, 45°, 90°, 135° with respect to the image, for cells embedded in fibrin, cell front was assigned away from the region of enzymatic breakdown of fibrin (indicated by arrows in **Figure 3.4A**), instead of arbitrary assigning cell front to the right side of the cell. Spatial distribution of κ along the 0° direction (for collagen hydrogels) or along the direction closest to the orientation of the enzymatic breakdown (for fibrin hydrogels) is shown in **Figure 3.4B**. κ measurements along other axes are illustrated in **Suppl. Figure 3.8A-C**.

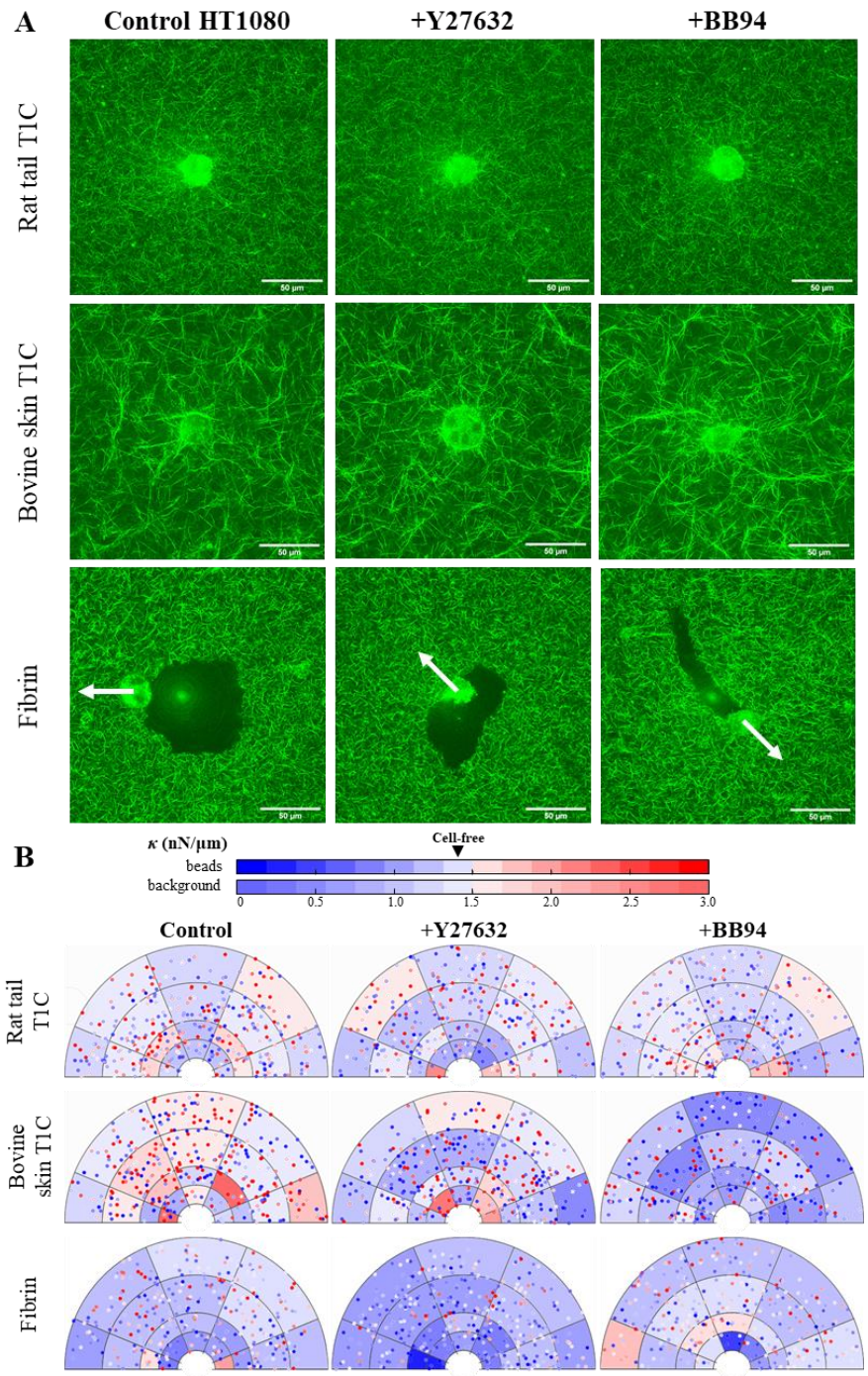

Figure 3.4. The effect of ECM type and treatment on stiffness distribution around HT1080s. (A) RCM images of HT1080 cells cultured in 3 different types of hydrogels (rat tail T1C, bovine skin T1C, fibrin), untreated or treated with Y27632 and BB94. (B) κ distribution around HT1080s, probed along horizontal axis of the image for cells cultured in rat tail or bovine skin T1C. For cells cultured in fibrin hydrogels, κ was probed along the direction closest to the orientation of the enzymatic breakdown, as indicated by the white arrows seen in (A). Background color is shaded according to the median κ value in each bin (background color bar). Each data point is a single probed bead, color-coded for κ (beads color bar). * $p < 0.05$

MER of local ECM stiffness indicated that culturing HT1080s in bovine skin T1C or in fibrin hydrogels resulted in lower κ values as compared to stiffness measured in rat tail T1C hydrogels (**Suppl. Figure 3.8D**). However, κ measured in bovine skin T1C did not differ significantly from κ of cell-free hydrogels (p = 0.71). Decrease in stiffness was more pronounced in fibrin hydrogels and local κ values were shown to be lower towards ECM regions broken down by the cells (towards cell rear).

Treatment effect was observed in all tested types of ECM. Addition of Y27632 or BB94 led to reduction in local κ around HT1080s cultured in rat tail T1C and bovine T1C, yet this effect was more evident in bovine T1C hydrogels (**Suppl. Figure 3.8E**). While Y27632 and BB94 promoted similar stiffness values in rat tail T1C (p = 0.17), BB94 reduced κ more efficiently than Y27632 in bovine skin T1C hydrogels ($p < 0.01$). In fibrin hydrogels, addition of Y27632 led to significant decrease in κ around HT1080s. In contrast, addition of BB94 resulted in increase in local κ, yet local stiffness was still below the κ of cell-free hydrogels ($p < 0.01$) and fibrinolysis was still exhibited by the cells. Only in fibrin hydrogels, distance between the probed bead and cell and angular position θ (arbitrary for HT1080s in collagen hydrogels) were found to be significant predictors of κ. κ was found to increase further away from the cell and away from the region broken down by fibrinolysis.

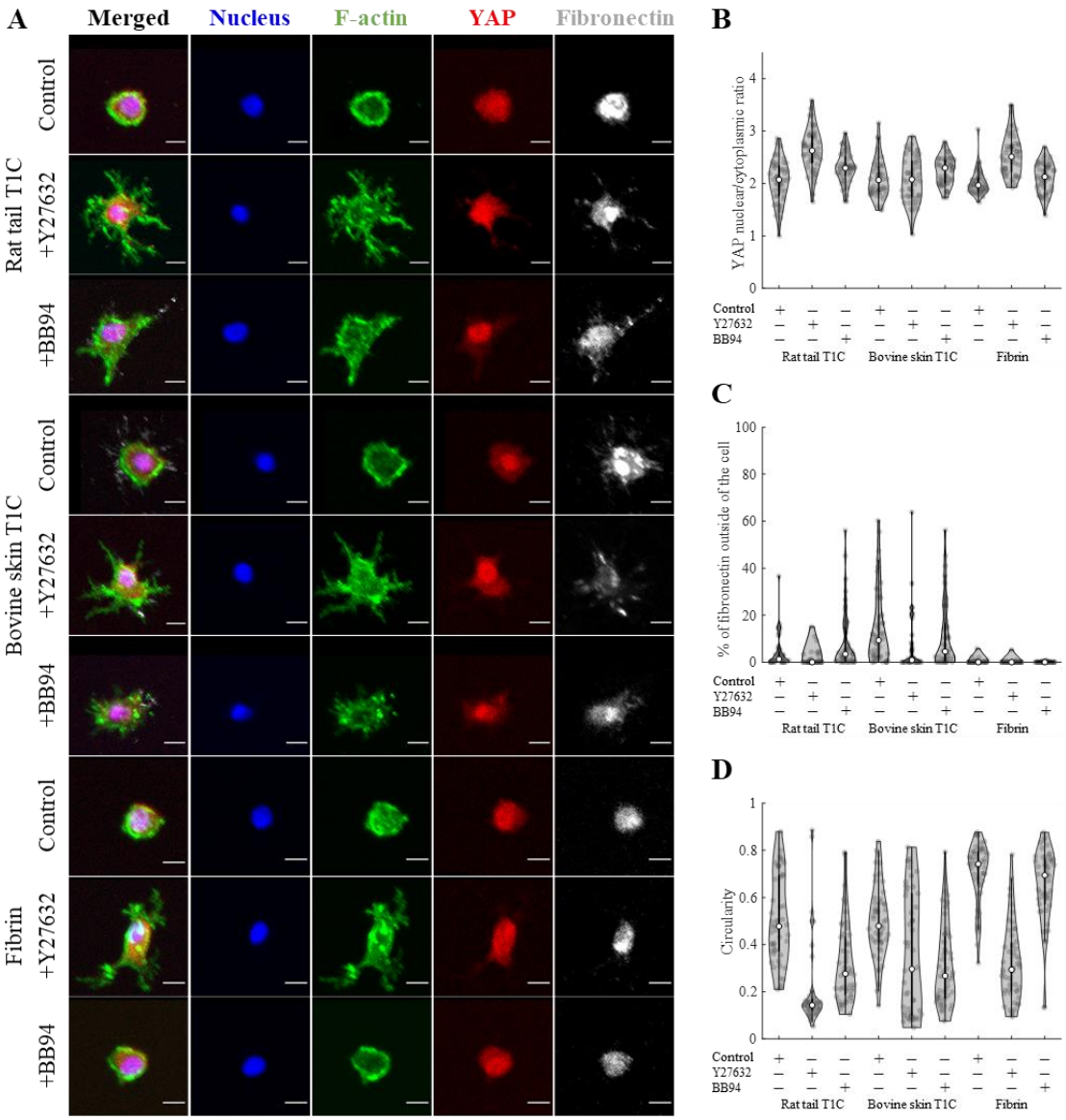

Figure 3.5. The effect of ECM type and treatment on nuclear/cytoplasmic YAP ratio, fibronectin secretion and circularity of HT1080s. (A) Immunofluorescent confocal images of HT1080s. Scale bar = 10 μm. Quantification of (B) nuclear/cytoplasmic YAP ratio, (C) fibronectin secretion, described as % of fibronectin signal found outside of the cell and (D) cell circularity. Statistical comparison between the groups for (B-D) is shown in Suppl. Table 3.2.

ECM type and tested treatments altered not only local κ landscapes, but also affected various cell properties (**Figure 3.5A**, **Suppl. Table 3.2**). Nuclear/cytoplasmic YAP ratio did not differ for control cells cultured in different types of hydrogels, but differed following treatments for cells in rat tail T1C or in fibrin (**Figure 3.5B**). While the extent of fibronectin secretion (**Figure 3.5C**) and cell circularity (**Figure 3.5D**) was comparable for cells cultured

in different types of collagen, fibronectin secretion decreased and circularity increased when cells were cultured inside fibrin hydrogels. Addition of either Y27632 or BB94 promoted more dendritic morphology of HT1080s, but treatment effect on other nuclear/cytoplasmic YAP ratio and fibronectin secretion varied with type of ECM (**Suppl. Table 3.2**).

3.5. Discussion

Stiffness around cells was previously shown by our group to depend on T1C concentration [11] and vary with different treatments and between tested cell lines [11,34]. Here, we add new information about stiffness and its anisotropy around two cell lines cultured in distinct ECMs, varying in source, porosity and concentration. For all conditions, G' values were significantly lower when calculated from PMR data than when estimated from AMR data (**Suppl. Figure 3.6**). These results are in agreement with previously reported data that found passive microrheology to underestimate G' due to lower signal-to-noise ratio and the assumption of thermal equilibrium that does not account for the influence of the optical trap and external forces from the cells in calculations of the G^* modulus [37,38]. Further, the calculation of G^* assumes the material is in a local continuum, and that pore size is considerably smaller than the probe bead [37,38], which is not the case for rat tail 1.0T1C, 1.5T1C and 2.0T1C hydrogels. However, in cell-free 3.0T1C hydrogels (**Figure 3.1B**), the pore size distribution shows that most pores are smaller than the bead diameter (2 μm). This crossing of spatial scale may influence the interpretation of AMR data, and may explain in part the similarity in stiffness distribution between 2.0T1C and 3.0T1C hydrogels.

Stiffness around DFs and HT1080s was probed in 4 distinct directions elucidating local anisotropies. Stiffness and cell properties, including expressed nuclear/cytoplasmic YAP ratio, cell solidity or circularity and percentage of secreted fibronectin were shown to

vary across the tested ECM types and treatments, indicating a complex cell-ECM relationship based on a variety of factors and characteristics of both cells and the ECM. ECM concentration was found to be a dominant predictor of local stiffness for DFs and HT1080s cultured at different concentrations of rat tail T1C (**Figure 3.1**, **Suppl. Figure 3.2**, **Suppl. Figure 3.3**). These findings are seemingly in opposition to our past studies that found peri-cellular stiffness to be comparable around DFs cultured for 24 hours in rat tail 1.0T1C or 1.5T1C hydrogels [11]. Peri-cellular stiffening observed 24 hours after hydrogel preparation was not observed in the current study at the 48 hour time point. Further, in contrast to our previous studies [11], stiffness was largely unaffected by distance from the cell, angular position θ, and axes of bead oscillation. Discrepancy in results could potentially stem from the difference in duration of cell culture, as supported by past research that found hydrogel stiffness to vary with cell incubation time [51,52]. Reported results are most likely also affected by additional factors outside the scope of this project, including cell seeding density [52], discrepancies in collagen lots [53] and cell area [54–56].

Both DFs and HT1080s were also shown to respond differently when cultured in three distinct types of hydrogels, formulated to have comparable cell-free median stiffness (**Figure 3.2B**). Our results indicate that cell response to an ECM might not be governed by median stiffness levels alone. Past studies found that cells sense local stiffness anisotropies in 3D hydrogels [42] and thus, cells might also be sensitive to the magnitude of local variances in stiffness within the hydrogels (**Figure 3.2B**). Further, all three types of hydrogels exhibited distinct porosities and microarchitectures – factors, which are known to significantly affect cell survival, proliferation, and migration [57–59]. In addition to detecting differences in mechanical properties of hydrogels, cell behavior is known to vary with

biochemical properties of the ECM [2,60–62], which is also corroborated by our study. The impact of ECM type on cell properties and local stiffness levels was most pronounced when comparing data collected in collagen hydrogels and fibrin hydrogels. For example, while DFs promoted peri-cellular stiffening in fibrin as compared to either rat tail or bovine skin T1C (**Figure 3.2D**), HT1080s prominently degraded local fibrin, but not collagen matrix (**Figure 3.4A**) [63–65]. Even though stiffness levels increased following BB94 treatment of HT1080s in fibrin, fibrinolysis was still observed (**Figure 3.4**). This observation could be consistent with the molecular action of BB94, which is a broad spectrum inhibitor of zinc MMPs, whereas the enzymatic breakdown of fibrin by HT1080s is associated with expression of serine proteases and not directly with MMP activity [66,67].

Rat tail T1C and bovine skin T1C were prepared using the same protocol and differed only with the tissue source of telocollagen. Based on results of SPS-Page tests available from the manufacturer, both types of collagen exhibited similar purity with over 85% of T1C contained within contained within α, β and γ bands. Nonetheless, discrepancy in fiber architectures between the two sources of collagen (**Figure 3.2A-B**) could potentially stem from small differences in amino acid compositions, presence of distinct collagen subtypes other than type 1 or different fibrillogenesis dynamics, which were all previously shown to differ with collagen source, including tissue type and species [68–70]. In our study, cells embedded in bovine skin T1C hydrogels with larger pore sizes established lower stiffness values than cells cultured inside rat tail T1C hydrogels with smaller pores (**Figure 3.2B**). These findings indicate that local ECM stiffness established by the cells decreases with the pore size. However, the relationship may not be causal because the cells can also respond to biochemical differences between the collagen types [47]. While cells were shown to

differentially respond to different types of ECM, the small predictive power of MER suggests that a more comprehensive analysis of factors governing peri-cellular stiffness is still required.

Despite observed effect of ECM type and treatment on stiffness around cells, change in nuclear/cytoplasmic YAP was only detected for Y27632 treatment of HT1080 cells (**Figure 3.4B**, **Suppl. Table 4.2**). While YAP expression was shown to be more prominent inside the nuclei than inside cell cytoplasm for all tested conditions, YAP signal was still widely distributed throughout each cell. Translocation of YAP to the nucleus has been widely reported for cells cultured on 2D substrates with increasing stiffness [71–73], yet translocation was shown to occur at different stiffness values based on cell or substrate type or tested treatment [74–77]. For 3D cultures, YAP translocation into the nucleus also varied with cell and ECM type [72,78,79]. For example, past studies on fibroblasts embedded inside synthetic fibrous hydrogels reported increase in nuclear/cytoplasmic YAP ratio with fiber density [78], indicating a role in mechanotransduction, but mechanotransduction of human breast cancer cells in 3D cultures was found to be independent of YAP [79]. We assert that, to further understanding of the role of YAP in mechanosensing requires measurements of local peri-cellular and not bulk stiffness of the ECM. Such studies may clarify the signal-to-stiffness relationship. Our findings presented here do measure the stiffness sensed by the cells and provide new, but far from comprehensive, understanding regarding roles of ECM types and tested treatments on YAP ratio. Despite no prominent difference in nuclear/cytoplasmic YAP between analyzed conditions, lack of change in YAP ratio could also be attributed to a narrow range of tested stiffnesses in our study (G' = 0.1-1000 Pa), preventing more prominent YAP translocation to nuclei in stiffer hydrogels or to cytoplasm in softer hydrogels.

Comparatively, fibronectin secretion was shown to be more correlated with local stiffness (**Figure 3.3C**, **Figure 3.5C**). For instance, DFs exhibited highest peri-cellular stiffness and fibronectin secretion inside fibrin hydrogels as compared to collagen hydrogels. In contrast, HT1080s promoted much lower stiffness levels and fibronectin secretion inside fibrin hydrogels than inside collagen hydrogels. Nonetheless, after 48 hours of cell culture, fibronectin expression, considered to be colocalized with newly secreted collagen [80–82], was not prominent in the extracellular space. Most of the fibronectin signal was detected inside the cells (**Figure 3.3A**), which is in agreement with past studies on fibroblasts in fibrin hydrogels after 48 hours of culture [83,84]. Similarly, collagen secreted by fibroblasts cultured in collagen hydrogels was previously found to be limited to the cell perimeter after 48 hours of culture and was present throughout the whole hydrogel only after 12 days of culture [85]. While DFs promote formation of fibronectin fibrils [83,84], HT1080s possess limited ability to assemble fibronectin fibrils without dexamethasone stimulation [86,87]. In agreement with past research, our study shows that fibronectin secretion by HT1080s was largely non-fibrillar and lesser in extent than observed for DFs (**Figure 3.5A**). Extent of fibronectin expression indicates that ECM probed by AMR was composed of mostly original, not cell-secreted, ECM. Nonetheless, trends in stiffness across tested ECMs were shown to follow trends in fibronectin expression, and further studies are required to explicate the relationship between peri-cellular stiffness and ECM secretion by cells.

Differential effect of ECM type on how cells remodel the matrix is further evidenced by the addition of Y27632 or BB94 treatments. Stiffening of local matrix by the tested cell types is known to be mediated by contractile forces, which can be inhibited by Y27632 [10,11,88] and local matrix degradation by MMP secretion, which is inhibited by BB94 [29–31].

Interestingly, past studies by our group have showed that MMP secretion can also contribute to stiffening of the ECM, most likely by allowing cell elongation within a dense ECM [10]. In fact, MMP activity and cell contractility were essential to ECM stiffening for the case of dermal fibroblasts and aortic smooth muscle cells in type 1 collagen [10]. Results from our current study support this finding across multiple ECM types (**Figure 3.2D**, **Figure 3.4B**, **Suppl. Figure 3.7**, **Suppl. Figure 3.8**), and further show that Y27632 and BB94 treatments also alter morphology of both cell types, yet the effect of Y27632 and BB94 on YAP and fibronectin expression varied with the type of ECM (**Figure 3.3**, **Figure 3.5**).

In conclusion, we investigated complex relationship between stiffness established by dermal fibroblasts or HT1080 fibrosarcoma cells and ECM properties, such as hydrogel concentration, type, fiber architecture and pore size. While tested cell lines created highly heterogeneous stiffness landscapes, cell response did not vary with the initial concentration of rat tail T1C hydrogel. In contrast, cells responded differentially when embedded inside different types of ECMs with matched initial stiffness. Given that rat tail T1C, bovine skin T1C and fibrin hydrogels were polymerized at concentrations promoting similar stiffness values in cell-free hydrogels, this work provides further evidence of the importance of measuring peri-cellular and not bulk properties of the ECM. As bulk stiffness might not reflect stiffness sensed by the cells, peri-cellular measurements should be included in comprehensive studies on cellular mechanotransduction.

3.6. Acknowledgments

We would like to thank Dr. Vijaykumar S. Meli for his assistance with immunostaining and Lawrence Vulis for his help with exponential regression analysis. Research reported in this publication was supported by the United States National Science Foundation (US-NSF) under

Award Number DMS-1953410, and by the National Institutes for Health (NIH) under Award Number (NIH R01-HL085339). The content is solely the responsibility of the authors and does not necessarily represent the official views of the US-NSF and the NIH. Approximately, $50,000 of United States federal funds supported the effort (100%) on this project. Use of confocal microscope Fluoview3000 inside the Edwards Lifesciences Foundation Cardiovascular Innovation and Research Center was supported by (NIH 1S10OD025064-01A1). No effort on this project was supported by non-federal funds.

3.7. Supplementary materials

A

	Angle of oscillation	1.0T1C	1.5T1C	2.0T1C	3.0T1C
Median ± IQR κ (nN/μm)	All angles	0.61 ± 0.63	1.41 ± 1.29	2.51 ± 1.64	2.72 ± 0.86
	0°	0.61 ± 0.61	1.47 ± 1.43	2.43 ± 1.39	2.82 ± 0.97
	45°	0.62 ± 0.59	1.47 ± 1.21	2.60 ± 1.58	2.67 ± 0.87
	90°	0.58 ± 0.68	1.33 ± 1.29	2.59 ± 1.75	2.66 ± 0.85
	135°	0.60 ± 0.63	1.44 ± 1.29	2.60 ± 1.71	2.72 ± 0.74
n_{beads}		128	141	153	149
$n_{samples}$		3	3	3	3
Kruskal-Wallis test		$p = 0.84$	$p = 0.96$	$p = 0.44$	$p = 0.57$

B

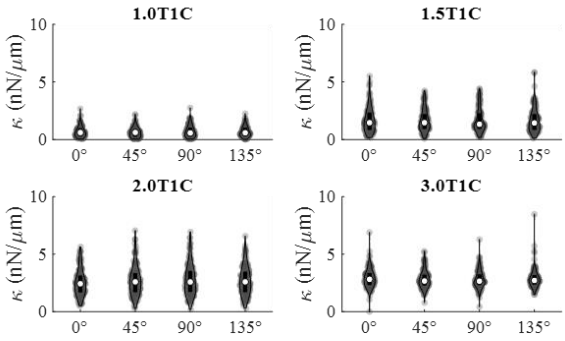

C

	Angle of oscillation	Rat tail T1C	Bovine skin T1C	Fibrin
Median ± IQR κ (nN/μm)	All angles	1.41 ± 1.29	1.39 ± 2.39	1.36 ± 0.69
	0°	1.47 ± 1.43	1.52 ± 1.93	1.41 ± 0.75
	45°	1.47 ± 1.21	1.42 ± 2.69	1.36 ± 0.70
	90°	1.33 ± 1.29	1.46 ± 2.50	1.36 ± 0.74
	135°	1.44 ± 1.29	1.31 ± 2.40	1.31 ± 0.69
n_{beads}		141	186	138
$n_{samples}$		3	3	3
Kruskal-Wallis test		$p = 0.96$	$p = 0.99$	$p = 0.82$

Suppl. Figure 3.1. Stiffness κ probed inside cell-free T1C hydrogels. Median ± IQR κ values (A) and κ distributions (B) for cell-free hydrogels polymerized at 4 different concentrations and probed along 4 distinct axes. (C) Median κ values for 3 different types of hydrogels (rat tail T1C, bovine skin T1C, fibrin) polymerized at concentrations resulting in similar stiffness values. Isotropy of cell-free hydrogels is assessed using the Kruskal-Wallis test (A,C).

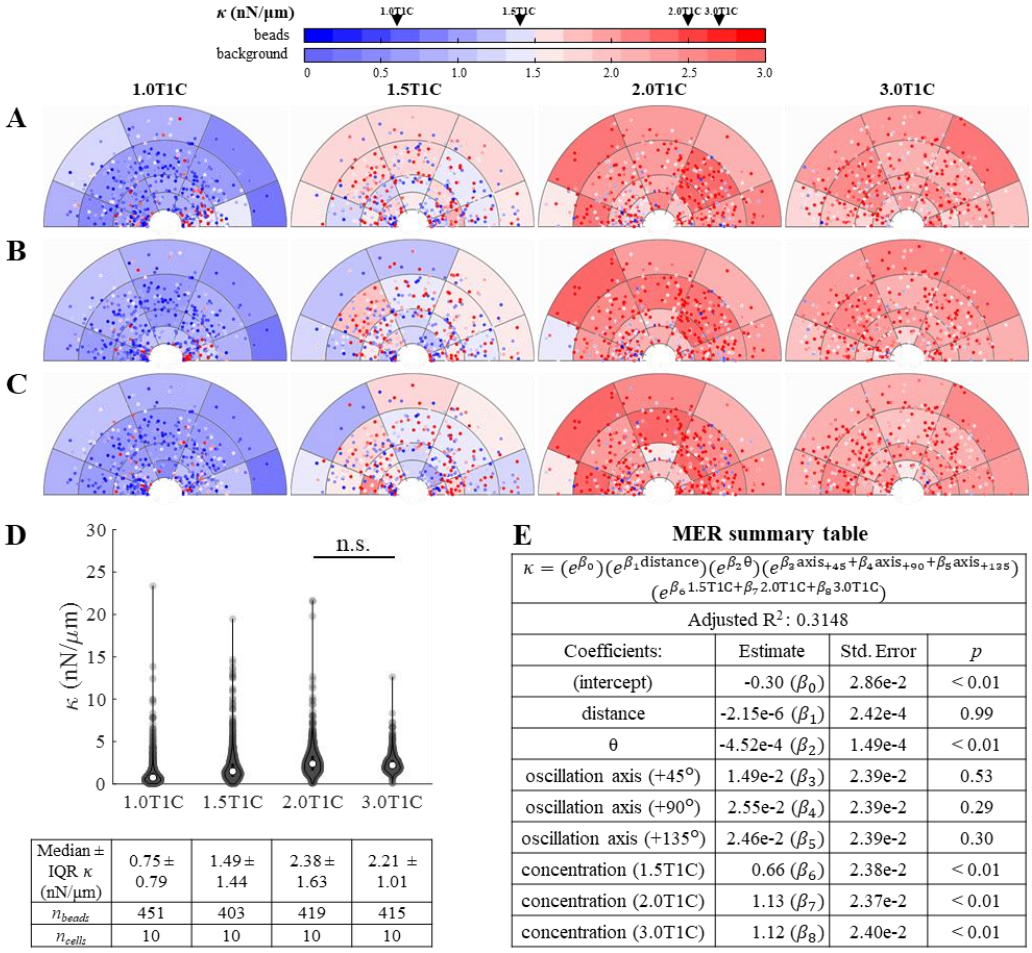

Median ± IQR κ (nN/μm)	0.75 ± 0.79	1.49 ± 1.44	2.38 ± 1.63	2.21 ± 1.01
n_{beads}	451	403	419	415
n_{cells}	10	10	10	10

E **MER summary table**

$\kappa = (e^{\beta_0})(e^{\beta_1 \text{distance}})(e^{\beta_2 \theta})(e^{\beta_3 \text{axis}_{+45} + \beta_4 \text{axis}_{+90} + \beta_5 \text{axis}_{+135}})(e^{\beta_6 1.5\text{T1C} + \beta_7 2.0\text{T1C} + \beta_8 3.0\text{T1C}})$

Adjusted R^2: 0.3148

Coefficients:	Estimate	Std. Error	p
(intercept)	-0.30 (β_0)	2.86e-2	< 0.01
distance	-2.15e-6 (β_1)	2.42e-4	0.99
θ	-4.52e-4 (β_2)	1.49e-4	< 0.01
oscillation axis (+45°)	1.49e-2 (β_3)	2.39e-2	0.53
oscillation axis (+90°)	2.55e-2 (β_4)	2.39e-2	0.29
oscillation axis (+135°)	2.46e-2 (β_5)	2.39e-2	0.30
concentration (1.5T1C)	0.66 (β_6)	2.38e-2	< 0.01
concentration (2.0T1C)	1.13 (β_7)	2.37e-2	< 0.01
concentration (3.0T1C)	1.12 (β_8)	2.40e-2	< 0.01

Suppl. Figure 3.2. Supplementary material to Figure 3.1F. Stiffness κ distribution around DFs probed at (A) +45°, (B) +90° and (C) +135° with respect to the long axis of the cell. (D) κ distributions around DFs cultured in rat tail T1C polymerized at 4 different concentrations. Plots aggregate κ probed in all 4 directions. (E) MER summary table. Discrete variables of oscillation axis and concentration were simply encoded with the reference to cell orientation angle and 1.0T1C concentration.

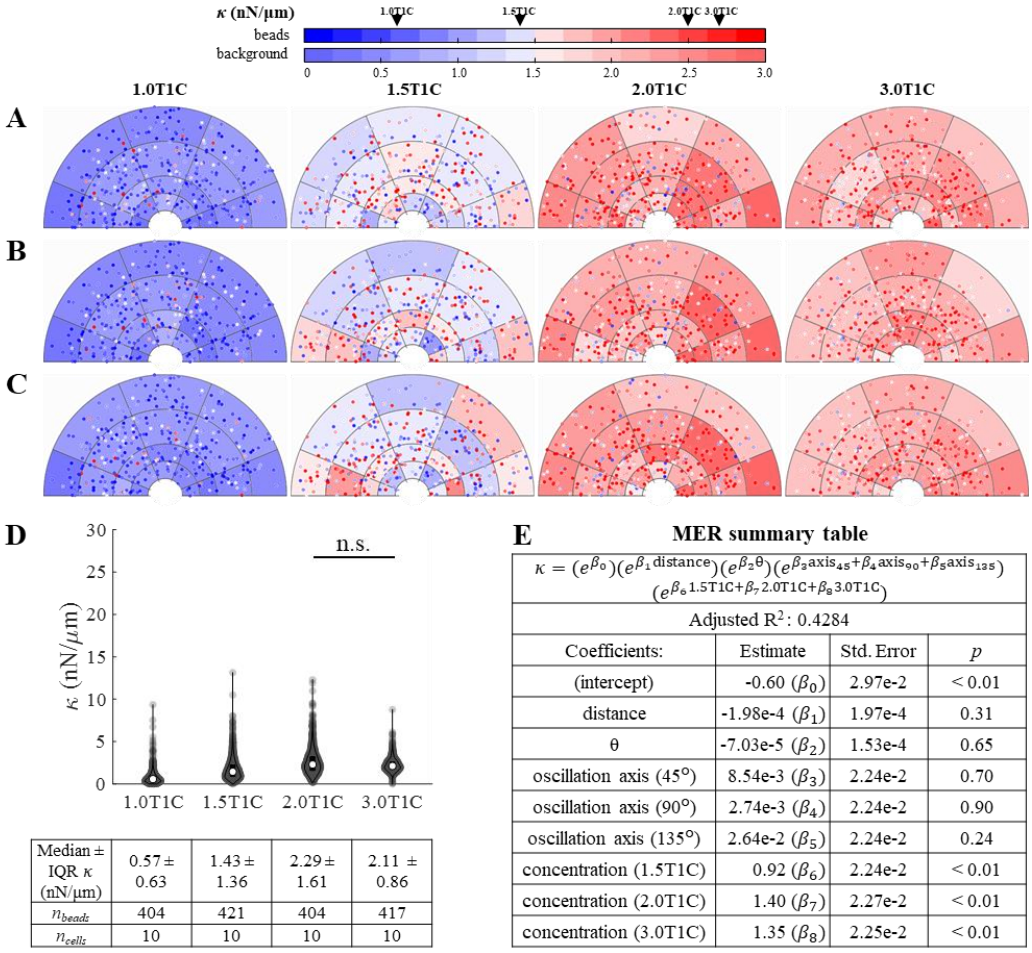

Median ± IQR κ (nN/μm)	0.57 ± 0.63	1.43 ± 1.36	2.29 ± 1.61	2.11 ± 0.86
n_{beads}	404	421	404	417
n_{cells}	10	10	10	10

E **MER summary table**

$\kappa = (e^{\beta_0})(e^{\beta_1 \text{distance}})(e^{\beta_2 \theta})(e^{\beta_3 \text{axis}_{45} + \beta_4 \text{axis}_{90} + \beta_5 \text{axis}_{135}})(e^{\beta_6 1.5\text{T1C} + \beta_7 2.0\text{T1C} + \beta_8 3.0\text{T1C}})$

Adjusted R^2: 0.4284

Coefficients:	Estimate	Std. Error	p
(intercept)	-0.60 (β_0)	2.97e-2	< 0.01
distance	-1.98e-4 (β_1)	1.97e-4	0.31
θ	-7.03e-5 (β_2)	1.53e-4	0.65
oscillation axis (45°)	8.54e-3 (β_3)	2.24e-2	0.70
oscillation axis (90°)	2.74e-3 (β_4)	2.24e-2	0.90
oscillation axis (135°)	2.64e-2 (β_5)	2.24e-2	0.24
concentration (1.5T1C)	0.92 (β_6)	2.24e-2	< 0.01
concentration (2.0T1C)	1.40 (β_7)	2.27e-2	< 0.01
concentration (3.0T1C)	1.35 (β_8)	2.25e-2	< 0.01

Suppl. Figure 3.3. Supplementary material to Figure 3.1H. Stiffness κ distribution around HT1080s probed at (A) 45°, (B) 90° and (C) 135° with respect to the horizontal axis of the image. (D) κ distributions around HT1080s cultured in rat tail T1C polymerized at 4 different concentrations. Plots aggregate κ probed in all 4 directions. (E) MER summary table. Discrete variables of oscillation axis and concentration were simply encoded with the reference to horizontal axis of the image and 1.0T1C concentration.

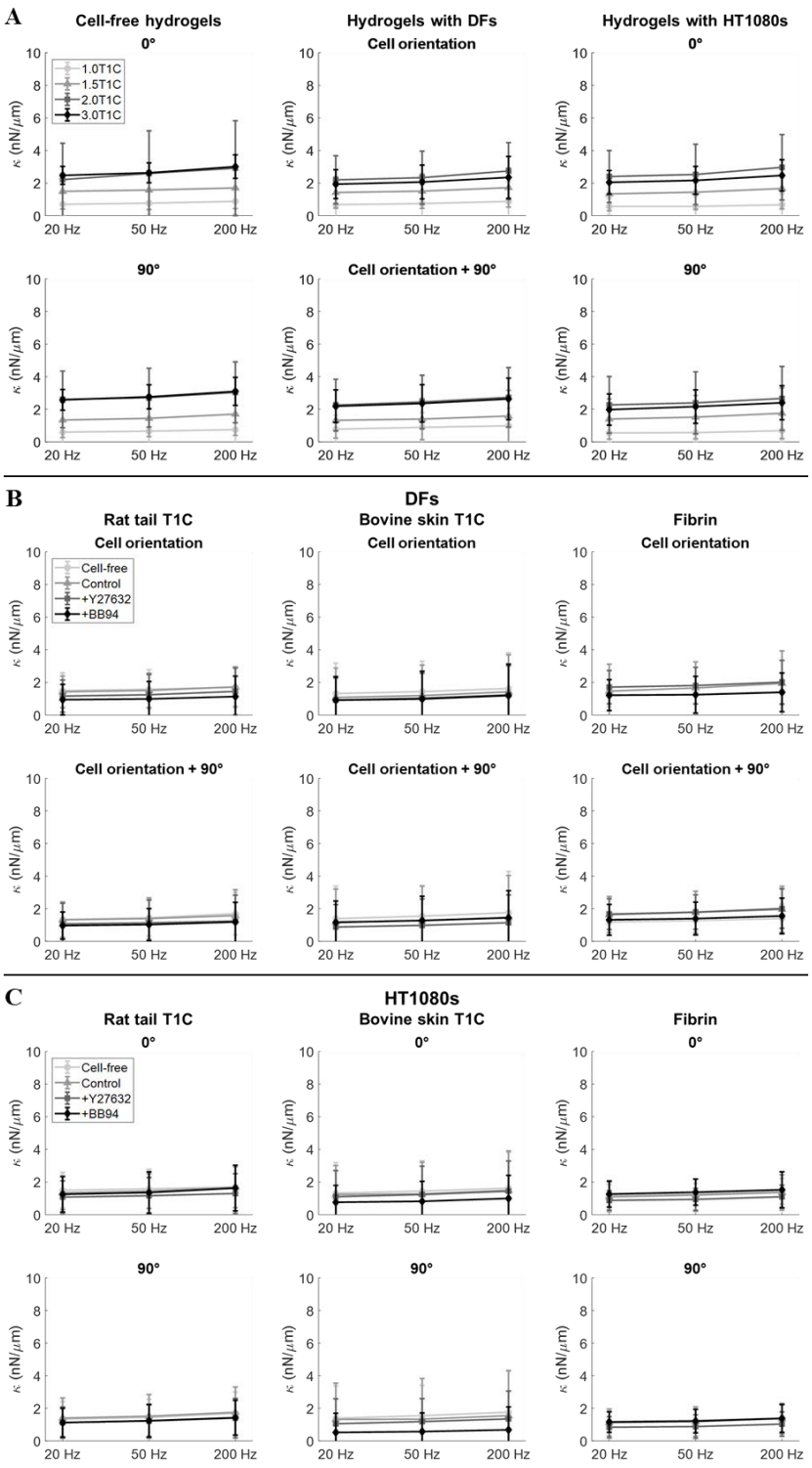

Suppl. Figure 3.4. Stiffness κ measured at different frequencies of bead oscillation (median ± IQR). κ was probed along and across the long axis of the cell (for DF cells) or along horizontal and vertical axis of the image (for HT1080s and cell-free hydrogels). Median κ values for (A) rat tail T1C hydrogels polymerized at different concentrations and probed around (B) DFs and (C) HT1080s cultured in 3 different types of hydrogels (rat tail T1C, bovine skin T1C, fibrin), untreated or treated with Y27632 or BB94.

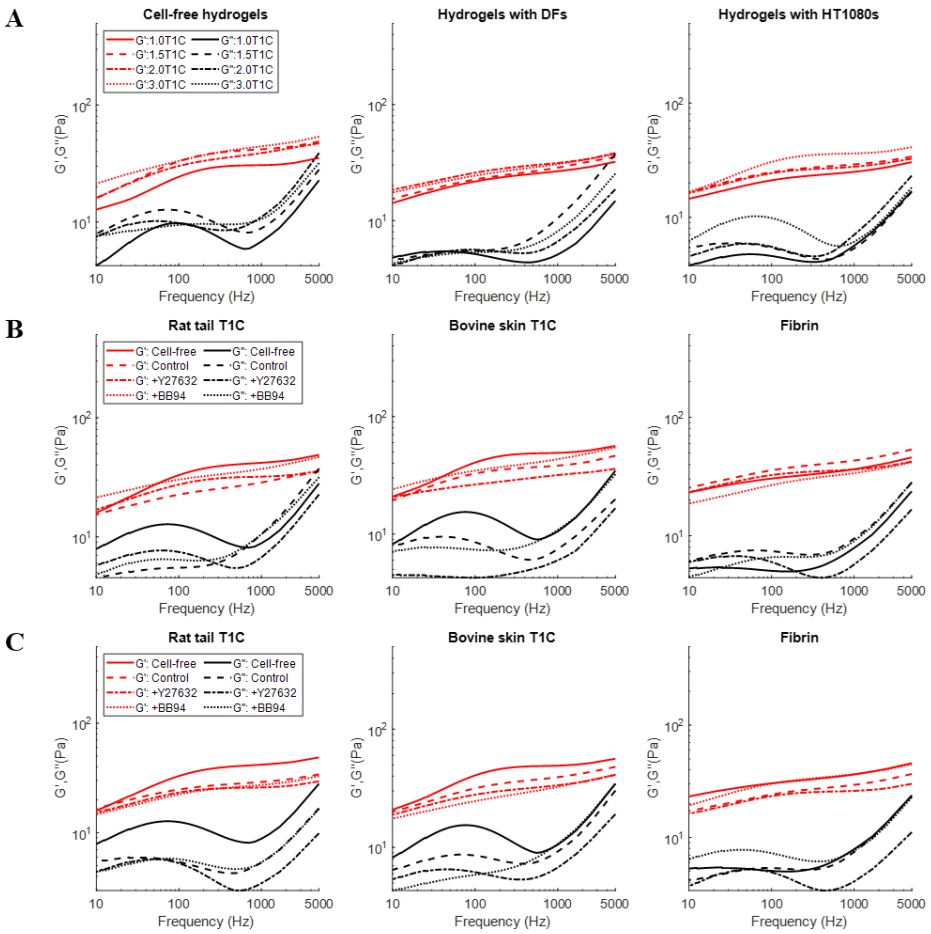

Suppl. Figure 3.5. *G'* and *G''* values calculated from passive microrheology data (detection beam only). Change in *G'* and *G''* with frequency inside (A) rat tail T1C hydrogels polymerized at different concentrations and probed around (B) DFs and (C) HT1080s cultured in 3 different types of hydrogels (rat tail T1C, bovine skin T1C, fibrin), untreated or treated with Y27632 or BB94.

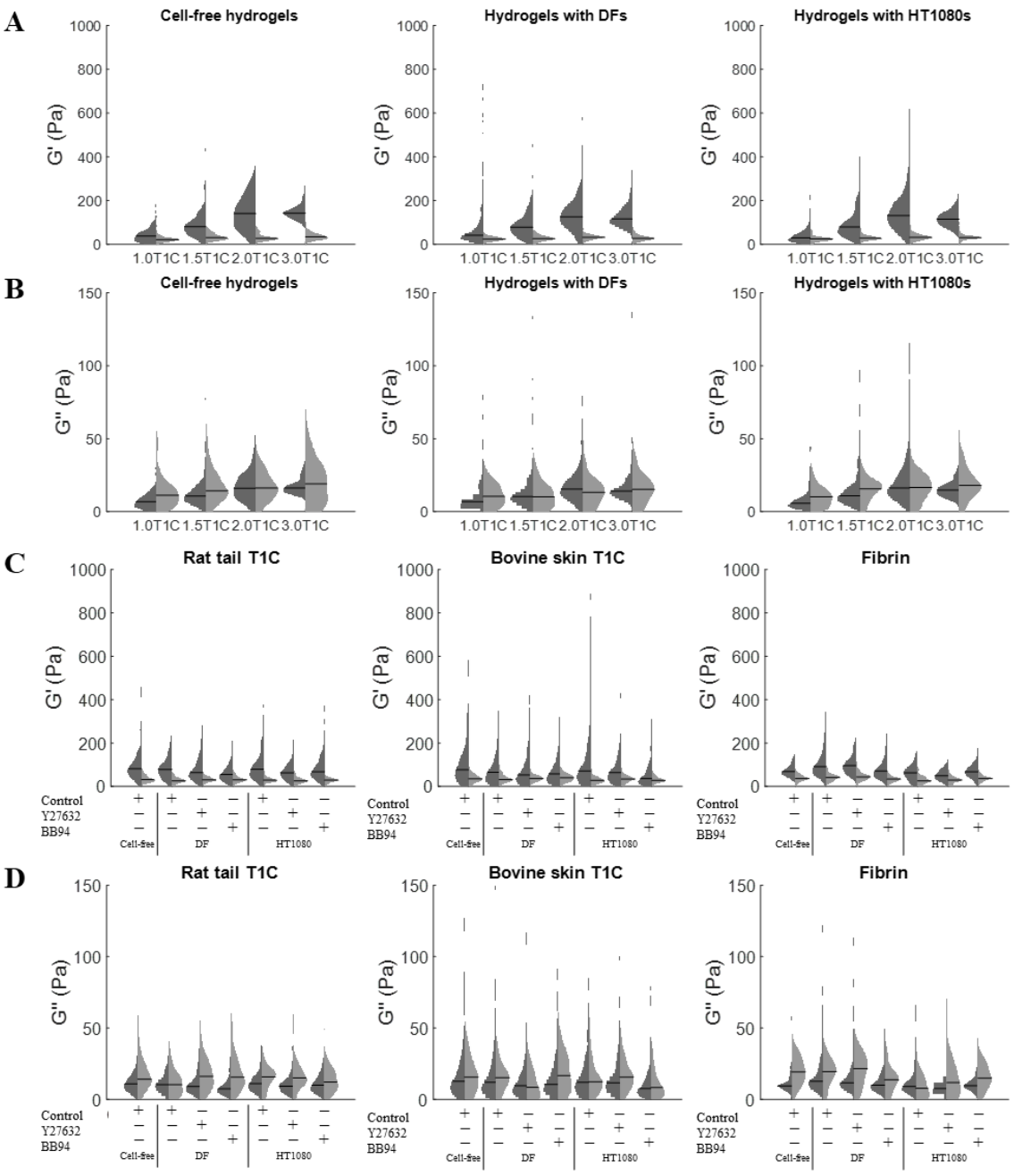

Suppl. Figure 3.6. Comparison of *G'* and *G"* values measured using active (dark grey) and passive (light grey) microrheology. (A) *G'* and (B) *G"* distributions for rat tail T1C hydrogels polymerized at different concentrations. (C) *G'* and (D) *G"* distributions for 3 different types of hydrogels (rat tail T1C, bovine skin T1C, fibrin).

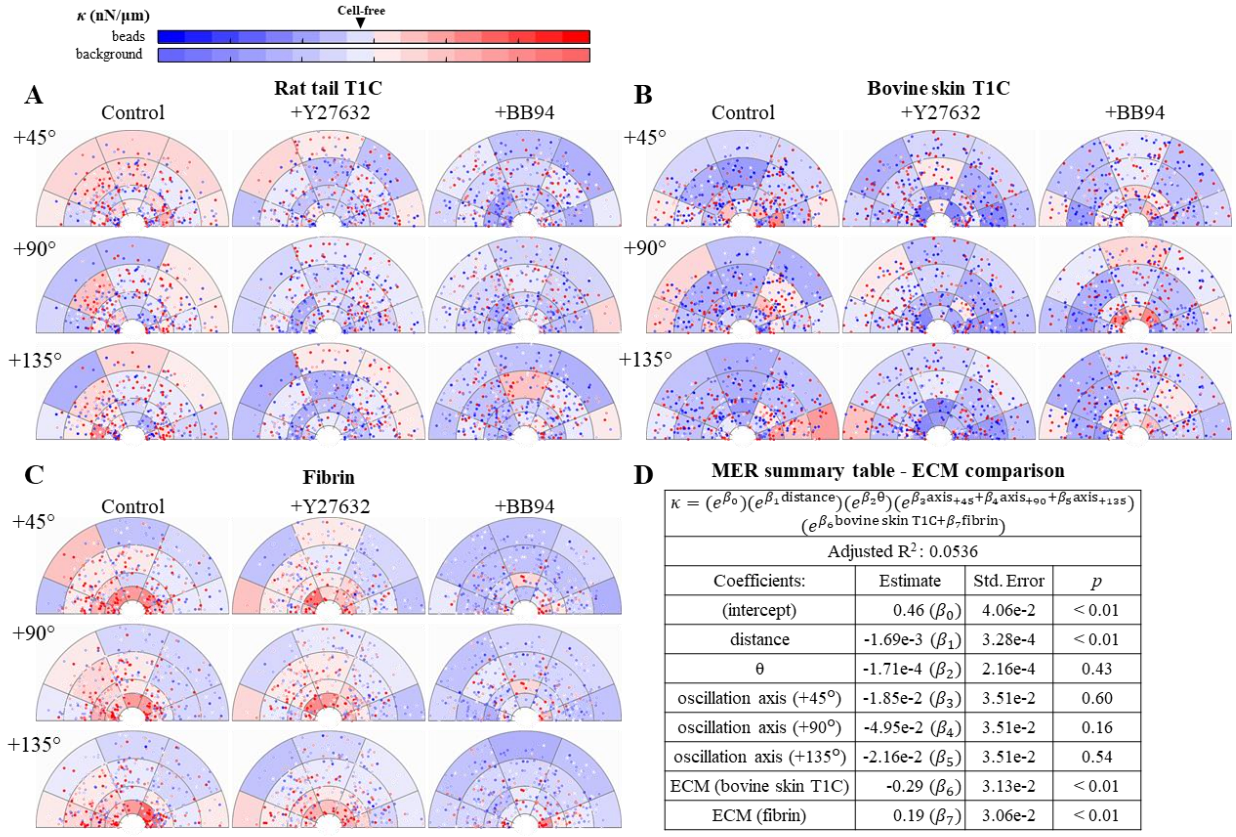

D MER summary table - ECM comparison

$\kappa = (e^{\beta_0})(e^{\beta_1 \text{distance}})(e^{\beta_2 \theta})(e^{\beta_3 \text{axis}_{+45} + \beta_4 \text{axis}_{+90} + \beta_5 \text{axis}_{+135}})(e^{\beta_6 \text{bovine skin T1C} + \beta_7 \text{fibrin}})$

Adjusted R^2: 0.0536

Coefficients:	Estimate	Std. Error	p
(intercept)	0.46 (β_0)	4.06e-2	< 0.01
distance	-1.69e-3 (β_1)	3.28e-4	< 0.01
θ	-1.71e-4 (β_2)	2.16e-4	0.43
oscillation axis (+45°)	-1.85e-2 (β_3)	3.51e-2	0.60
oscillation axis (+90°)	-4.95e-2 (β_4)	3.51e-2	0.16
oscillation axis (+135°)	-2.16e-2 (β_5)	3.51e-2	0.54
ECM (bovine skin T1C)	-0.29 (β_6)	3.13e-2	< 0.01
ECM (fibrin)	0.19 (β_7)	3.06e-2	< 0.01

E MER summary table - treatment comparison

$\kappa = (e^{\beta_0})(e^{\beta_1 \text{distance}})(e^{\beta_2 \theta})(e^{\beta_3 \text{axis}_{+45} + \beta_4 \text{axis}_{+90} + \beta_5 \text{axis}_{+135}})(e^{\beta_6 \text{Y27632} + \beta_7 \text{BB94}})$

	Rat tail T1C			Bovine skin T1C			Fibrin		
	Adjusted R^2: 0.0152			Adjusted R^2: 0.0002			Adjusted R^2: 0.1150		
Coefficients:	Estimate	Std. Error	p	Estimate	Std. Error	p	Estimate	Std. Error	p
(intercept)	0.33 (β_0)	3.55e-2	< 0.01	6.28e-2 (β_0)	5.74e-2	0.27	0.71 (β_0)	2.42e-2	< 0.01
distance	7.43e-4 (β_1)	2.82e-4	0.01	-3.98e-4 (β_1)	4.12e-4	0.33	-3.54e-3 (β_1)	1.82e-4	< 0.01
θ	-2.47e-4 (β_2)	1.94e-4	0.20	-1.18e-4 (β_2)	3.05e-4	0.70	3.31e-4 (β_2)	1.27e-4	0.01
oscillation axis (+45°)	-1.13e-3 (β_3)	3.05e-2	0.97	-2.91e-2 (β_3)	4.83e-2	0.55	3.49e-3 (β_3)	2.03e-2	0.86
oscillation axis (+90°)	-2.76e-2 (β_4)	3.05e-2	0.37	4.17e-4 (β_4)	4.83e-2	0.99	6.23e-3 (β_4)	2.03e-2	0.76
oscillation axis (+135°)	-1.68e-2 (β_5)	3.05e-2	0.58	2.69e-2 (β_5)	4.83e-2	0.58	1.25e-3 (β_5)	2.03e-2	0.95
treatment (Y27632)	-0.18 (β_6)	2.71e-2	< 0.01	-6.86e-2 (β_6)	4.16e-2	0.10	-8.01e-2 (β_6)	1.74e-2	< 0.01
treatment (BB94)	-0.23 (β_7)	2.68e-2	< 0.01	2.99e-2 (β_7)	4.20e-2	0.48	-0.28 (β_7)	1.76e-2	< 0.01

Suppl. Figure 3.7. Supplementary material to Figure 3.2D. Stiffness κ distribution around DFs probed at +45°, +90° and +135° with respect to the long axis of the cell. Data shown for DFs cultured in (A) rat tail T1C, (B) bovine skin T1C, and (C) fibrin. MER summary table describing significant predictors of stiffness probed around DFs cultured in the 3 different types of hydrogels (D) and treated with Y27632 or BB94 (E). Discrete variables of oscillation axis, ECM and treatment were simply encoded with the reference to cell orientation angle, rat tail T1C and control condition, respectively.

Suppl. Table 3.1. Supplementary table to (A) Figure 3.3B, (B) Figure 3.3C and (C) Figure 3.3D. Shown are the *p*-statistics using the Tukey-Kramer test.

A — **Nuclear/Cytoplasmic YAP ratio**

		Rat tail T1C			Bovine skin T1C			Fibrin		
		Control	+Y27632	+BB94	Control	+Y27632	+BB94	Control	+Y27632	+BB94
Rat tail T1C	Control		0.23	0.95	> 0.99	0.98	> 0.99	> 0.99	> 0.99	> 0.99
	+Y27632			0.01	0.19	0.01	0.34	0.54	0.61	0.72
	+BB94				0.97	> 0.99	0.88	0.72	0.66	0.54
Bovine skin T1C	Control					0.99	> 0.99	> 0.99	> 0.99	> 0.99
	+Y27632						0.95	0.85	0.8	0.7
	+BB94							> 0.99	> 0.99	> 0.99
Fibrin	Control								> 0.99	> 0.99
	+Y27632									> 0.99
	+BB94									

B — **% of fibronectin outside of the cell**

		Rat tail T1C			Bovine skin T1C			Fibrin		
		Control	+Y27632	+BB94	Control	+Y27632	+BB94	Control	+Y27632	+BB94
Rat tail T1C	Control		0.53	< 0.01	0.27	0.05	< 0.01	< 0.01	< 0.01	< 0.01
	+Y27632			< 0.01	> 0.99	0.97	0.19	< 0.01	< 0.01	< 0.01
	+BB94				< 0.01	0.01	0.47	0.02	0.25	0.98
Bovine skin T1C	Control					> 0.99	0.44	< 0.01	< 0.01	< 0.01
	+Y27632						0.87	< 0.01	< 0.01	< 0.01
	+BB94							< 0.01	< 0.01	0.03
Fibrin	Control								0.99	0.26
	+Y27632									0.87
	+BB94									

C — **Solidity**

		Rat tail T1C			Bovine skin T1C			Fibrin		
		Control	+Y27632	+BB94	Control	+Y27632	+BB94	Control	+Y27632	+BB94
Rat tail T1C	Control		0.38	< 0.01	0.13	0.88	0.01	> 0.99	> 0.99	> 0.99
	+Y27632			0.77	> 0.99	0.01	0.87	0.57	0.68	0.14
	+BB94				0.97	< 0.01	> 0.99	0.01	0.02	< 0.01
Bovine skin T1C	Control					< 0.01	0.99	0.24	0.33	0.03
	+Y27632						< 0.01	0.73	0.63	0.99
	+BB94							0.02	0.03	< 0.01
Fibrin	Control								> 0.99	> 0.99
	+Y27632									0.99
	+BB94									

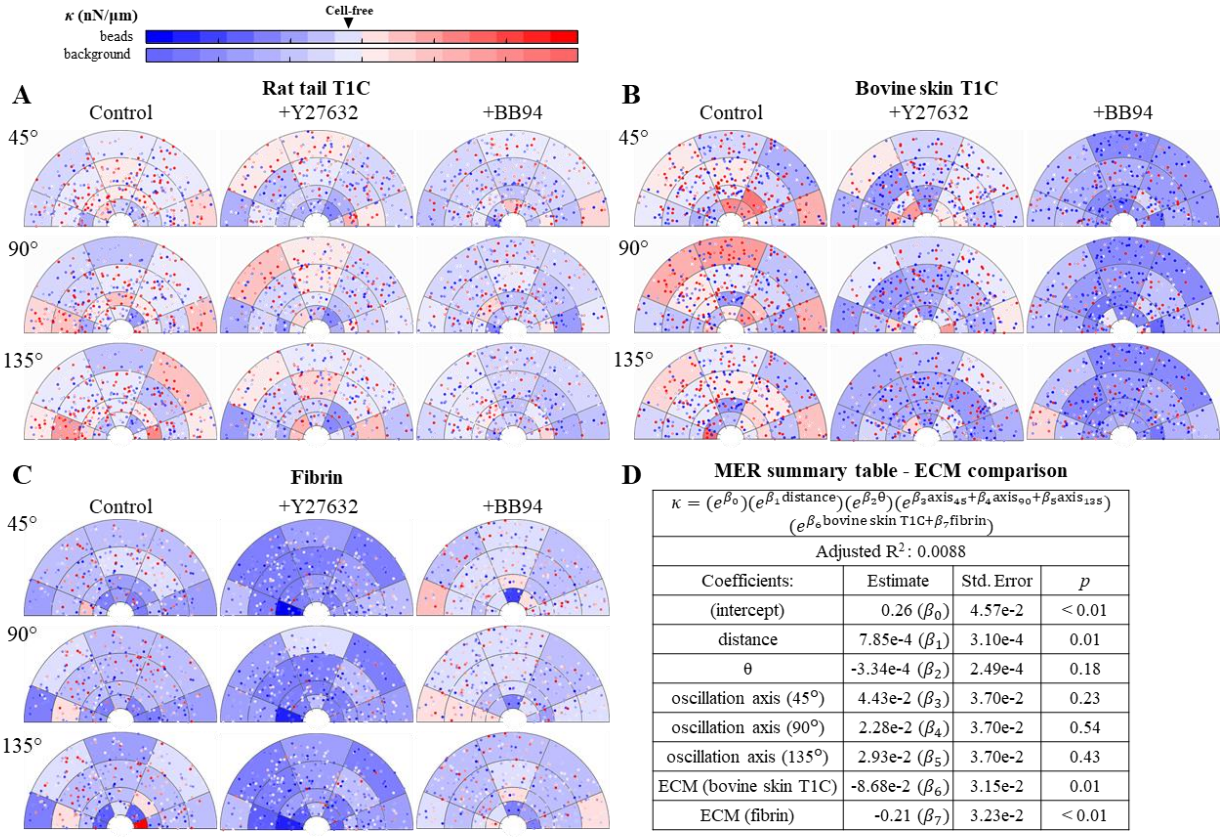

D **MER summary table - ECM comparison**

$\kappa = (e^{\beta_0})(e^{\beta_1 \text{distance}})(e^{\beta_2 \theta})(e^{\beta_3 \text{axis}_{45} + \beta_4 \text{axis}_{90} + \beta_5 \text{axis}_{135}})(e^{\beta_6 \text{bovine skin T1C} + \beta_7 \text{fibrin}})$

Adjusted R^2: 0.0088

Coefficients:	Estimate	Std. Error	p
(intercept)	0.26 (β_0)	4.57e-2	< 0.01
distance	7.85e-4 (β_1)	3.10e-4	0.01
θ	-3.34e-4 (β_2)	2.49e-4	0.18
oscillation axis (45°)	4.43e-2 (β_3)	3.70e-2	0.23
oscillation axis (90°)	2.28e-2 (β_4)	3.70e-2	0.54
oscillation axis (135°)	2.93e-2 (β_5)	3.70e-2	0.43
ECM (bovine skin T1C)	-8.68e-2 (β_6)	3.15e-2	0.01
ECM (fibrin)	-0.21 (β_7)	3.23e-2	< 0.01

E **MER summary table - treatment comparison**

$\kappa = (e^{\beta_0})(e^{\beta_1 \text{distance}})(e^{\beta_2 \theta})(e^{\beta_3 \text{axis}_{45} + \beta_4 \text{axis}_{90} + \beta_5 \text{axis}_{135}})(e^{\beta_6 \text{Y27632} + \beta_7 \text{BB94}})$

	Rat tail T1C			Bovine skin T1C			Fibrin		
	Adjusted R^2: 0.0081			Adjusted R^2: 0.0434			Adjusted R^2: 0.0569		
Coefficients:	Estimate	Std. Error	p	Estimate	Std. Error	p	Estimate	Std. Error	p
(intercept)	0.24 (β_0)	3.50e-2	< 0.01	0.32 (β_0)	6.69e-2	< 0.01	7.67e-3 (β_0)	3.58e-2	0.83
distance	3.14e-4 (β_1)	2.22e-4	0.16	4.84e-4 (β_1)	4.21e-4	0.91	1.92e-3 (β_1)	2.34e-4	< 0.01
θ	3.52e-4 (β_2)	1.94e-4	0.07	-6.27e-4 (β_2)	3.53e-4	0.08	-6.66e-4 (β_2)	1.93e-4	< 0.01
oscillation axis (45°)	2.40e-2 (β_3)	2.81e-2	0.39	-3.20e-2 (β_3)	5.13e-2	0.53	1.34e-2 (β_3)	2.81e-2	0.63
oscillation axis (90°)	1.76e-2 (β_4)	2.81e-2	0.53	-6.22e-2 (β_4)	5.13e-2	0.23	-1.22e-2 (β_4)	2.81e-2	0.66
oscillation axis (135°)	2.18e-2 (β_5)	2.81e-2	0.44	-5.19e-2 (β_5)	5.13e-2	0.31	-3.29e-3 (β_5)	2.81e-2	0.91
treatment (Y27632)	-0.13 (β_6)	2.47e-2	< 0.01	-0.33 (β_6)	4.41e-2	< 0.01	-0.24 (β_6)	2.46e-2	< 0.01
treatment (BB94)	-0.15 (β_7)	2.44e-2	< 0.01	-0.64 (β_7)	4.47e-2	< 0.01	6.14e-2 (β_7)	2.47e-2	0.01

Suppl. Figure 3.8. Supplementary material to Figure 3.4B. Stiffness κ distribution around HT1080s probed at 45°, 90° and 135° with respect to the horizontal axis of the image. Data shown for HT1080s cultured in (A) rat tail T1C, (B) bovine skin T1C, and (C) fibrin. MER summary table describing significant predictors of stiffness probed around HT1080s cultured in the 3 different types of hydrogels (D) and treated with Y27632 or BB94 (E). Discrete variables of oscillation axis, ECM and treatment were simply encoded with the reference to horizontal axis of the image, rat tail T1C and control condition, respectively.

Suppl. Table 3.2. Supplementary table to (A) Figure 3.5B, (B) Figure 3.5C and (C) Figure 3.5D. Shown are the *p*-statistics using the Tukey-Kramer test.

A — Nuclear/Cytoplasmic YAP ratio

		Rat tail T1C			Bovine skin T1C			Fibrin		
		Control	+Y27632	+BB94	Control	+Y27632	+BB94	Control	+Y27632	+BB94
Rat tail T1C	Control		< 0.01	0.04	> 0.99	> 0.99	0.32	0.94	< 0.01	> 0.99
	+Y27632			0.02	< 0.01	< 0.01	< 0.01	< 0.01	0.99	< 0.01
	+BB94				0.03	0.12	> 0.99	< 0.01	0.24	0.21
Bovine skin T1C	Control					> 0.99	0.27	0.95	< 0.01	> 0.99
	+Y27632						0.58	0.76	< 0.01	> 0.99
	+BB94							0.01	0.02	0.74
Fibrin	Control								< 0.01	0.61
	+Y27632									< 0.01
	+BB94									

B — % of fibronectin outside of the cell

		Rat tail T1C			Bovine skin T1C			Fibrin		
		Control	+Y27632	+BB94	Control	+Y27632	+BB94	Control	+Y27632	+BB94
Rat tail T1C	Control		0.01	0.84	0.06	> 0.99	0.79	< 0.01	< 0.01	< 0.01
	+Y27632			< 0.01	< 0.01	0.03	< 0.01	0.99	0.75	0.89
	+BB94				0.85	0.51	> 0.99	< 0.01	< 0.01	< 0.01
Bovine skin T1C	Control					0.01	0.93	< 0.01	< 0.01	< 0.01
	+Y27632						0.46	< 0.01	< 0.01	< 0.01
	+BB94							< 0.01	< 0.01	< 0.01
Fibrin	Control								> 0.99	> 0.99
	+Y27632									> 0.99
	+BB94									

C — Circularity

		Rat tail T1C			Bovine skin T1C			Fibrin		
		Control	+Y27632	+BB94	Control	+Y27632	+BB94	Control	+Y27632	+BB94
Rat tail T1C	Control		< 0.01	< 0.01	> 0.99	0.01	< 0.01	< 0.01	< 0.01	0.1
	+Y27632			0.07	< 0.01	0.04	0.15	< 0.01	0.08	< 0.01
	+BB94				0.01	> 0.99	> 0.99	< 0.01	> 0.99	< 0.01
Bovine skin T1C	Control					0.01	< 0.01	< 0.01	< 0.01	0.08
	+Y27632						> 0.99	< 0.01	> 0.99	< 0.01
	+BB94							< 0.01	> 0.99	< 0.01
Fibrin	Control								< 0.01	0.97
	+Y27632									< 0.01
	+BB94									

3.8. References

1. Mouw, J. K., Ou, G. & Weaver, V. M. Extracellular matrix assembly : a multiscale deconstruction. *Nat. Rev. Mol. Cell Biol.* **15**, 771–85 (2014).

2. Frantz, C. *et al.* The extracellular matrix at a glance. *J. Cell Sci.* **123**, 4195–4200 (2010).

3. Lu, P., Takai, K., Weaver, V. M. & Werb, Z. Extracellular Matrix Degradation and Remodeling in Development and Disease. *Cold Spring Harb Perspect Biol* **3**, 1–24 (2011).

4. Humphrey, J. D., Dufresne, E. R. & Schwartz, M. A. Mechanotransduction and extracellular matrix homeostasis. *Nat. Rev. Mol. Cell Biol.* **15**, 802–812 (2014).

5. Daley, W. P., Peters, S. B. & Larsen, M. Extracellular matrix dynamics in development and

regenerative medicine. *J. Cell Sci.* **121**, 255–264 (2008).

6. Ehrbar, M. *et al.* Elucidating the role of matrix stiffness in 3D cell migration and remodeling. *Biophys. J.* **100**, 284–293 (2011).

7. Gkretsi, V. & Stylianopoulos, T. Cell Adhesion and Matrix Stiffness : Coordinating Cancer Cell invasion and Metastasis. *Front. Oncol.* **8**, 1–7 (2018).

8. Smith, L. R., Cho, S. & Discher, D. E. Stem cell differentiation is regulated by extracellular matrix mechanics. *Physiology* **33**, 16–25 (2018).

9. Najafi, M., Farhood, B. & Mortezaee, K. Extracellular matrix (ECM) stiffness and degradation as cancer drivers. *J. Cell. Biochem.* **120**, 2782–2790 (2019).

10. Keating, M., Kurup, A., Alvarez-Elizondo, M., Levine, A. J. & Botvinick, E. Spatial distributions of pericellular stiffness in natural extracellular matrices are dependent on cell-mediated proteolysis and contractility. *Acta Biomater.* **57**, 304–312 (2017).

11. Jagiełło, A., Lim, M. & Botvinick, E. Dermal fibroblasts and triple-negative mammary epithelial cancer cells differentially stiffen their local matrix. *APL Bioeng.* **4**, 1–12 (2020).

12. Antoine, E. E., Vlachos, P. P. & Rylander, M. N. Review of Collagen I Hydrogels for Bioengineered Tissue Microenvironments : Characterization of Mechanics , Structure , and Transport. *Tissue Eng Part B Rev.* **20**, 683–696 (2014).

13. Davison-Kotler, E., Marshall, W. S. & García-Gareta, E. Sources of collagen for biomaterials in skin wound healing. *Bioengineering* **6**, 1–15 (2019).

14. Tronci, G. The application of collagen in advanced wound dressings. in *Advanced Textiles for Wound Care* 363–389 (2019). doi:10.1016/b978-0-08-102192-7.00013-8

15. Moreno-Arotzena, O., Meier, J., del Amo, C. & García-Aznar, J. Characterization of Fibrin and Collagen Gels for Engineering Wound Healing Models. *Materials (Basel).* **8**, 1636–1651 (2015).

16. Hong, H. & Stegemann, J. P. 2D and 3D collagen and fibrin biopolymers promote specific ECM and integrin gene expression by vascular smooth muscle cells. *J. Biomater. Sci. Polym. Ed.* **19**, 1279–1293 (2008).

17. Kumar, N. & Al Sabti, K. Fibrin glue in ophthalmology. *Indian J. Ophthalmol.* **57**, 371–379 (2010).

18. Bhat, Y. M. *et al.* Tissue adhesives: Cyanoacrylate glue and fibrin sealant. *Gastrointest. Endosc.* **78**, 209–215 (2013).

19. Spotnitz, W. D. Fibrin Sealant: The Only Approved Hemostat, Sealant, and Adhesive—a Laboratory and Clinical Perspective. *ISRN Surg.* **2014**, 1–28 (2014).

20. Lai, V. K. *et al.* Microstructural and mechanical differences between digested collagen – fibrin co-gels and pure collagen and fibrin gels. *Acta Biomater.* **8**, 4031–4042 (2012).

21. Wolf, K. *et al.* Physical limits of cell migration: Control by ECM space and nuclear deformation and tuning by proteolysis and traction force. *J. Cell Biol.* **201**, 1069–1084 (2013).

22. Gaggioli, C. *et al.* Fibroblast-led collective invasion of carcinoma cells with differing roles for RhoGTPases in leading and following cells. *Nat. Cell Biol.* **9**, 1392–1400 (2007).

23. Yamamoto, M. *et al.* A selective inhibitor of the rho kinase pathway, y-27632, and its influence on wound healing in the corneal stroma. *Mol. Vis.* **18**, 1727–1739 (2012).

24. Ibrahim, D. G., Ko, J. A., Iwata, W., Okumichi, H. & Kiuchi, Y. An in vitro study of scarring formation mediated by human Tenon fibroblasts: Effect of Y-27632, a Rho kinase inhibitor. *Cell Biochem. Funct.* **37**, 113–124 (2019).

25. Nath, D. *et al.* Meltrin γ (ADAM-9) mediates cellular adhesion through α6β1 integrin, leading to a marked induction of fibroblast cell motility. *J. Cell Sci.* **113**, 2319–2328 (2000).

26. Schwartz, M. P. *et al.* A quantitative comparison of human HT-1080 fibrosarcoma cells and primary human dermal fibroblasts identifies a 3D migration mechanism with properties unique to the transformed phenotype. *PLoS One* **8**, 1–24 (2013).

27. Carragher, N. O. *et al.* Calpain 2 and Src dependence distinguishes mesenchymal and amoeboid modes of tumour cell invasion: A link to integrin function. *Oncogene* **25**, 5726–5740 (2006).

28. Niggli, V., Schmid, M. & Nievergelt, A. Differential roles of Rho-kinase and myosin light chain kinase in regulating shape, adhesion, and migration of HT1080 fibrosarcoma cells. *Biochem. Biophys. Res. Commun.* **343**, 602–608 (2006).

29. Botos, I., Scapozza, L., Zhang, D., Liotrat, L. a & Meyer, E. F. Batimastat, a potent matrix metalloproteinase inhibitor, exhibits an unexpected mode of binding. *Proc. Natl. Acad. Sci.* **93**, 2749–2754 (1996).

30. Low, J. A., Johnson, M. D., Bone, E. A. & Dickson, R. B. The matrix metalloproteinase inhibitor batimastat (BB-94) retards human breast cancer solid tumor growth but not ascites formation in nude mice. *Clin. Cancer Res.* **2**, 1207–1214 (1996).

31. Sabeh, F. *et al.* Tumor cell traffic through the extracellular matrix is controlled by the membrane-anchored collagenase MT1-MMP. *J. Cell Biol.* **167**, 769–781 (2004).

32. Doyle, A. D. Generation of 3D collagen gels with controlled, diverse architectures. *Curr Protoc Cell Biol.* **72**, 1–22 (2016).

33. Jagiełło, A., Hu, Q., Castillo, U. & Botvinick, E. Patterned photocrosslinking to establish stiffness anisotropies in fibrous 3D hydrogels. *Acta Biomater.* (2021). doi:10.1016/j.actbio.2021.12.028

34. Keating, M., Lim, M., Hu, Q. & Botvinick, E. Selective stiffening of fibrin hydrogels with micron resolution via photocrosslinking. *Acta Biomater.* **87**, 88–96 (2019).

35. Legland, D., Arganda-carreras, I., Andrey, P., Biopolymers, U. R. & Bourgin, I. J. MorphoLibJ : integrated library and plugins for mathematical morphology with ImageJ. *Bioinformatics* **32**, 3532–3534 (2016).

36. Schindelin, J. *et al.* Fiji: An open-source platform for biological-image analysis. *Nat. Methods* **9**, 676–682 (2012).

37. Mizuno, D., Head, D. A., MacKintosh, F. C. & Schmidt, C. F. Active and passive microrheology in equilibrium and nonequilibrium systems. *Macromolecules* **41**, 7194–7202 (2008).

38. Mizuno, D., Tardin, C., Schmidt, C. F. & MacKintosh, F. C. Nonequilibrium Mechanics of Active Cytoskeletal Networks. *Science.* **315**, 370–373 (2007).

39. Allersma, M. W., Gittes, F., DeCastro, M. J., Stewart, R. J. & Schmidt, C. F. Two-Dimensional Tracking of ncd Motility by Back Focal Plane Interferometry. *Biophys. J.* **74**, 1074–1085 (1998).

40. Staunton, J. R. *et al.* Mechanical Properties of the Tumor Stromal Microenvironment Probed In Vitro and Ex Vivo by In Situ-Calibrated Optical Trap-Based Active Microrheology. *Cell. Mol. Bioeng.* **9**,

398–417 (2016).

41. Blehm, B. H., Devine, A., Staunton, J. R. & Tanner, K. In vivo tissue has non-linear rheological behavior distinct from 3D biomimetic hydrogels, as determined by AMOTIV microscopy. *Biomaterials* **83**, 66–78 (2016).

42. Thrivikraman, G. *et al.* Cell contact guidance via sensing anisotropy of network mechanical resistance. *PNAS* **118**, 1–11 (2021).

43. Pelletier, V., Gal, N., Fournier, P. & Kilfoil, M. L. Microrheology of microtubule solutions and actin-microtubule composite networks. *Phys. Rev. Lett.* **102**, 100–103 (2009).

44. Lobo, J., See, E. Y. S., Biggs, M. & Pandit, A. An insight into morphometric descriptors of cell shape that pertain to regenerative medicine. *J. Tissue Eng. Regen. Med.* **10**, 539–553 (2016).

45. Wilkinson, G. N. & Rogers, C. E. Symbolic Description of Factorial Models for Analysis of Variance. *J. R. Stat. Soc. Ser. C (Applied Stat.* **22**, 392–399 (1973).

46. Team, R. C. R: A language and environment for statistical computing. R Foundation for Statistical Computing, Vienna, Austria. (2008). Available at: https://www.r-project.org/.

47. Shinsato, Y., Doyle, A. D., Li, W. & Yamada, K. M. Direct comparison of five different 3D extracellular matrix model systems for characterization of cancer cell migration. *Cancer Rep.* **3**, 1–11 (2020).

48. Shayegan, M. & Forde, N. R. Microrheological Characterization of Collagen Systems : From Molecular Solutions to Fibrillar Gels. *PLoS One* **8**, 23–28 (2013).

49. Nijenhuis, N., Mizuno, D., Spaan, J. A. E. & Schmidt, C. F. High-resolution microrheology in the pericellular matrix of prostate cancer cells. *J. R. Soc. Interface* **9**, 1733–1744 (2012).

50. Crocker, J. C. & Hoffman, B. D. Multiple-Particle Tracking and Two-Point Microrheology in Cells. *Methods Cell Biol.* **83**, 141–178 (2007).

51. Pokki, J., Zisi, I., Schulman, E., Indana, D. & Chaudhuri, O. Magnetic probe-based microrheology reveals local softening and stiffening of 3D collagen matrices by fibroblasts. *Biomed. Microdevices* **23**, 1–14 (2021).

52. Duong, H., Wu, B. & Tawil, B. Modulation of 3D fibrin matrix stiffness by intrinsic fibrinogen-thrombin compositions and by extrinsic cellular activity. *Tissue Eng. - Part A* **15**, 1865–1876 (2009).

53. Doyle, A. D., Carvajal, N., Jin, A., Matsumoto, K. & Yamada, K. M. Local 3D matrix microenvironment regulates cell migration through spatiotemporal dynamics of contractility-dependent adhesions. *Nat. Commun.* **6**, 1–15 (2015).

54. Solon, J., Levental, I., Sengupta, K., Georges, P. C. & Janmey, P. A. Fibroblast adaptation and stiffness matching to soft elastic substrates. *Biophys. J.* **93**, 4453–4461 (2007).

55. Tong, M. H., Huang, N., Ngan, A. H. W., Du, Y. & Chan, B. P. Preferential sensing and response to microenvironment stiffness of human dermal fibroblast cultured on protein micropatterns fabricated by 3D multiphoton biofabrication. *Sci. Rep.* **7**, 1–12 (2017).

56. Schwager, S. C. *et al.* Matrix stiffness regulates microvesicle-induced fibroblast activation. *Am. J. Physiol. - Cell Physiol.* **317**, C82–C92 (2019).

57. Lien, S. M., Ko, L. Y. & Huang, T. J. Effect of pore size on ECM secretion and cell growth in gelatin scaffold for articular cartilage tissue engineering. *Acta Biomater.* **5**, 670–679 (2009).

58. Mandal, B. B. & Kundu, S. C. Cell proliferation and migration in silk fibroin 3D scaffolds. *Biomaterials* **30**, 2956–2965 (2009).

59. Annabi, N. *et al.* Controlling the porosity and microarchitecture of hydrogels for tissue engineering. *Tissue Eng. - Part B Rev.* **16**, 371–383 (2010).

60. Kular, J. K., Basu, S. & Sharma, R. I. The extracellular matrix : Structure , composition , age-related differences , tools for analysis and applications for tissue engineering. *J. Tissue Eng.* **5**, 1–17 (2014).

61. Kim, S. H., Turnbull, J. & Guimond, S. Extracellular matrix and cell signalling: The dynamic cooperation of integrin, proteoglycan and growth factor receptor. *J. Endocrinol.* **209**, 139–151 (2011).

62. Coradin, T., Wang, K., Thalie, L. & Trichet, L. Type I Collagen-Fibrin Mixed Hydrogels : Preparation, Properties and Biomedical Applications. *Gels* **6**, (2020).

63. Higuchi, T., Nakamura, T., Kakutani, H. & Ishii, H. Thrombomodulin suppresses invasiveness of HT1080 tumor cells by reducing plasminogen activation on the cell surface through activation of thrombin-activatable fibrinolysis inhibitor. *Biol. Pharm. Bull.* **32**, 179–185 (2009).

64. Jones, C. A. R. *et al.* Micromechanics of cellularized biopolymer networks. *Proc. Natl. Acad. Sci. U. S. A.* **112**, E5117–E5122 (2015).

65. Mahmood, N. & Rabbani, S. A. Fibrinolytic system and cancer: Diagnostic and therapeutic applications. *Int. J. Mol. Sci.* **22**, 1–16 (2021).

66. Yaron, J. R., Zhang, L., Guo, Q., Haydel, S. E. & Lucas, A. R. Fibrinolytic Serine Proteases, Therapeutic Serpins and Inflammation: Fire Dancers and Firestorms. *Front. Cardiovasc. Med.* **8**, 1–21 (2021).

67. Lim, Y. T. *et al.* Independent regulation of matrix metalloproteinases and plasminogen activators in human fibrosarcoma cells. *J. Cell. Physiol.* **167**, 333–340 (1996).

68. Gauza-Włodarczyk, M., Kubisz, L. & Włodarczyk, D. Amino acid composition in determination of collagen origin and assessment of physical factors effects. *Int. J. Biol. Macromol.* **104**, 987–991 (2017).

69. Bielajew, B. J., Hu, J. C. & Athanasiou, K. A. Methodology to Quantify Collagen Subtypes and Crosslinks : Application in Minipig Cartilages. *Cartilage* **13**, 1742S-1754S (2021).

70. Sorushanova, A., Skoufos, I., Tzora, A., Mullen, A. M. & Zeugolis, D. I. The influence of animal species, gender and tissue on the structural, biophysical, biochemical and biological properties of collagen sponges. *J. Mater. Sci. Mater. Med.* **32**, 1–12 (2021).

71. Liu, F. *et al.* Mechanosignaling through YAP and TAZ drives fibroblast activation and fibrosis. *Am. J. Physiol. - Lung Cell. Mol. Physiol.* **308**, L344–L357 (2015).

72. Scott, K. E., Fraley, S. I. & Rangamani, P. A spatial model of YAP/TAZ signaling reveals how stiffness, dimensionality, and shape contribute to emergent outcomes. *Proc. Natl. Acad. Sci. U. S. A.* **118**, 1–12 (2021).

73. Cai, X., Wang, K. C. & Meng, Z. Mechanoregulation of YAP and TAZ in Cellular Homeostasis and Disease Progression. *Front. Cell Dev. Biol.* **9**, 1–12 (2021).

74. Das, A., Fischer, R. S., Pan, D. & Waterman, C. M. YAP Nuclear Localization in the Absence of Cell-Cell Contact Is Mediated by a Filamentous Actin-dependent , Myosin II- and Phospho-YAP-independent Pathway during Extracellular Matrix Mechanosensing. *J. Biol. Chem.* **291**, 6096–6110 (2016).

75. Li, S. *et al.* Targeting Mechanics-Induced Fibroblast Activation through CD44-RhoA-YAP Pathway Ameliorates Crystalline Silica-Induced Silicosis. *Theranostics* **9**, 4993–5008 (2019).

76. Lee, J. Y. *et al.* Identification of cell context- dependent YAP-associated proteins reveals β 1 and β 4 integrin mediate YAP translocation independently of cell spreading. *Sci. Rep.* **9**, 1–11 (2019).

77. You, E. *et al.* SPIN90 Depletion and Microtubule Acetylation Mediate Stromal Fibroblast Activation in Breast Cancer Progression. *Cancer Res.* **77**, 4710–4723 (2017).

78. Matera, D. L. *et al.* Microengineered 3D pulmonary interstitial mimetics highlight a critical role for matrix degradation in myofibroblast differentiation. *Sci. Adv.* **6**, 1–14 (2020).

79. Lee, J. Y. *et al.* YAP-independent mechanotransduction drives breast cancer progression. *Nat. Commun.* **10**, 1–9 (2019).

80. Paten, J. A. *et al.* Molecular Interactions between Collagen and Fibronectin: A Reciprocal Relationship that Regulates De Novo Fibrillogenesis. *Chem* **5**, 2126–2145 (2019).

81. Saunders, J. T. & Schwarzbauer, J. E. Fibronectin matrix as a scaffold for procollagen proteinase binding and collagen processing. *Mol. Biol. Cell* **30**, 2218–2226 (2019).

82. Kubow, K. E. *et al.* Mechanical forces regulate the interactions of fibronectin and collagen I in extracellular matrix. *Nat. Commun.* **8026**, 1–11 (2015).

83. Miron-Mendoza, M., Vazquez, D., Garc, N., Ikebe, H. R. & Petroll, W. M. Coupling of Fibrin Reorganization and Fibronectin Patterning by Corneal Fibroblasts in Response to PDGF BB and TGF β 1. *Bioengineering* **7**, 1–18 (2020).

84. Miron-Mendoza, M., Graham, E., Manohar, S. & Petroll, W. M. Fibroblast-fibronectin patterning and network formation in 3D fibrin matrices. *Matrix Biol.* **64**, 69–80 (2017).

85. Oostendorp, C. *et al.* Visualisation of newly synthesised collagen in vitro and in vivo. *Sci. Rep.* **6**, 1–7 (2016).

86. Brenner, K. A., Corbett, S. A. & Schwarzbauer, J. E. Regulation of fibronectin matrix assembly by activated Ras in transformed cells. *Oncogene* **19**, 3156–3163 (2000).

87. Oliver, N., Newby, R. F., Furcht, L. T., Bourgeois, S. & Diego, S. Regulation of Fibronectin Biosynthesis by Glucocorticoids in Human Fibrosarcoma Cells and Normal Fibroblasts. **33**, 287–296 (1983).

88. Lampi, M. C. & Reinhart-king, C. A. Targeting extracellular matrix stiffness to attenuate disease : From molecular mechanisms to clinical trials. *Sci. Transl. Med.* **10**, 1–15 (2018).

Chapter 4: Patterned photocrosslinking to establish stiffness anisotropies in fibrous 3D hydrogels

Alicja Jagiełło[1], Qingda Hu[1,2], Ulysses Castillo[1], Elliot Botvinick[1,2,3,4,5]

[1] Department of Biomedical Engineering, University of California Irvine, Irvine, CA, 92697-2730, United States

[2] Center for Complex Biological Systems, University of California Irvine, Irvine, CA, 92697-2280, United States

[3] Beckman Laser Institute and Medical Clinic, University of California Irvine, Irvine, CA, 92612, United States

[4] Department of Surgery, University of California Irvine, 333 City Boulevard, Suite 700, Orange, CA, 92868, United States

[5] The Edwards Lifesciences Foundation Cardiovascular Innovation and Research Center, University of California Irvine, Irvine, CA, 92697-2730, United States

4.1. Abstract

Cells are known to constantly interact with their local extracellular matrix (ECM) and respond to a variety of biochemical and mechanical cues received from the ECM. Nonetheless, comprehensive understanding of cell-ECM interactions has been elusive. Many studies rely on analysis of cell behavior on 2D substrates, which do not reflect a natural cell environment. Further, lack of dynamic control over local stiffness anisotropies and fiber alignment hinders progress in studies in naturally derived fibrous 3D cultures. Here, we present a cell-safe method of patterned photocrosslinking, which can aid in studying biological hypotheses related to mechanotransduction in 3D hydrogels. As previously described by our group, ruthenium-catalyzed photocrosslinking (RCP) of selected ECM regions promotes localized increase in stiffness mediated by focused blue laser light in a confocal microscope. In this study, we further demonstrate that RCP can induce localized strain stiffening and fiber alignment outside of the selected crosslinked region and induce stiffness anisotropy biased towards the direction of fiber alignment. MDA-MB-231 cells are shown to respond to RCP-induced changes in local ECM architecture and display directional bias towards the direction of fiber alignment, as compared to control cells. Further, the effect of patterned crosslinking on a stiffness landscape is measured using multi-axes optical tweezers active microrheology (AMR) with backscattered laser beam illumination. AMR validates RCP as a suitable tool for creating distinct stiffness anisotropies which promote directed migration of cells, further underscoring the usefulness of RCP in cell-ECM studies.

4.2. Introduction

Cells in the human body reciprocally interact with their local extracellular matrix (ECM). Cells constantly remodel their ECM through synthesis, breakdown, organization, and crosslinking of ECM proteins and dynamic changes in tension of local ECM fibers [1–3]. Reciprocally, cells also respond to a variety of biochemical and mechanical cues from their ECM. For instance, cells can exhibit contact guidance and migrate along the direction of topographical features on 2D substrates or along the fiber orientation in 3D cultures [4–6]. Contact guidance has been reported to play an important role in numerous physiological processes, including morphogenesis, wound healing and cancer metastasis [5,7–9]. Past research indicates that cells display contact guidance by sensing anisotropy in the organization of local ECM fibers [10]. However, cells also respond to stiffness gradients of their local ECM and migrate towards regions of higher stiffness in a phenomenon known as durotaxis. Durotaxis was shown to be exhibited by different cancer cell lines [11] and it has been previously described to affect cell phenotype and promote fibrosis [12,13].

Despite the importance of cell contact guidance and durotaxis in natural cell behavior, a comprehensive understanding of mechanotransduction and cell-ECM interactions during these biological processes has been elusive. Many studies rely on analysis of cell behavior on 2D substrates [8], which do not reflect a natural cell environment and may provide misleading results as compared those observed in 3D with respect to cell-ECM interactions [2,14]. While micropatterning strategies readily used to generate stiffness gradients in 2D systems have been adapted for synthetic hydrogels [15], they are still emerging for naturally-derived fibrous 3D systems [16]. Approaches developed for 3D cultures include cell-induced hydrogel contraction and fiber alignment [17,18], use of polymers with temperature controlled

mechanical properties [19], magnetic alignment of fibrin and collagen fibers [9,10,20,21] or mechanical stretching of hydrogels [22]. All these methods alter fiber alignment and stiffness inside the whole hydrogel, and don't allow the study of individual cell responses to complex changes to their stiffness landscape.

Here, we evaluate a method of patterned photocrosslinking to alter stiffness and fiber alignment and induce directed cell migration at a single cell level. As previously described by our group and others [23–25], the addition of a solution of a ruthenium compound and sodium persulfate promotes fibrin crosslinking in the presence of focused blue laser light in a confocal microscope. Crosslinking of peri-cellular fibrin via ruthenium-catalyzed photocrosslinking (RCP) does not affect cell viability and can precisely be applied to a specified ECM region around an individual cell [23]. Multi-axes optical tweezers active microrheology (AMR) verifies the RCP-induced change in local fiber network stiffness anisotropy. AMR is a non-invasive method of assessing local mechanical properties of a hydrogel. AMR operates by applying optical forces to individual embedded microbeads, and then extracting mechanical properties of the surrounding ECM from the resulting microbead displacements [26]. Past research by our group has shown AMR can be used to measure temporal and spatial changes in ECM-stiffness landscapes around individual cells [27,28] and cell colonies [29]. The optical tweezers are programmed to serially oscillate along six distinct axes passing through the microbead centroid. Bead position is monitored by a detection beam and quadrant photodiode as previously described, and stiffness along each axis is computed from bead displacement and optical force waveforms [27]. Accurate measurements of local stiffness anisotropy with multi-axes AMR aid in describing properties of ECM networks, which were previously shown to be obscured by bulk measurements [27,30].

Past findings reported by our group showed that RCP can promote up to a 25-fold increase in localized ECM stiffness of the crosslinked region as compared to control, with a range of stiffness values corresponding to those naturally established by the cells [23]. Patterned crosslinking was also shown to induce stiffening outside of the crosslinked region, potentially due to strain hardening of the fibers. We postulated that the increase in stiffness outside of the crosslinked region was highly directional and anisotropic. Here, we verify that hypothesis and demonstrate that RCP can be used to create distinct stiffness anisotropies and fiber alignments both inside and outside of the crosslinked region. Furthermore, RCP can induce change in the direction of migration of cells exhibiting contact guidance and durotaxis. Exclusive of the microrheology application presented, this method can be implemented by any investigator with access to a laser scanning confocal microscope.

4.3. Methods

4.3.1. Cell culture

Highly invasive and triple-negative human breast cancer cells, MDA-MB-231 (ATCC), were cultured in Dulbecco's Modified Eagle's Medium (DMEM) with low glucose, L-glutamate, and sodium pyruvate (Gibco) supplemented with 10% Fetal Bovine Serum (FBS, Gibco) and 1% penicillin streptomycin (Gibco).

4.3.2. Hydrogel preparation

Fibrin hydrogels were prepared at 2.3 mg/ml concentration and incubated at 37 °C and 5% CO_2 for 24 h prior to stiffness measurements and imaging. Bovine stock fibrinogen (Sigma, SLBZ1967) was dissolved in phosphate buffered saline (PBS, Gibco), filtered and mixed with 2 μm carboxylated silica microbeads (0.8 mg/ml, Bangs Laboratories). For hydrogels with cells, 15 k/ml of MDA-MB-231 cells was also added to the solution. Following

the addition of bovine thrombin (4 U/ml, Sigma), each solution was polymerized into a 1 ml hydrogel inside of a 35 mm glass bottom dish (MatTek). Hydrogels were incubated for 30 min, and then supplemented with 2 ml of either PBS (cell-free hydrogels) or culture media (hydrogels with cells). On the day of experiments, PBS or culture media was replaced by 2 ml of DMEM with 25 mM HEPES (Gibco), 10% of FBS and 1% penicillin streptomycin.

4.3.3. Selective photocrosslinking

Selective photocrosslinking was conducted as previously described [23]. Briefly, 200 µl of culture media with HEPES was substituted with 200 µl of crosslinker solution prepared by mixing 1.5 mg/mL tris(2,20-bipyridyl) dichlororuthenium (II) hexahydrate (Sigma) and 2.4 mg/mL sodium persulfate (Sigma). Photocrosslinking was conducted at least 30 min after the addition of the crosslinker solution, but no later than 6 h. The region of interest (ROI) chosen for crosslinking was selected using built-in functionality of our Fluoview1200 inverted laser scanning confocal microscope (Olympus) into which the optical tweezers active microrheology optics are integrated. The photocrosslinking was induced by illumination of the selected ROI with the 488 nm laser line (0.1 mW) focused by a high numerical aperture microscope objective lens (60x-oil PlanApo TIRFM 1.45NA, Olympus). A selected ROI was crosslinked at a height of 35 µm from the cover glass at a scanning speed of 2 µs/pixel and a total scan resolution of 1600 pixels x1600 pixels across the 211.2 µm by 211.2 µm field-of-view (FOV). Circular and rectangular ROIs were crosslinked for 2000 and 500 scans, respectively.

4.3.4. Microstructural assessment of fibrin hydrogels

Reflection confocal images obtained with the 559 nm laser line were used to quantify the effect of selective photocrosslinking on fiber alignment and pixel brightness. Image

contrast was normalized before fiber alignment was measured by Ulysses Castillo using the GTFiber software [31]. Pixel brightness of fibers identified by GTFiber software was extracted in MATLAB (The MathWorks Inc.) using custom code. Change in fiber pixel brightness and fiber alignment were calculated in MATLAB by comparing results from images of the same field of view before and after crosslinking.

4.3.5. Active microrheology

Stiffness was measured using our optical tweezers active microrheology system previously described in **Chapter 1.3.1** and in **Chapter 2.3**, but optimized to measure material properties in an arbitrary number of directions. Briefly, stiffness of the ECM is probed by oscillating individual microbeads using optical forces applied by a continuous-wave fiber laser with an emission at 1064 nm (YLR-5–1064-LP, IPG Photonics). Trapping beam oscillations are caused by the movement of a pair of galvanometer mirrors (GVS012, ThorLabs), located conjugate to the back focal plane of the microscope objective lens (60x-oil PlanApo TIRFM 1.45NA, Olympus). A detection laser beam of wavelength 785 nm is generated by a single mode fiber-pigtailed laser diode (LP785-SF100, ThorLabs) and co-aligned with the trapping beam at the center of the bead. Change in bead position and trapping beam position are recorded by two quadrant photodiodes (detQPD and trapQPD, 2901 and 2903, respectively, Newport) and used to calculate a complex material response (α^*) by the relationship X= $\alpha^* F$, where X and F are the Fourier components of bead displacement and optical force, respectively. α^* is computed once for each oscillation direction under the assumption that α^* oscillates purely along that axis. Reported stiffness κ represents the real component of inverse α^*. Each probed bead was located approximately 35 μm from the cover glass and oscillated along 6 different directions (0, 30, 60, 90, 120 and

150° with respect to the horizontal axis of the camera image FOV). The trapping beam was oscillated with an amplitude of 60 nm and frequency of 50 Hz, unless specified otherwise. The proportionality parameter relating detQPD signals to bead displacements was measured *in situ* per bead and per angle of oscillation. Specifically, the sample is mounted in a stage-top nanopositioning piezoelectric stage (P-545.xR8S PInano® XYPiezoSystem,PI). After centering the stage on each bead, the stage is moved 200 nm across the bead with a constant velocity of 100 nm/s. Recorded detQPD voltages are used to quantify the voltage-to-µm conversion factor [32–34], which is later used to calculate bead displacement during AMR measurements. Prior to AMR measurements in fibrin hydrogels, the AMR system is calibrated in water, as previously described [27,28].

4.3.6. Cell tracking experiment

The effect of micropatterned photocrosslinking on migration and orientation of MDA-MB-231 cells was assessed using a Fluoview3000 laser scanning microscope equipped with a 10x-air 0.3 NA microscope objective lens (Olympus). This part of the project was carried out by Qingda Hu. Hydrogels were incubated in a ThermoBox environmental chamber (Tokai Hit) and a stage top incubator (Tokai Hit) with 15% oxygen and 5% CO_2. Photocrosslinking was initiated at least 30 min after the addition of the crosslinking solution to allow for diffusion of the crosslinker solution evenly throughout the hydrogel. Two 1000 µm by 50 µm rectangles separated by 100 µm were selected using built-in functionality of the Fluoview3000 system and crosslinked for 2000 scans using the 488 nm laser line (0.1mW). A selected ROI was crosslinked 100 µm from the cover glass at a scanning speed of 2 µs/pixel and a total scan resolution of 4096 pixels x 4096 pixels across a 1088 µm x 1088 µm FOV.

Crosslinking settings were chosen to match the total light energy used in cell-free studies and the Fluoview1200 microscope.

Afterwards, the crosslinking solution was washed out three times with fresh media. The fibrin hydrogels were incubated at 37 °C and 5% CO_2 for at least 15 min between the washes to allow for crosslinker diffusion. Next, hydrogels were hydrated with fresh media and returned to the stage top incubator for imaging. Cells between the crosslinked rectangles, and control cells at least 2 mm away from any crosslinked region were then imaged every hour for up to 100 h using the Fluoview3000 with a 4x-air 0.16NA objective lens (Olympus). Cell viability after crosslinking a single 1000 μm by 50 μm rectangle was confirmed with live-dead staining, as described previously [23]. Briefly, 2μM calcein AM (Invitrogen) excited with the 488 nm laser line was used to identify live cells and 4 μM ethidium homodimer (Invitrogen) excited with the 561 nm laser line was used to identify dead cells.

Analysis of cell migration was conducted by first hand-tracing cells in each FOV using Fiji [35]. Afterwards, cell directional bias, cell speed, orientation and direction of cell migration were quantified using a custom MATLAB script. Forward migration index (FMI) was calculated in MATLAB as the average of the ratio of cell displacement in either horizontal (FMI_X) or vertical (FMI_Y) direction to total distance traveled by each cell [11].

4.3.7. Statistical analysis

Non-parametric statistical analyses at a significance level of 0.05 were conducted to compare non-normally distributed stiffness values ($p < 0.01$, Kolmogorov-Smirnov test). The Friedman test was used to compare stiffness measurements between each oscillation axes. The Kruskal–Wallis test was performed for comparison of multiple groups. The post-hoc

Tukey–Kramer test was used to compare specific groups. Distance-dependance of stiffness was described using Spearman's rank correlation coefficient, while change in fiber alignment with distance was compared using ANOVA. The Pearson correlation coefficient was used to quantify the correlation between stiffness and frequency or amplitude of bead oscillation and to assess the time-dependency of cell migration speed. FMI values were compared using Student's *t* test. All statistical tests were performed in MATLAB.

4.4. Results

4.4.1. Circular RCP causes radial stiffening

The effect of RCP on stiffening local fibrin networks has been previously described by our group and it was proposed that RCP promotes radial stiffening outside of the crosslinked region [23]. Following enhanced capabilities of our AMR system, we can now test this hypothesis and measure stiffness in an arbitrary number of directions. Here, stiffness (κ) of the fibrin network was measured 24 h after sample preparation by oscillating embedded microbeads at 0°, 30°, 60°, 90°, 120° and 150° with respect to the horizontal axis of the camera (FOV).

In the first set of experiments, a crosslinking solution of ruthenium compound and sodium persulfate was added to 2.3 mg/ml fibrin hydrogels (**Figure 4.1A**) and allowed to diffuse for 30 min. κ within a single FOV was measured along each oscillation axes. These measurements verified that κ of the local fibrin network was isotropic (Friedman test, p = 0.22, **Figure 4.1B-C**). Afterwards, a crosslinking reaction was initiated by exposing a 50 μm diameter circular region to the 488 nm laser light for the duration of 500 scans (**Figure 4.1D**). As described previously [23–25], 488 nm light is absorbed by the ruthenium compound and initiates the crosslinking reaction by oxidizing tyrosine residues to form a dityrosine

crosslink in the presence of sodium persulfate. The effect of crosslinking on stiffness gradients is represented by **Figures 4.1E-F** (n_{beads} = 163, n_{sample} = 4). In **Figure 4.1E**, κ at each bead is measured in all 6 directions and represented by a segmented circle with segments that align with the axes of oscillation, and are color-coded for stiffness. For each bead, the axis of largest stiffness is plotted in **Figure 4.1F**. Results indicate that after crosslinking, κ within the circular region increased by a factor of 2.11, when comparing median values across all 6 directions. Stiffness within the circular crosslinked region was also found to be isotropic, based on probing 15 beads (p = 0.15). Outside of the crosslinked region, κ also increased, although predominantly in the radial direction. **Figures 4.1G-H** represent measured κ as a function of distance away from the center of the crosslinked region and the angle by which the axis of AMR oscillation deviates from the radial direction. Stiffness measured along the radial direction is plotted at 0°, while stiffness measured along the tangential direction is plotted at 90°. Before crosslinking, κ was found to be independent of distance from the circle center or deviation angle (p = 0.52, **Figure 4.1G**, **Suppl. Table 4.1**). After crosslinking, stiffness probed up to 30° from the radial direction and as far as 75 μm from the crosslinked region was found to be significantly higher than control stiffness (**Figure 4.1H**). In fact, within this ±30° bin, stiffness of the crosslinked region did not differ significantly from that of regions located up to 25 μm (p = 0.55), 25-50 μm (p = 0.33) or even 50-75 μm (p = 0.22) away from the crosslinked region. In contrast, stiffness probed 60-90° away from the radial direction did not differ from control stiffness (**Suppl. Table 4.1**), regardless of distance away from the crosslinked region center. While radial stiffening did depend to some extent on the duration of crosslinking, a maximum radial stiffening effect was observed with 500 scans, and even after 2000 scans stiffness probed 60-90° away from

the radial direction did not differ from the control stiffness (**Suppl. Figure 4.1B-C**). During crosslinking, pixel brightness increased for up to 2000 scans (**Suppl. Figure 4.1D**), predominantly inside the crosslinked region (**Figure 4.1I**).

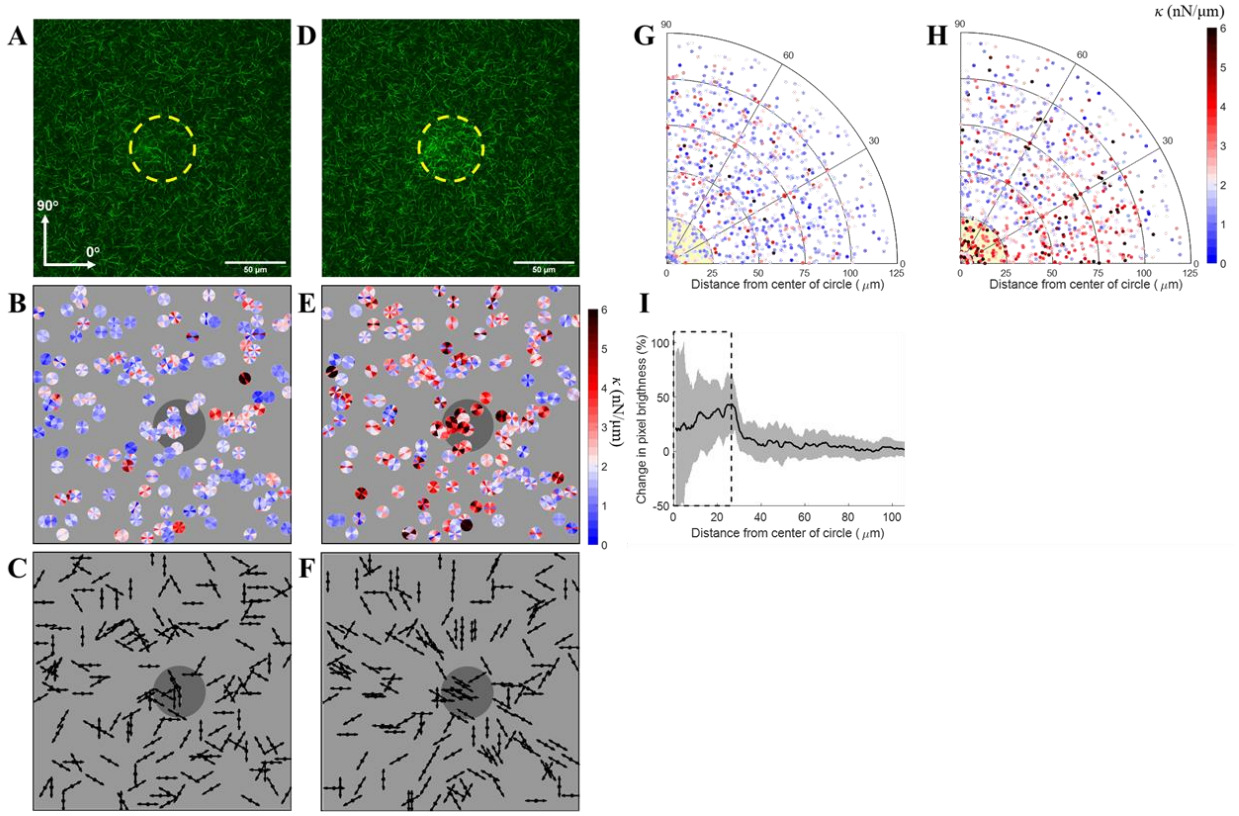

Figure 4.1. The effect of crosslinking a circular region. (A, D) Reflection confocal images before (A) and after (D) crosslinking a circular region marked by the yellow dashed line. Stiffness was probed in 6 directions using multi-axes AMR before (B) and after (E) crosslinking. Stiffness is color-coded separately for each direction of bead oscillation. Crosslinked region is marked by a dark gray background. (C, F) Direction of the highest stiffness is represented by arrows before (C) and after (F) crosslinking. (G, H) Change in stiffness with the distance away from the crosslinked circle center (yellow background) and angle of deviation of probed bead position from the radial direction before (G) and after (H) crosslinking. (I) Change in pixel brightness with distance from the crosslinked circle center. Crosslinked region is denoted by dashed rectangle. Median ± IQR.

4.4.2. Rectangular RCP creates distinct stiffness anisotropies inside and outside of the crosslinked region

Thin rectangular crosslinked regions were also studied due to their intuitive one-dimensional Cartesian symmetry, which was particularly useful when examining the volume

between two neighboring crosslinked regions. At first, a single 50 μm by 200 μm rectangular region was crosslinked using the same scanning duration and laser power settings as used for circular regions (**Figure 4.2A**). After crosslinking, κ was probed inside and outside of the crosslinked region (**Figure 4.2B**, n_{beads} = 165, n_{sample}= 4). Control stiffness measurements were conducted before crosslinking, but not necessarily in the same FOV. **Figure 4.1A** is representative of all control conditions before crosslinking. Inside the crosslinked region, κ was found to be higher than control stiffness in all directions, except along the short axis of the rectangle (0°, p = 0.71). Stiffness anisotropy in the crosslinked region was observed and κ probed along the long axis of the rectangle (90°) was significantly higher than κ probed along 0° (p < 0.01, n_{beads} = 52, **Suppl. Table 4.2**). Outside of the crosslinked region, κ measured at 0° was significantly higher than both control stiffness (p = 0.02) and stiffness probed at 90° (p < 0.01), but not different from κ probed at 0° inside the crosslinked region (p >> 0.99). Direction of the highest stiffness is visualized by arrows in **Figure 4.2C**, indicating diverse anisotropies both inside and outside of the crosslinked region. While stiffness probed at 0° did not show distance-dependency, stiffness probed at 90° decreased with the distance away from the crosslinked region (**Suppl. Figure 4.2A**; p < 0.05).

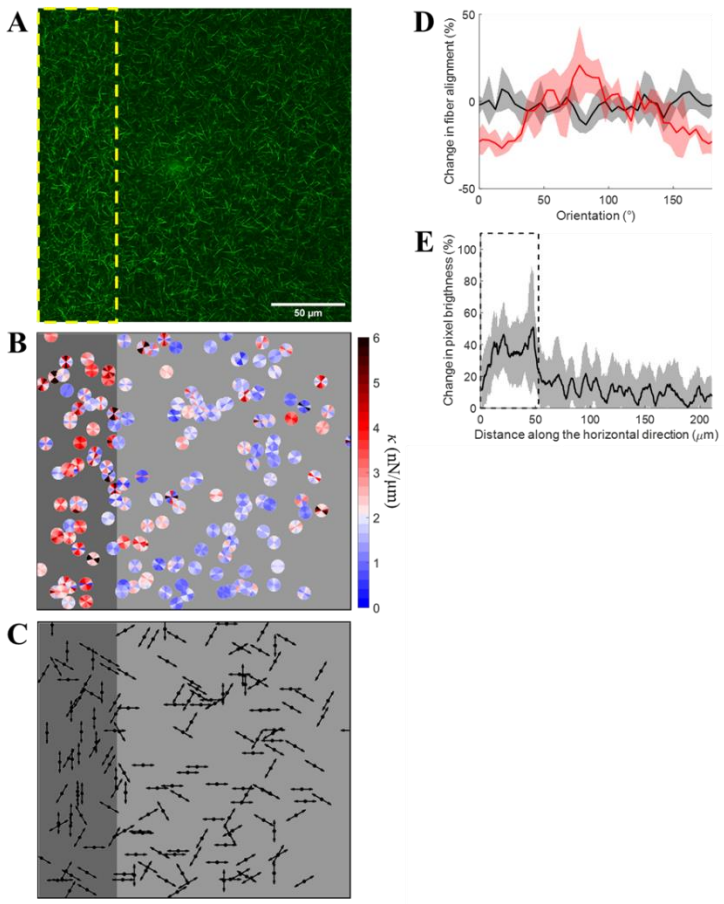

Figure 4.2. The effect of crosslinking a rectangular region. (A) Reflection confocal image after crosslinking a region marked by the yellow dashed line. (B) Stiffness was probed in 6 directions using multi-axes AMR Stiffness is color-coded separately for each direction of bead oscillation. Crosslinked region is marked by a dark gray background. (C) Direction of the highest stiffness is represented by arrows. (D) Fiber alignment within (red) and beyond (black) the crosslinked region. (E) Change in pixel brightness with distance from the crosslinked region (denoted by dashed rectangle). Median ± IQR.

These findings are corroborated by image analysis of fiber architecture before and after crosslinking. Orientation distribution of fibers was measured by processing reflection confocal images in GTFiber software for automated analysis of fibrillar morphologies [31]. After crosslinking, the crosslinked region showed a bias towards 90° fiber orientation (**Figure 4.2D**). Change in fiber alignment was not detected outside of the crosslinked region when considering that region as a whole, or binning it into regions located 0-50, 50-100, and 100-150 μm away from the crosslinked region (repeated measures ANOVA; p = 0.70, **Suppl.**

Figure 4.2B). Pixel brightness increased notably inside the crosslinked region, a finding consistent with our previous work [23] (**Figure 4.2E**). An increase in pixel brightness was also observed outside of the crosslinked region, although to a lesser extent. Pixel brightness decreased significantly with distance away from the crosslinked region (Spearman's rank correlation coefficient, r_s = -0.62, p <0.01).

4.4.3. Pairs of rectangular crosslinked regions establish more pronounced stiffness anisotropies

In order to establish more pronounced stiffness anisotropies, two 50 μm by 200 μm rectangles were crosslinked parallel to one another (**Figure 4.3A**). Rectangles were separated by either 50 μm (defined as R50) or 100 μm (defined as R100). After each treatment, κ was significantly higher than control stiffness in all directions, both inside and outside of the crosslinked regions (p < 0.01, **Suppl. Table 4.2**). Stiffness in crosslinked regions was comparable between R50 and R100 treatments (**Figure 4.3B-C**), as is also true for the non-crosslinked regions. For both R50 and R100, stiffness anisotropy was biased towards 90° inside the crosslinked regions, but towards 0° between the crosslinked regions. Interestingly, stiffness measured along the 0° direction did not change with the horizontal coordinate of probed beads. This holds true within and between the crosslinked regions. This result is in agreement with that observed up to 110 μm away from a single crosslinked rectangle (**Figure 4.2B**). However, κ within each crosslinked region was higher in the case of two crosslinked rectangles as compared to a single rectangle (with the exception of κ probed at 90°; **Suppl. Table 4.2**). Similarly, when comparing regions equidistant from a crosslinked rectangle and probed at 0°, R50 and R100 treatments resulted in higher stiffness

between the crosslinked rectangles than stiffness measured in regions adjacent to a single crosslinked rectangle (**Suppl. Table 4.3**).

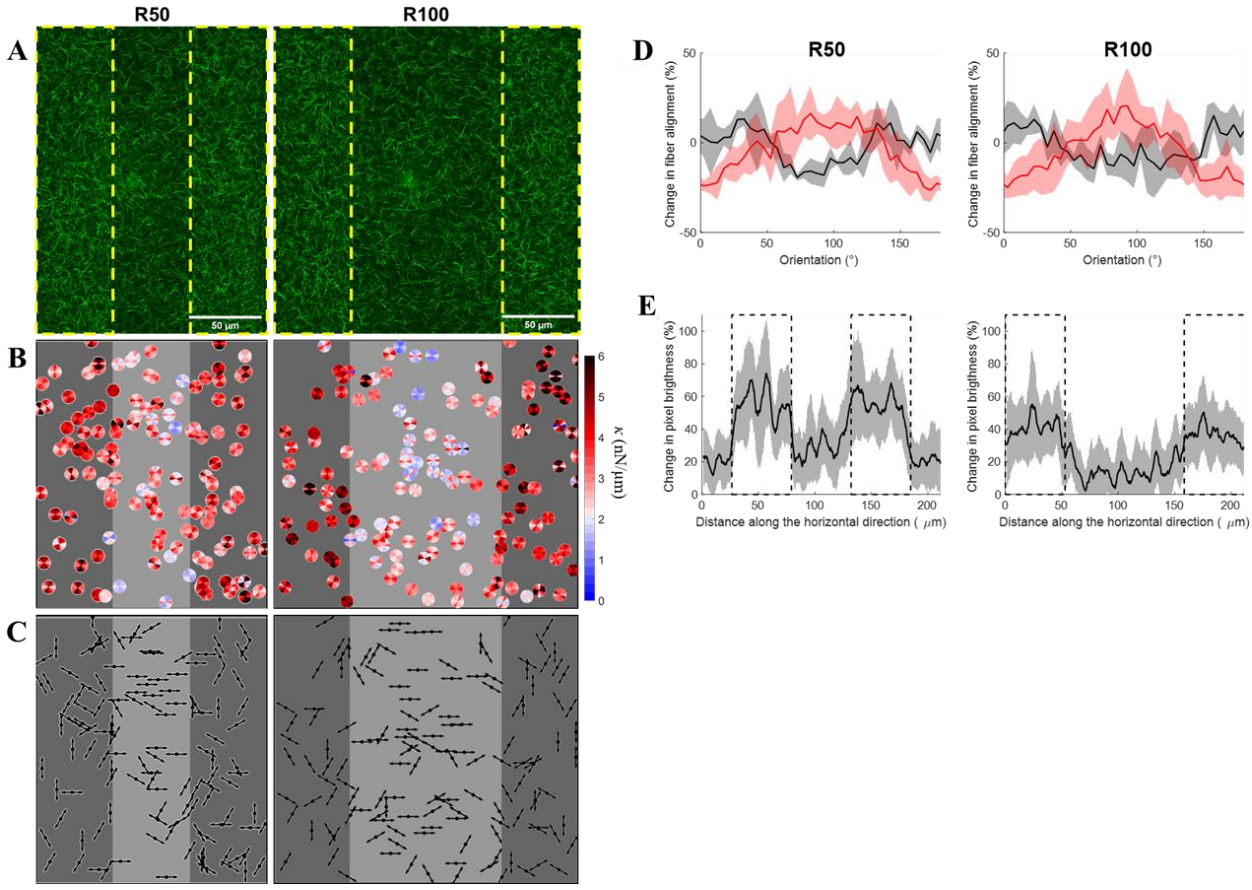

Figure 4.3. The effect of crosslinking two rectangular regions. (A) Reflection confocal images after crosslinking rectangles separated by 50 μm (R50) or 100 μm (R100) - marked by the yellow dashed lines. (B) Stiffness was probed in 6 directions using multi-axes AMR. Stiffness is color-coded separately for each direction of bead oscillation. Crosslinked region is marked by a dark gray background. (C) Direction of the highest stiffness is represented by arrows. (D) Fiber alignment within (red) and beyond (black) the crosslinked region. (E) Change in pixel brightness with distance from the crosslinked region (denoted by dashed rectangle). Median ± IQR.

An additional experiment was conducted to assess the extent by which AMR measurements of κ were frequency or bead-displacement amplitude dependent. AMR was conducted at different frequencies and amplitudes of bead oscillations following single rectangle, R50, or R100 crosslinking treatment. Stiffness was not significantly correlated with oscillation amplitudes ranging between 40 and 80 nm (**Suppl. Figure 4.3**), and was

mostly independent of oscillation frequencies between 20 and 200 Hz (**Suppl. Figure 4.4**). The Pearson correlation coefficient *r* did not exceed *r* = -0.19 and *r* = 0.15 for amplitude and frequency testing, respectively.

Fiber alignment after crosslinking either one or two rectangles was subtle and not evident without computational image analysis. Analysis in GTFiber software indicated that crosslinking two rectangles instead of one resulted in similar alignment inside the crosslinked region, but more prominent horizontal alignment outside of crosslinked regions (**Figure 4.3D**). In all cases fiber alignment was biased towards the 90° orientation inside the crosslinked region and towards the 0° orientation outside of the crosslinked region. After both R50 and R100 treatments, pixel brightness was higher inside the crosslinked regions, than between them (**Figure 4.3E**).

4.4.4. RCP induces changes in cell migration

Next, the effect of patterned photocrosslinking on direction of cell migration was evaluated in fibrin hydrogels containing MDA-MB-231 cells. MDA-MB-231 human breast cancer cells are known to respond to stiffness gradients in 2D and 3D cultures and were previously shown to display positive durotaxis [11,36,37]. Here, two 1000 µm x 50 µm rectangles spaced by 100µm were crosslinked for 2000 scans using the 488 nm laser line of a Fluoview3000 microscope. Rectangles were oriented vertically with respect to the field of view (**Figure 4.4A**). Unlike the Fluoview1200 system used for AMR measurements, the Fluoview3000 is equipped with a stage top incubator for multi-day studies. Cells were observed every hour for up to 100 h following crosslinking (n_{cells} = 15, **Figure 4.4A**). Control cells were imaged similarly (n_{cells} = 25, **Figure 4.4A**).

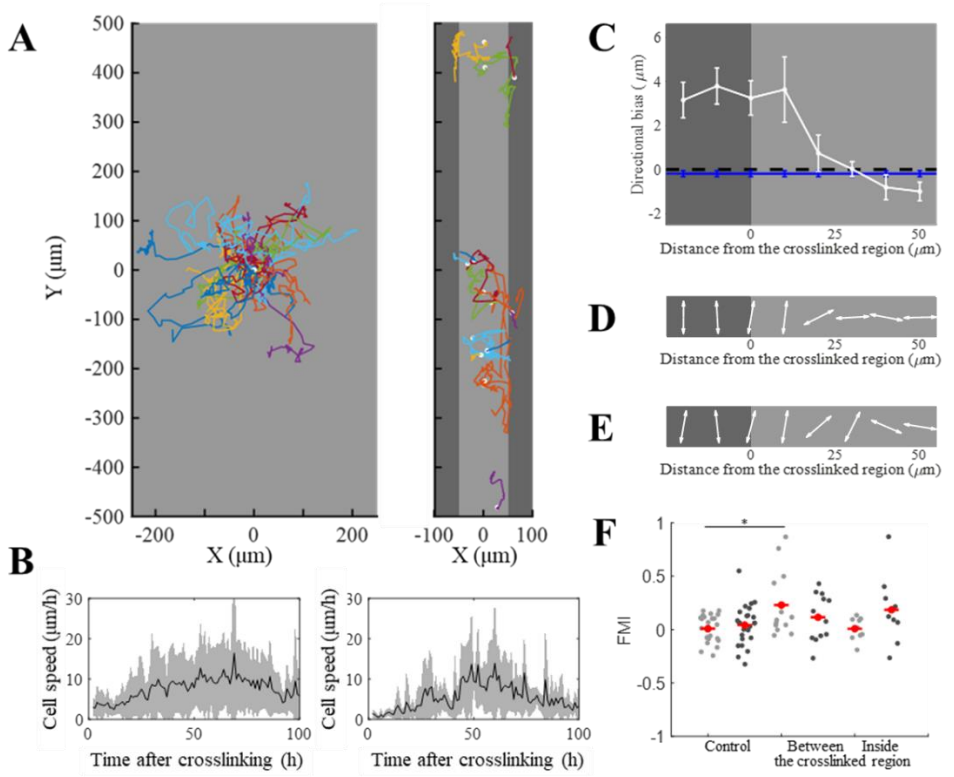

Figure 4.4. RCP induces changes in migratory behavior of MDA-MB-231 cells. (A) Trajectories of control cells (left) and cells between (right) the crosslinked rectangular regions (dark gray). (B) Change in average cell speed with time after crosslinking, calculated between every 1 h for control cells (left) and cells between the crosslinked regions (right). (C) Directional bias defined as a difference in absolute displacement in the vertical and horizontal direction for control cells (blue line) and cells between the crosslinked regions (white line). (D) Dominant cell orientation and (E) dominant direction of cell migration, represented with respect to the distance away from the crosslinked region and binned for every 10 μm (F) FMI index values for each cell in the direction perpendicular (light grey background) and parallel (dark grey background) to the crosslinked region. Mean FMI values are denoted by red markers; * denotes statistical significance.

Cells between the crosslinked regions were found to migrate at lower speeds than control cells ($p < 0.01$, **Figure 4.4B**). Cells located centrally between the crosslinked regions were more likely to move in the horizontal direction (directional bias < 0, **Figure 4.4C**) than in the vertical direction. However, as cells moved closer to the crosslinked region, they exhibited a vertical directional bias (directional bias > 0). Similarly, cells located in the central region exhibit horizontal-dominant direction of cell orientation (Figure 4D) and cell migration (**Figure 4.4E**). These trends transition to vertical near to the crosslinked

rectangles. Forward migration indices (FMI) did not differ from 0 for control cells in either horizontal (FMI_X; p = 0.72, **Figure 4.4G**) or vertical (FMI_Y; p = 0.26) direction. In contrast, cells between the crosslinked regions had higher FMI_X than control cells (FMI_X = 0.23, p < 0.01), while FMI_Y in the vertical direction (FMI_Y = 0.12) did not differ from control FMI_Y (p = 0.29).

4.5. Discussion

In this study we verified ruthenium-catalyzed photocrosslinking (RCP) as a suitable tool for creating distinct stiffness landscapes and anisotropies, both inside and outside of crosslinked regions. The use of multi-axes AMR allowed us to assess relationships between fiber alignment and stiffness anisotropy, where such properties are not accessible using surface probe technologies, single axis AMR, or bulk measurements. Crosslinking a circular region resulted in radial stiffening towards the center of the crosslinked region. Stiffness inside the crosslinked region was found to be isotropic and 2.1-fold higher than before crosslinking. Fold-increase in stiffness after RCP was comparable with the effect of magnetic alignment of fibers [10] and with other methods of creating stiffness gradients in natural hydrogels [38].

In order to further investigate RCP effect on local ECM changes, different crosslinked geometries were explored. Rectangular crosslinking promoted stiffening and fiber alignment inside the crosslinked region biased along the long axis of the rectangle. Outside of the crosslinked region, the reverse bias was observed up to 110 μm away from the crosslinked rectangle, suggesting that the region is under tension and RCP may induce strain hardening. Interestingly, stiffness measured in the horizontal direction (0°) did not change with probed bead location indicating lack of measurable spatial gradients (**Suppl. Figure 4.2A**, **Suppl.**

Figure 4.5). The lack of distance-dependent stiffness gradients probed at 0° is consistent with strain hardening. In contrast, stiffness gradients with respect to the horizontal axis of the image were detected when stiffness was measured along 60°, 90° and 120° direction (**Suppl. Figure 4.2A**, **Suppl. Figure 4.5**).

Crosslinking two rectangles instead of one resulted in higher stiffness and a greater change in fiber alignment. Surprisingly, we found pixels in between the crosslinked regions to be brighter for R50 as compared to R100. Such differences in pixel brightness could be indicative of diffusion of the crosslinking radicals from the laser-scanned region. However, crosslinking results in a detectable autofluorescence (Ex: 561 nm, Em: 570-670 nm) and only fibers in the selected laser-scanned region had detectable signal, suggesting that chemical alterations were highly localized (**Suppl. Figure 4.6**).

MDA-MB-231 cells exhibited behavior consistent with contact guidance along a network of fibers aligned by micropatterned RCP. The cells favored horizontal migration between the crosslinked rectangles where fibers were biased towards the horizontal direction (**Figure 4.4C**). As cells approached the crosslinked regions with fibers exhibiting more vertical orientation, they orientated themselves accordingly. Similarly, cell orientation was shown to correspond with the axis of the highest stiffness. Our experiments show that not only were fibers aligned, but stiffness was anisotropic, and these 'off-axis' stiffness values did exhibit gradients in the horizontal direction (**Suppl. Figure 4.5**). In consideration of biophysical cues, it is possible that effects of contact guidance were supplemented by these gradients, a phenomena currently being investigated by our group.

Changes in fiber alignments introduced by RCP are quite subtle, and significantly less prominent than changes caused by magnetic alignment of fibers [9,20,21] or mechanical

stretching of hydrogels [22]. Nonetheless, observed changes in migratory behaviour and alignment of MDA-MB-231 cells indicate that the effect of RCP on fiber alignment and stiffness landscape is strong enough to promote directed cell migration. Moreover, unlike other existing methods, RCP can alter stiffness landscape and anisotropy around individual cells embedded inside 3D fibrous hydrogels and allows for observation of a single cell's response to changes in local ECM physical properties. Relevant to such studies, the extent of stiffness anisotropy and fiber alignment can be readily controlled by crosslinking duration, delivered light dose, photoinitiator concentration or by modifying the geometry of the crosslinked region. Further, compared to commonly used crosslinking techniques developed for synthetic hydrogels [39,40] or riboflavin-based crosslinking of naturally-derived fibrous hydrogels [41], RCP does not require the use of ultraviolet (UV) light. RCP can be induced using a 488 nm laser line, which is safer for cells and readily available in most confocal laser scanning microscopes.

4.6. Conclusion

In this study, multi-axes AMR and analysis of reflection confocal microscopy images were used to assess the effect of micropatterned ruthenium-catalyzed photocrosslinking on local ECM stiffness anisotropy and fiber alignment. We verified that RCP can be applied to establish distinct local stiffness anisotropies in adjacent regions. Cells were shown to respond to RCP-mediated changes and exhibited directed cell migration congruent with fiber alignment direction, axis of greatest stiffness, and in a direction for which off-axis stiffness values do exhibit spatial gradients. The usefulness of RCP in cell-ECM studies is further underscored by its wide availability to most investigators and applicability to fibrous 3D hydrogels and other strain-hardening materials.

4.7. Acknowledgments

Research reported in this publication was supported by the United States National Science Foundation (US-NSF) under Award Number DMS-1953410. The content is solely the responsibility of the authors and does not necessarily represent the official views of the US-NSF. Approximately, $50,000 of United States federal funds supported the effort (100%) on this project. Use of confocal microscope Fluoview3000 within the Edwards Lifesciences Foundation Cardiovascular Innovation and Research Center was supported by (NIH 1S10OD025064-01A1). No effort on this project was supported by non-federal funds.

4.8. Supplementary materials

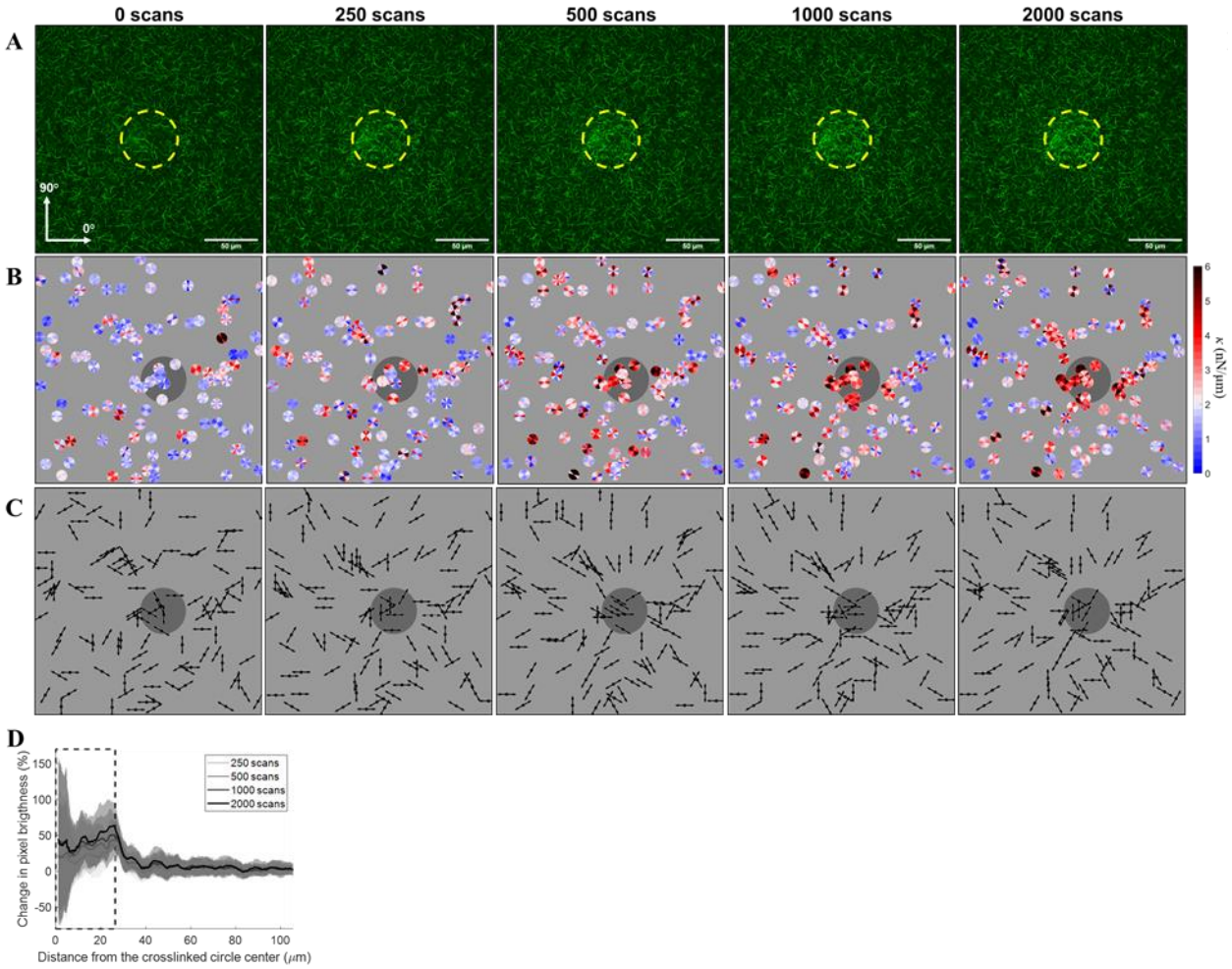

Suppl. Figure 4.1. Supplementary data to Figure 4.1. (A) Reflection confocal images of the same FOV before and after 250, 500, 1000 and 2000 crosslinking scans. Crosslinked region is marked by yellow dashed line (B) Stiffness measurements inside (dark gray background) and outside (light gray background) of the crosslinked region. Segmented circles represent a single probed bead where segment orientation corresponds to axis of bead oscillation. Each segment is color-coded for stiffness. (C) Direction of the highest stiffness for each segmented circle in (B) is indicated by the direction of the arrow. (D) Change in pixel brightness with distance from the center of the crosslinked circle. Change is relative to pixel brightness before crosslinking.

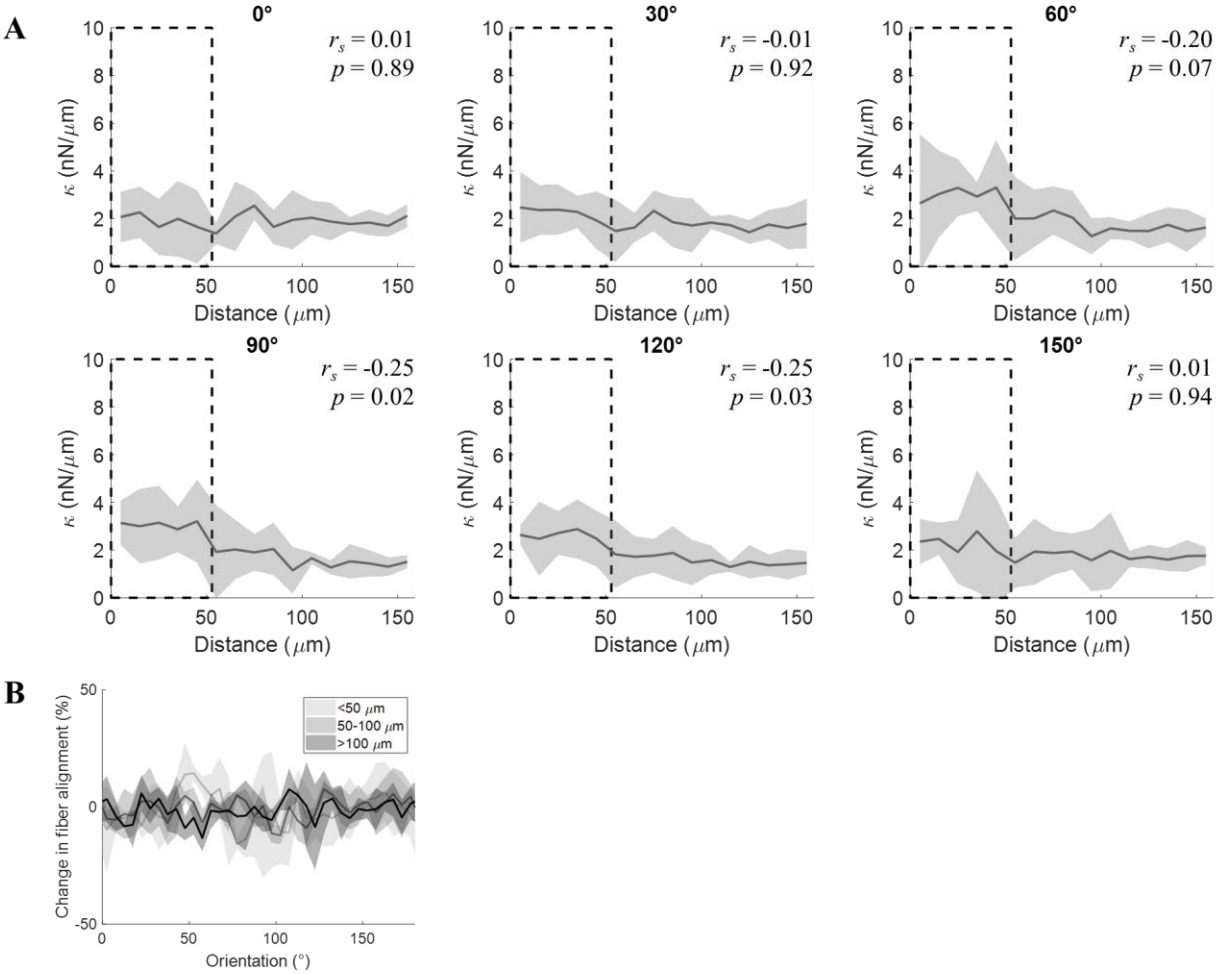

Suppl. Figure 4.2. Supplementary data to Figure 4.2. (A) Change in stiffness with distance from the left edge of the crosslinked region (dashed line). Median ± IQR. Spearman's rank correlation coefficient r_s calculated outside of the crosslinked region and corresponding p values are listed for each direction of bead oscillation (0°, 30°, 60°, 90°, 120°, 150°). (B) Change in fiber alignment with normal distance from the crosslinked region (single rectangular crosslinked region). Mean ± std.

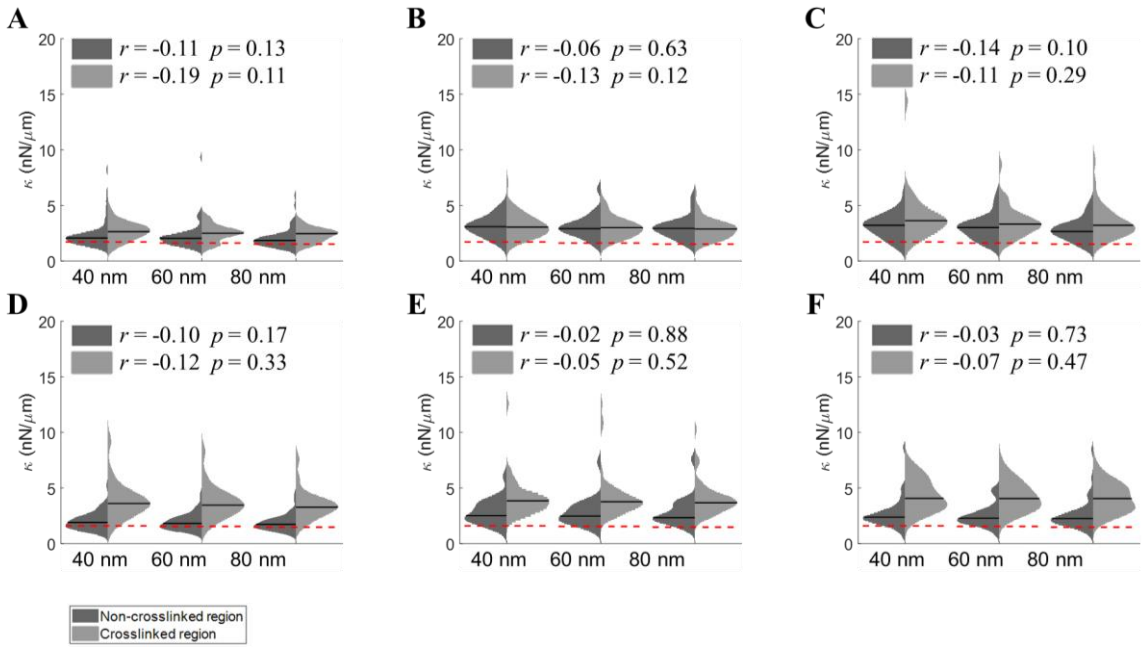

Suppl. Figure 4.3. Supplementary data to Figures 4.2 and 4.3. Distribution of stiffness measured at different amplitudes of bead oscillation inside (light gray) and outside (dark gray) of the single rectangle (A, D), R50 (B, E) or R100 (C, F) treatment. Beads were oscillated at either 0° (A-C) or 90° (D-F). Median stiffness is represented by black lines. Pearson correlation coefficient *r* and corresponding *p*-statistics are listed for each condition. Median control stiffness is represented by red dashed line.

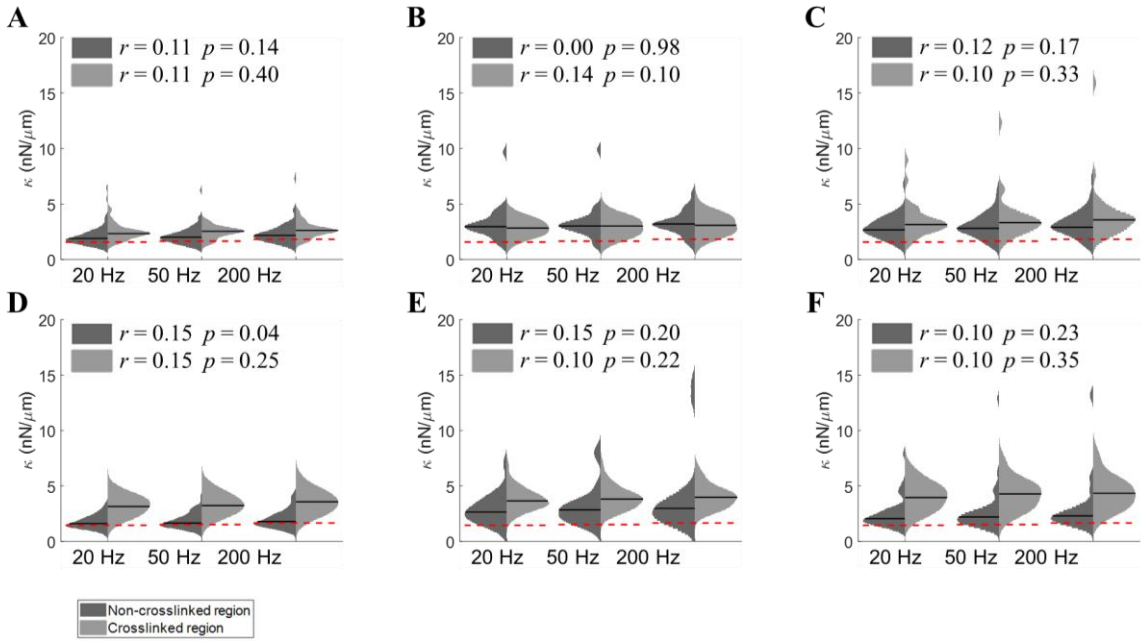

Suppl. Figure 4.4. Supplementary data to Figures 4.2 and 4.3. Distribution of stiffness measured at different frequencies of bead oscillation inside (light gray) and outside (dark gray) of the single rectangle (A, D), R50 (B, E) or R100 (C, F) treatment. Beads were oscillated at either 0° (A-C) or 90° (D-F). Median stiffness is represented by black lines. Pearson correlation coefficient *r* and corresponding *p*-statistics are listed for each condition. Median control stiffness is represented by red dashed line.

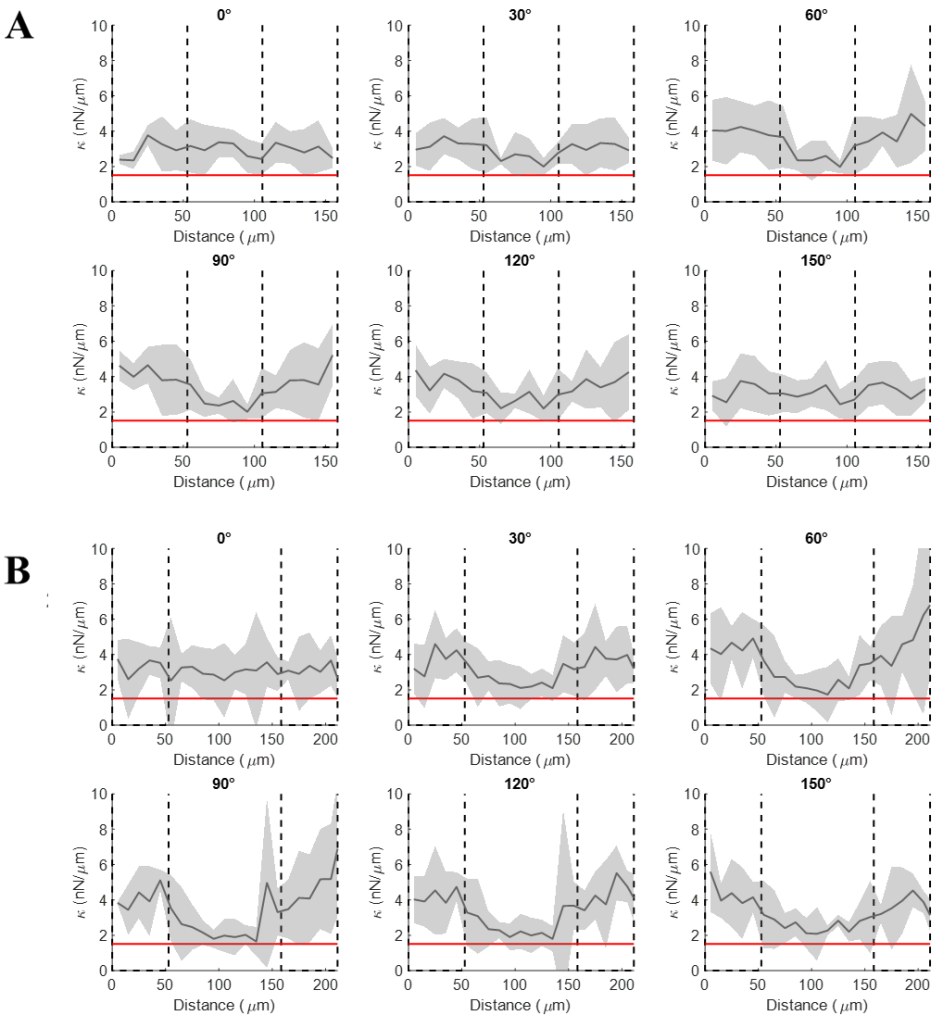

Suppl. Figure 4.5. Supplementary data to Figure 3. Change in stiffness with probed bead location after R50 (A) and R100 (B) treatment in cell-free hydrogels. Median ± IQR. Median stiffness of hydrogels before crosslinking is denoted by the red line.

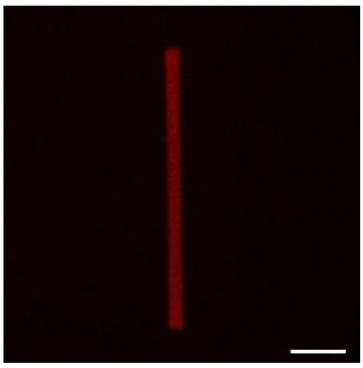

Suppl. Figure 4.6. Autofluorescence of the crosslinked region imaged by the FV3000 confocal microscope using microscope setting for the ethidium homodimer but increasing pixel brightness. Scale bar = 200 μm.

Suppl. Table 4.1. Supplementary table to Figure 4.1G-H: *p*-statistics using Tukey-Kramer test after Kruskal-Wallis test.

Distance, Deviation angle	Before	<25µm, [0:30°]	<50µm, [0:30°]	<75µm, [0:30°]	<100µm, [0:30°]	<150µm, [0:30°]	<25µm, [30:60°]	<50µm, [30:60°]	<75µm, [30:60°]	<100µm, [30:60°]	<150µm, [30:60°]	<25µm, [60:90°]	<50µm, [60:90°]	<75µm, [60:90°]	<100µm, [60:90°]	<150µm, [60:90°]
Before		<0.01	<0.01	<0.01	<0.01	>>0.99	<0.01	<0.01	<0.01	<0.01	>>0.99	<0.01	>>0.99	0.96	0.91	>>0.99
<25µm, [0:30°]			0.55	0.33	0.22	<0.01	>>0.99	<0.01	<0.01	<0.01	<0.01	>>0.99	<0.01	<0.01	<0.01	<0.01
<50µm, [0:30°]				>>0.99	>>0.99	<0.01	0.85	0.23	0.09	0.02	<0.01	0.31	<0.01	<0.01	<0.01	<0.01
<75µm, [0:30°]					>>0.99	<0.01	0.66	0.43	0.21	0.07	<0.01	0.15	<0.01	<0.01	<0.01	<0.01
<100µm, [0:30°]						<0.01	0.52	0.49	0.24	0.07	<0.01	0.09	<0.01	<0.01	<0.01	<0.01
<150µm, [0:30°]							<0.01	0.78	0.89	0.95	>>0.99	<0.01	>>0.99	>>0.99	>>0.99	>>0.99
<25µm, [30:60°]								<0.01	<0.01	<0.01	<0.01	>>0.99	<0.01	<0.01	<0.01	<0.01
<50µm, [30:60°]									>>0.99	>>0.99	0.48	<0.01	0.05	0.68	0.63	0.71
<75µm, [30:60°]										>>0.99	0.64	<0.01	0.11	0.84	0.81	0.84
<100µm, [30:60°]											0.76	<0.01	0.17	0.94	0.92	0.92
<150µm, [30:60°]												<0.01	>>0.99	>>0.99	>>0.99	>>0.99
<25µm, [60:90°]												0	<0.01	<0.01	<0.01	<0.01
<50µm, [60:90°]														>>0.99	>>0.99	>>0.99
<75µm, [60:90°]															>>0.99	>>0.99
<100µm, [60:90°]																>>0.99

Suppl. Table 4.2. Supplementary table to Figure 4.2B and 4.3B: *p*-statistics using Tukey-Kramer test after Kruskal-Wallis (white background) or Friedman (green background) test.

			Single rectangle								Rectangles 50 µm apart								Rectangles 100 µm apart							
			Crosslinked region			Non-crosslinked region					Crosslinked region				Non-crosslinked region				Crosslinked region				Non-crosslinked region			
			0°	30°	60°	90°	120°	150°	0°	30°	60°	90°	120°	150°	0°	30°	60°	90°	120°	150°	0°	30°	60°	90°	120°	150°
Control			0.71	<0.01	<0.01	<0.01	<0.01	<0.01	0.02	0.91	0.86	>0.99	>0.99	0.86	<0.01	<0.01	<0.01	<0.01	<0.01	<0.01	<0.01	<0.01	<0.01	<0.01	<0.01	<0.01
Single rectangle	Crosslinked region	0°		0.58	<0.01	<0.01	<0.01	<0.01	>0.99	>0.99	>0.99	>0.99	0.9	>0.99	<0.01	<0.01	<0.01	<0.01	<0.01	<0.01	<0.01	<0.01	<0.01	<0.01	<0.01	<0.01
		30°			<0.01	<0.01	0.06	0.86	>0.99	0.46	0.52	0.04	<0.01	0.52	0.03	<0.01	<0.01	<0.01	<0.01	0.15	>0.99	>0.99	>0.99	>0.99	0.33	>0.99	>0.99	>0.99
		60°				0.90	0.55	0.01	<0.01	<0.01	<0.01	<0.01	<0.01	<0.01	>0.99	>0.99	>0.99	>0.99	>0.99	>0.99	>0.99	>0.99	>0.99	>0.99	>0.99	>0.99	>0.99
		90°					0.07	<0.01	<0.01	<0.01	<0.01	<0.01	<0.01	<0.01	>0.99	>0.99	>0.99	>0.99	>0.99	>0.99	>0.99	>0.99	>0.99	>0.99	>0.99	>0.99	>0.99
		120°						0.58	0.01	0.41	0.47	0.03	<0.01	0.47	0.04	<0.01	<0.01	<0.01	<0.01	0.65	>0.99	>0.99	>0.99	>0.99	>0.99	>0.99	>0.99	>0.99
		150°							0.99	0.31	0.55	<0.01	<0.01	0.57	<0.01	<0.01	<0.01	<0.01	<0.01	<0.01	<0.01	<0.01	<0.01	<0.01	<0.01	<0.01	<0.01
	Non-crosslinked region	0°									>0.99	0.10	<0.01	>0.99	<0.01	<0.01	<0.01	<0.01	<0.01	<0.01	<0.01	<0.01	<0.01	<0.01	<0.01	<0.01	<0.01
		30°										0.03	<0.01	>0.99	<0.01	<0.01	<0.01	<0.01	<0.01	<0.01	<0.01	<0.01	<0.01	<0.01	<0.01	<0.01	<0.01
		60°											0.43	0.03	<0.01	<0.01	<0.01	<0.01	<0.01	<0.01	<0.01	<0.01	<0.01	<0.01	<0.01	<0.01	<0.01
		90°												<0.01	<0.01	<0.01	<0.01	<0.01	<0.01	<0.01	<0.01	<0.01	<0.01	<0.01	<0.01	<0.01	<0.01
		120°													<0.01	<0.01	<0.01	<0.01	<0.01	<0.01	<0.01	<0.01	<0.01	<0.01	<0.01	<0.01	<0.01
		150°																									
Rectangles 50 µm apart	Crosslinked region	0°														0.76	<0.01	<0.01	>0.99	0.97	>0.99	>0.99	>0.99	0.52	>0.99	>0.99	>0.99
		30°															<0.01	<0.01	>0.99	0.55	<0.01	<0.01	<0.01	<0.01	<0.01	<0.01	<0.01
		60°																<0.01	>0.99	0.02	<0.01	<0.01	<0.01	<0.01	<0.01	<0.01	<0.01
		90°																	>0.99	0.52	<0.01	<0.01	<0.01	<0.01	<0.01	<0.01	<0.01
		120°																		0.14	>0.99	>0.99	>0.99	>0.99	>0.99	>0.99	>0.99
		150°																			0.02	0.97	>0.99	0.69	0.92	>0.99	>0.99
	Non-crosslinked region	0°																				0.02	>0.99	>0.99	>0.99	>0.99	>0.99
		30°																					>0.99	>0.99	>0.99	>0.99	>0.99
		60°																						0.67	>0.99	>0.99	>0.99
		90°																							0.84	0.01	>0.99
		120°																								0.29	>0.99
		150°																									>0.99
Rectangles 100 µm apart	Crosslinked region	0°																									
		30°																									
		60°																									
		90°																									
		120°																									
		150°																									
	Non-crosslinked region	0°																									
		30°																									
		60°																									
		90°																									
		120°																									
		150°																									

Suppl. Table 4.3. Supplementary table to Figure 4.2B and 4.3B comparing stiffness probed up to 25 µm (A) or 50 µm (B) from the crosslinked region: *p*-statistics using Tukey-Kramer test after Kruskal-Wallis test.

A		**R50**						**R100**					
		0°	**30°**	**60°**	**90°**	**120°**	**150°**	**0°**	**30°**	**60°**	**90°**	**120°**	**150°**
Single rectangle	**0°**	<0.01	0.55	0.69	0.82	0.51	0.03	0.02	0.08	0.03	0.22	0.31	0.27
	30°	<0.01	0.25	0.37	0.51	0.22	<0.01	<0.01	0.02	<0.01	0.07	0.11	0.1
	60°	0.01	0.73	0.85	0.93	0.69	0.06	0.05	0.16	0.06	0.36	0.48	0.43
	90°	<0.01	0.23	0.35	0.49	0.21	<0.01	<0.01	0.02	<0.01	0.07	0.11	0.09
	120°	<0.01	0.02	0.04	0.08	0.02	<0.01	<0.01	<0.01	<0.01	<0.01	<0.01	<0.01
	150°	<0.01	0.03	0.06	0.11	0.03	<0.01	<0.01	<0.01	<0.01	<0.01	0.01	<0.01
R50	**0°**							>>0.99	>>0.99	>>0.99	>>0.99	>>0.99	>>0.99
	30°							0.98	>>0.99	0.99	>>0.99	>>0.99	>>0.99
	60°							0.93	>>0.99	0.95	>>0.99	>>0.99	>>0.99
	90°							0.83	0.98	0.87	>>0.99	>>0.99	>>0.99
	120°							0.98	>>0.99	0.99	>>0.99	>>0.99	>>0.99
	150°							>>0.99	>>0.99	>>0.99	>>0.99	>>0.99	>>0.99

B		**R100**					
		0°	**30°**	**60°**	**90°**	**120°**	**150°**
Single rectangle	**0°**	<0.01	0.01	0.06	0.61	0.29	<0.01
	30°	<0.01	<0.01	<0.01	0.12	0.03	<0.01
	60°	<0.01	<0.01	0.03	0.47	0.2	<0.01
	90°	<0.01	<0.01	<0.01	0.2	0.06	<0.01
	120°	<0.01	<0.01	<0.01	0.02	<0.01	<0.01
	150°	<0.01	<0.01	<0.01	0.07	0.02	<0.01

4.9. References

1. Malandrino, A., Trepat, X., Kamm, R. D. & Mak, M. Dynamic filopodial forces induce accumulation, damage, and plastic remodeling of 3D extracellular matrices. *PLoS Comput. Biol.* **15**, 1–26 (2019).

2. Doyle, A. D. & Yamada, K. M. Mechanosensing via cell-matrix adhesions in 3D microenvironments. *Exp. Cell Res.* **343**, 1–7 (2015).

3. Kular, J. K., Basu, S. & Sharma, R. I. The extracellular matrix : Structure, composition, age-related differences, tools for analysis and applications for tissue engineering. *J. Tissue Eng.* **5**, 1-17 (2014).

4. Linke, P. *et al.* Dynamic Contact Guidance of Myoblasts by Feature Size and Reversible Switching of Substrate Topography: Orchestration of Cell Shape, Orientation, and Nematic Ordering of Actin Cytoskeletons. *Langmuir* **35**, 7538–7551 (2019).

5. Ramirez-San Juan, G. R., Oakes, P. W. & Gardel, M. L. Contact guidance requires spatial control of leading-edge protrusion. *Mol. Biol. Cell* **28**, 1043–1053 (2017).

6. Ray, A. *et al.* Anisotropic forces from spatially constrained focal adhesions mediate contact guidance directed cell migration. *Nat. Commun.* **8**, 1-17 (2017).

7. Nuhn, J. A. M., Perez, A. M. & Schneider, I. C. Contact guidance diversity in rotationally aligned collagen matrices. *Acta Biomater.* **66**, 248–257 (2018).

8. Leclech, C. & Villard, C. Cellular and Subcellular Contact Guidance on Microfabricated Substrates. *Front. Bioeng. Biotechnol.* **8**, 1–30 (2020).

9. Kim, J. *et al.* The mechanics and dynamics of cancer cells sensing noisy 3D contact guidance. *Proc. Natl. Acad. Sci. U. S. A.* **118**, 1–8 (2021).

10. Thrivikraman, G. *et al.* Cell contact guidance via sensing anisotropy of network mechanical resistance. *Proc. Natl. Acad. Sci. U. S. A.* **118**, 1–11 (2021).

11. DuChez, B. J., Doyle, A. D., Dimitriadis, E. K. & Yamada, K. M. Durotaxis by Human Cancer Cells. *Biophys. J.* **116**, 670–683 (2019).

12. Lo, C. M., Wang, H. B., Dembo, M. & Wang, Y. L. Cell movement is guided by the rigidity of the substrate. *Biophys. J.* **79**, 144–152 (2000).

13. Sunyer, R. *et al.* Collective cell durotaxis emerges from long-range intercellular force transmission. *Science (80-.).* **353**, 1157–1161 (2016).

14. Jensen, C. & Teng, Y. Is It Time to Start Transitioning From 2D to 3D Cell Culture? *Front. Mol. Biosci.* **7**, 1–15 (2020).

15. Whang, M. & Kim, J. Synthetic hydrogels with stiffness gradients for durotaxis study and tissue engineering scaffolds. *Tissue Eng. Regen. Med.* **13**, 126–139 (2016).

16. D'Arcangelo, E. & McGuigan, A. P. Micropatterning strategies to engineer controlled cell and tissue architecture in vitro. *Biotechniques* **58**, 13–23 (2015).

17. Ray, A., Slama, Z. M., Morford, R. K., Madden, S. A. & Provenzano, P. P. Enhanced Directional Migration of Cancer Stem Cells in 3D Aligned Collagen Matrices. *Biophys. J.* **112**, 1023–1036 (2017).

18. Morin, K. T. & Tranquillo, R. T. Guided sprouting from endothelial spheroids in fibrin gels aligned by magnetic fields and cell-induced gel compaction. *Biomaterials* **32**, 6111–6118 (2011).

19. Jin, Y. *et al.* Thermally tunable dynamic and static elastic properties of hydrogel due to volumetric phase transition. *Polymers (Basel).* **12**, 1-13 (2020).

20. Namani, R., Wood, M. D., Sakiyama-Elbert, S. E. & Bayly, P. V. Anisotropic mechanical properties of magnetically aligned fibrin gels measured by magnetic resonance elastography. *J. Biomech.* **42**, 2047–2053 (2009).

21. Taufalele, P. V., VanderBurgh, J. A., Muñoz, A., Zanotelli, M. R. & Reinhart-King, C. A. Fiber alignment drives changes in architectural and mechanical features in collagen matrices. *PLoS One* **14**, 1–11 (2019).

22. Nam, E., Lee, W. C. & Takeuchi, S. Formation of Highly Aligned Collagen Nanofibers by Continuous Cyclic Stretch of a Collagen Hydrogel Sheet. *Macromol. Biosci.* **16**, 995–1000 (2016).

23. Keating, M., Lim, M., Hu, Q. & Botvinick, E. Selective stiffening of fibrin hydrogels with micron resolution via photocrosslinking. *Acta Biomater.* **87**, 88–96 (2019).

24. Bjork, J., Johnson, S. & Tranquillo, R. Ruthenium-catalyzed photo cross-linking of fibrin-based engineered tissue. *Biomaterials* **32**, 2479–2488 (2011).

25. Fancy, D. A. & Kodadek, T. Chemistry for the analysis of protein-protein interactions: Rapid and efficient cross-linking triggered by long wavelength light. *Proc. Natl. Acad. Sci. U. S. A.* **96**, 6020–6024 (1999).

26. Mizuno, D., Head, D. A., MacKintosh, F. C. & Schmidt, C. F. Active and passive microrheology in equilibrium and nonequilibrium systems. *Macromolecules* **41**, 7194–7202 (2008).

27. Jagiełło, A., Lim, M. & Botvinick, E. Dermal fibroblasts and triple-negative mammary epithelial cancer cells differentially stiffen their local matrix. *APL Bioeng.* **4**, 1-12 (2020).

28. Keating, M., Kurup, A., Alvarez-Elizondo, M., Levine, A. J. & Botvinick, E. Spatial distributions of pericellular stiffness in natural extracellular matrices are dependent on cell-mediated proteolysis and contractility. *Acta Biomater.* **57**, 304–312 (2017).

29. Juliar, B. A., Keating, M. T., Kong, Y. P., Botvinick, E. L. & Putnam, A. J. Sprouting angiogenesis induces signi fi cant mechanical heterogeneities and ECM stiffening across length scales in fi brin hydrogels. *Biomaterials* **162**, 99–108 (2018).

30. Jones, C. A. R. *et al.* Micromechanics of cellularized biopolymer networks. *Proc. Natl. Acad. Sci. U. S. A.* **112**, E5117–E5122 (2015).

31. Persson, N. E., McBride, M. A., Grover, M. A. & Reichmanis, E. Automated analysis of orientational order in images of fibrillar materials. *Chem. Mater.* **29**, 3–14 (2017).

32. Allersma, M. W., Gittes, F., DeCastro, M. J., Stewart, R. J. & Schmidt, C. F. Two-Dimensional Tracking of ncd Motility by Back Focal Plane Interferometry. *Biophys. J.* **74**, 1074–1085 (1998).

33. Staunton, J. R. *et al.* Mechanical Properties of the Tumor Stromal Microenvironment Probed In Vitro and Ex Vivo by In Situ-Calibrated Optical Trap-Based Active Microrheology. *Cell. Mol. Bioeng.* **9**, 398–417 (2016).

34. Blehm, B. H., Devine, A., Staunton, J. R. & Tanner, K. In vivo tissue has non-linear rheological behavior distinct from 3D biomimetic hydrogels, as determined by AMOTIV microscopy. *Biomaterials* **83**, 66–78 (2016).

35. Schindelin, J. *et al.* Fiji: An open-source platform for biological-image analysis. *Nat. Methods* **9**,

676–682 (2012).

36. Ansardamavandi, A., Tafazzoli-shadpour, M., Ali, M. & Group, F. Behavioral remodeling of normal and cancerous epithelial cell lines with differing invasion potential induced by substrate elastic modulus. *Cell Adh. Migr.* **12**, 472–488 (2018).

37. Riching, K. M. *et al.* 3D collagen alignment limits protrusions to enhance breast cancer cell persistence. *Biophysj* **107**, 2546–2558 (2014).

38. Chang, C. Y. & Lin, C. C. Hydrogel models with stiffness gradients for interrogating pancreatic cancer cell fate. *Bioengineering* **8**, 1–18 (2021).

39. Choi, J. R., Yong, K. W., Choi, J. Y. & Cowie, A. C. Recent advances in photo-crosslinkable hydrogels for biomedical applications. *Biotechniques* **66**, 40–53 (2019).

40. Eke, G., Mangir, N., Hasirci, N., MacNeil, S. & Hasirci, V. Development of a UV crosslinked biodegadable hydrogel containing adipose derived stem cells to promote vascularization for skin wounds and tissue engineering. *Biomaterials* **129**, 188–198 (2017).

41. Tirella, A., Liberto, T. & Ahluwalia, A. Riboflavin and collagen: New crosslinking methods to tailor the stiffness of hydrogels. *Mater. Lett.* **74**, 58–61 (2012).

Chapter 5: Conclusions

Cell-ECM interactions are highly complex, dynamic and not yet fully understood. In context of my work, stiffness of local ECM was previously described to regulate numerous cellular behaviors, alter wound healing processes and cancer progression. Cells in the human body sense local stiffness and can also exhibit contact guidance and durotaxis, migrating along the direction of fiber alignment or along the stiffness gradients, respectively. Nonetheless, studies on cell-ECM interactions in 3D cultures have often been hindered by the lack of available tools to measure and dynamically alter peri-cellular ECM stiffness.

My thesis is a continuation of our laboratory's research on probing peri-cellular stiffness using optical tweezers active microrheology. With my work, I introduced multi-axes stiffness measurements and quantified not only stiffness magnitudes around the cells but also described the extent of stiffness anisotropy established by the cells or induced with patterned photocrosslinking method. In **Chapter 2**, I demonstrated the effect of different treatments on local stiffness magnitudes and anisotropy around dermal fibroblasts and human breast cancer cells. Stiffness anisotropy patterns were shown to vary strongly with concentration of collagen hydrogels, cell type and tested treatment. In **Chapter 3**, I described cell type specific response to a wider range of collagen concentrations. Unlike in Chapter 2, and irrespective of the collagen concentration, cells did not strongly alter stiffness of local ECM, suggesting that cell remodeling of ECM stiffness varies with the duration of cell culture. Further, the role of ECM type was also assessed in Chapter 3, elucidating distinct cell behaviors and peri-cellular stiffness landscapes varying with ECM type and treatment. Taken together, findings described in Chapter 2 and Chapter 3 underscore the need for peri-cellular and not bulk stiffness measurements in studies on cellular mechanotransduction.

In **Chapter 4**, I validated the method of ruthenium-catalyzed patterned crosslinking as a useful tool in studying directed cell migration. Patterned crosslinking introduced distinct stiffness anisotropies and fiber alignment patterns in regions close to the cells. In response to changes in fiber architecture and stiffness landscape, human breast cancer cells exhibited contact guidance and durotaxis. These two widely known phenomena have not been extensively studied on a single cell level inside naturally-derived fibrous hydrogels. I am hopeful that this method can be applied by other researchers to further our knowledge of processes governing directed cell migration and improve our understanding of cell-ECM interactions.